TEXAS Geosciences
The University of Texas at Austin
Jackson School of Geosciences
Institute for Geophysics

Alejandro Cardona
alejandro.cardona@utexas.edu; +1 737 600 9348

Lyles School of Civil Engineering
College of Engineering
Purdue University

Oct 29, 2023

Dear Members of the Faculty Search Committee:

I am writing to apply for the tenure-track faculty position in Civil Engineering at the assistant professor rank. I am currently a Research Associate at The University of Texas at Austin (UT), following my postdoctoral position at UT and doctoral studies at King Abdullah University of Science and Technology (KAUST). My research addresses challenges related to reducing the negative environmental impacts of energy geo-systems, emphasizing *geo-centered and geotechnical solutions*.

Findings from my research have implications for our understanding of subsurface fluid transport, with a wide range of applications relevant to green and low-carbon energy geosystems (e.g., geothermal energy, CO_2 sequestration, energy geo-storage) and strengthening the climate resilience of our infrastructure (e.g., offshore geotechnics, permafrost thawing, gassy soils stability during warming). My approach is based on the design, development, and construction of physics-focused experiments, complemented with numerical simulations and analyses of large data sets. In my current role, I have explored the evolution of hydrate-bearing sediments through geomechanical analysis. I use pressure coring technology to investigate hydrate samples at in-situ conditions. My dissertation investigated permeability in geomaterials, hydromechanical processes in fractured rocks, and capillary effects in dual-porosity systems.

My teaching emphasizes key concepts explored in terms of their basic physics in lectures, and complemented by hands-on experience in labs to further explore and apply the material. For example, as teaching assistant for the "Experimental Methods in Research" class at KAUST during the pandemic, with all students in quarantine, I prepared weekly projects that explored fundamental physical processes with kitchen utensils, cellphone technology, and advanced signal processing. I am looking forward to teaching opportunities at Purdue where curiosity-driven exercises feature in the classroom.

I envision developing a vigorous and externally funded research program with a mix of federal, state and industry funding. My group will combine laboratory experiments, numerical/analytical models, and data-driven analysis to understand processes relevant to the low-energy civil systems and resilient infrastructure. The expertise of the department in geotechnical engineering will support these developments. I will strive to educate future science and industry leaders. I would be able to teach Geotechnical Eng., Rock Mechanics and Foundation Analysis and Design, for example. I aim to implement new courses related to Energy and the Environment, Geomechanics for Geo-Energy Applications, and Experimental Methods in Research.

I thank you in advance for your time and consideration. I look forward to hearing from you soon.

Sincerely,
Alejandro Cardona

Alejandro Cardona

Institute for Geophysics
Jackson School of Geosciences
The University of Texas at Austin
2305 Speedway
Austin, TX, 78712

alejandro.cardona@utexas.edu
+1 737 600 9348
https://ig.utexas.edu/staff/alejandro-cardona

I. EDUCATION

Ph.D.	2020	Energy Resources and Petroleum Engineering	KAUST, Saudi Arabia
M.S.	2016	Earth Sciences and Engineering	KAUST, Saudi Arabia
B.S.	2015	Petroleum Engineering	UNAL, Colombia

II. EMPLOYMENT

2022-present	Research Associate	UT Austin, USA
2020-2022	Postdoctoral Fellow	UT Austin, USA
2015-2020	Graduate Research Assistant	KAUST, Saudi Arabia
2014	Wellbore Stability Intern	Equion Energia, Colombia
2013-2014	Undergraduate Research Assistant	UNAL, Colombia

III. PUBLICATIONS

ARTICLES IN REFEREED JOURNALS

Published

Cardona A., Liu Q., and Santamarina J.C. (2023), The capillary pressure vs. saturation curve in a fractured rock mass: fracture and matrix contributions, *Scientific Reports*, v. 13, 12044, doi: 10.1038/s41598-023-38737-y

Cardona A. and Santamarina J.C. (2023), Immiscible fluid displacement in fractured media: A dual porosity microfluidics study, *International Journal of Rock Mechanics and Mining Sciences*, v. 170, 105555, doi:10.1016/j.ijrmms.2023.105555

Cardona A., Bhandari A., and Heidari M. and Flemings P.B. (2023). The viscoplastic behavior of natural hydrate bearing sediments under uniaxial strain compression (K_0 loading), *Journal of Geophysical Research: Solid* Earth, v. 128, e2023JB026976, doi:10.1029/2023JB026976

Cardona A. and Santamarina J.C. (2023), A Convenient Device to Measure the Permeability of Intact Rock (Heterogeneity and Anisotropy), *Geotechnical Testing Journal*, v. 46 (5), doi:10.1520/GTJ20220112

Cardona A., Finkbeiner T. and Santamarina J.C. (2021), Natural Rock Fractures: From Aperture to Fluid Flow, *Rock Mechanics and Rock Engineering*, v. 54, p 5827-5844, doi:10.1007/s00603-021-02565-1

Cardona A. and Santamarina J.C. (2020), Carbonate rocks: Matrix permeability estimation, *AAPG Bulletin*, v.104 (1), p 131-144 doi:10.1306/05021917345

Under review (PDF available on request)

Bhandari A., **Cardona A.**, Flemings P.B, Germaine J. T. Geomechanical behavior of sandy silts from Green Canyon 955 hydrate reservoir - Deepwater Gulf of Mexico, *Marine and Petroleum Geology*

Rodriguez-Florez X., Barbosa A., Guimarães L., **Cardona A.** and Finkbeiner T. Impact of carbonate content, rock texture, and roughness on fracture transmissivity and acid-etching patterns in carbonate rocks, *Rock Mechanics and Rock Engineering*

In preparation (PDF available on request)

Cardona A., You K. and Flemings P.B, Relative permeability of hydrate-bearing sediments: the critical role of hydrate dissolution *(to be submitted to Geophysical Research Letters)*

Cardona A., Finkbeiner T. and Santamarina J.C, Numerical Study of Fractured Reservoirs: Hydromechanical Analysis of the Permeability Tensor *(to be submitted to Rock Mechanics and Rock Engineering)*

Terzariol M. and **Cardona A.**, Methane Hydrate-Bearing Sediments Morphology: Spatial Variability, Physical Properties and Implications *(to be submitted to Geophysical Research Letters)*

CHAPTERS IN BOOKS

Santamarina J.C., Park J., Terzariol M., **Cardona A.**, Castro G., Cha W., Garcia A., Hakiki F., Lyu C., Salva-Ramírez M., Shen Y., Sun Z., Chong S.H. (2019), Soil Properties: Physics Inspired, Data Driven, *in: Lu N., Mitchell J. (eds) Geotechnical Fundamentals for Addressing New World Challenges*, Springer Series in Geomechanics and Geoengineering, Springer, doi:10.1007/978-3-030-06249-1_3

PEER-REVIEWED CONFERENCE ARTICLES

Cardona A., Finkbeiner T. and Santamarina J.C. (2020), Numerical Study of Fractured Reservoirs: Hydromechanical Analysis of the Permeability Tensor. *4th Naturally Fractured Reservoir Workshop*, Ras Al Khaimah, UAE.

Araujo, E., Alzate, G., Arbelaez, A., **Cardona, A.**, Pena, S., Naranjo, A. (2014), Analytical Prediction Model of Sand Production Integrating Geomechanics for Open Hole and Cased Hole – Perforated Wells. *Conference Paper SPE 171107-MS. SPE Heavy and Extra Heavy Oil Conference: Latin America*, Medellin, Colombia, 24-26 September. doi:10.2118/171107-ms

TECHNICAL REPORTS

Price, A., Flemings, P., Thomas, C., **Cardona, A.**, Murphy, Z., Garcia, A., Savage, A., Houghton, J., and Pettigrew T. (2021), GOM2 Pressure Coring Tool with Ball Valve (PCTB) Land Test III Report.

Cardona A., Finkbeiner T., Santamarina J.C. (2019), Hydromechanical Response of Fractured Carbonates, Saudi Aramco - Final Deliverable.

THESES

Cardona A. (2020), Fluid Transport in Fractured Carbonate Rocks, PhD Dissertation, KAUST. doi: 10.25781/KAUST-8A4ZQ

Cardona A. (2014), Software Construction to Generate Mechanical Earth Models from Well Logs, Engineering Thesis, UNAL (Universidad Nacional de Colombia), Colombia (in Spanish).

IV. INVITED SEMINAR TALKS

01/ 2023	Energy Geotechnology: Understanding Geo-Material Behavior *South Dakota School of Mines & Technology*
11/2022	Methane Hydrates at the University of Texas: Expeditions & Geo-material Behavior *UTIG 50th Anniversary, The University of Texas at Austin (link)*
09/2022	Energy Geotechnology: Flow & Geomechanics *National Energy Technology Laboratory (NETL)*
06/2022	Hydrate-bearing sediments: K_0 Loading and Creep *KAUST*
09/2021	Flow Phenomena in Geomaterials: Unraveling Processes and Behavior *UTIG, The University of Texas at Austin (link)*

V. HONORS AND AWARDS

03/2022	GRC Travel Award, *Natural Gas Hydrate Systems GRC 2022*
12/2016	Commencement speaker candidate, *KAUST*
2015-2020	KAUST Graduate Fellowship, *KAUST*
01/2015	WEP Annual Poster Competition, *KAUST*
09/2013	1st Place in Petro Cup SPE, *XV Colombian Congress of Oil and Gas*

VI. FIELD EXPERIENCE

08/2023	UT-GOM2-2: Gulf of Mexico Deepwater Hydrates Expedition - Dockside *Physical Properties Specialist* (2 weeks), Salt Lake City, UT, USA
08/2023	UT-GOM2-2: Gulf of Mexico Deepwater Hydrate Expedition - Offshore *Downhole & Pressure Core Specialist* (1 month), Gulf of Mexico, USA
04/2021	Pressure Coring Tool with Ball Valve Land Test III *Pressure Core Specialist* (1 week), Catoosa, OK
02/2020	Naturally Fractured Reservoirs Field Trip, EAGE Workshop *On-site geoscientist* (2 days), Northern Emirates Mountains
11/2017	Carbonate Analogues Field Trip, KAUST *On-site geoscientist* t (2 days), Abu Dhabi
07/2014	Well Floreña AP-13 drilling operation, Equion Energia *Wellbore stability engineer* (1 week), Colombian Foothills

VII. RESEARCH METHODS

A. EXPERIMENTAL DEVICES – DESIGN, CONSTRUCTION, OPERATION

(contributed in initiating/developing experimental hardware for laboratories)

- Triaxial cell for hydrate-bearing sediments at in-situ fluid pressure
- Torsional shear and radial flow for pre-fractured specimens
- Matrix permeameter for unjacketed rock specimens
- Micromodel fabrication using soft lithography with pressure and optical instrumentation
- Bench-scale 2D flow sandbox model with optical measurements

B. SCIENTIFIC INSTRUMENTS - OPERATION

Rock and soil mechanics, petrophysics, complex fluids

- Manipulation and testing of natural hydrate-bearing sediments under pressure and temperature
- High Pressure High Temperature: Core Flooding, Triaxial System, Contact Angle and Interfacial Tension
- Mercury Intrusion Porosimetry (MICP), Helium porosimetry
- Surface Roughness by Interferometry

Material characterization, imaging, and nanofabrication

- Analytical chemistry. Gas Sorption Specific Surface (Micromeritics ASAP 2420), Mercury Porosimeter (Micromeritics AutoPore IV)
- Imaging and Characterization. X-Ray Diffractometer (Rigaki Miniflex), X-Ray Computer Tomography (Tescan XRE), Nuclear Magnetic Resonance (Oxford Instruments, 12 MHz), Scanning Electron Microscopy SEM (Quanta 600 at KAUST Corelab), White Light Interferometer (Nanovea ST400 and Nanovea JR25)
- Nanofabrication. Mask Maker (Heidelberg µPG501), Mask Aligner (EVG 6200), Plasma Cleaner (Plasma Etch PE-50)

C. ANALYTICAL AND NUMERICAL TOOLS

Software development

- Pore-scale modeling: invasion percolation, fracture flow, fracture digital analogues
- Digital image correlation: strain analysis, fluid invasion fronts (micro&bench scale)
- Element-based models: coupled thermo-hydro-chemo-mechanical processes
- Programming languages: Python, Matlab, Mathcad, Mathematica, Fortran
- Numerical tools: finite differences, finite elements

Commercial software - operation

- High Performance Computing (HPC): Texas Advanced Computer Center (TACC)
- Laboratory software: Solidworks, AutoCAD, LabView, ImageJ
- FEM/DEM/Visualization Software: COMSOL, LIGGGHTS, Paraview
- Petroleum and geological engineering software: GMI-Suite, Fracman, CMG, Eclipse, Petrel, Interactive Petrophysics, Techlog, Matlab Reservoir Simulation Tool MRST

VIII. TEACHING AND ADVISING

Teaching Assistantships

Experimental Methods for Research & Digital Signal Processing, *Summer 2020*, KAUST
Rock Mechanics for Energy Geo-Engineering, *Fall 2019*, KAUST
Well logging, *Spring and Fall 2013*, UNAL

Undergraduate Research Students

At University of Texas at Austin

Camila Van Der Maal (2023)	Resedimentation in clay-rich materials
Colton Hayden (2022)	Strain-rate effects in salt-sand mixtures

IX. CONFERENCE ABSTRACTS

Cardona A., Fang Y., You K., and Flemings P.B (2023), Relative Permeability of Hydrate-Bearing Sediments: The Critical Role of Hydrate Dissolution, *AGU 2023*, San Francisco

Terzariol M. and **Cardona A.** (2023), Pore Habit of Natural Hydrate-Bearing Sediments: Learnings from GHASS2 Cruise, *AGU 2023*, San Francisco.

Cardona A., Bhandari A.R., and Flemings P.B. (2022), Creep and stress relaxation behavior of hydrate-bearing sediments: implications for stresses during production and geological sedimentation, *AGU 2022*, Chicago, IL.

Cardona A., Rasmussen C., Shionalyn K., Gase A., Boddupalli B., Greenbaum J. S., Buhl D., Morrison S., Reyes A., Soderlund K.M, and Van Avendonk H.J. (2022), Developing a Code of Conduct at The University of Texas at Austin, Institute for Geophysics (UTIG) - Alternative Approaches, Measures of Success, and Open Questions, *AGU 2022*, Chicago, IL.

Flemings P.B., Fang Y., You K., and **Cardona A.** (2022), The Water Relative Permeability Behavior of Hydrate-bearing Sediment, *AGU 2022*, Chicago, IL.

Shionalyn K., Rasmussen C., Buhl D., **Cardona A.**, Morrison S., Reyes A., Soderlund K.M, and Van Avendonk H.J. (2022), Working from the ground up-initiating a new code of conduct for improved inclusion, *AGU 2022*, Chicago, IL.

Terzariol M. and **Cardona A.** (2022), Natural Hydrate-Bearing Sediments: Pore Habit, *GDR 2022 - Hydrates*, Paris.

Rodriguez-Florez X., Finkbeiner T., Guimarães L., Barbosa, A., and **Cardona A.** (2022), Natural fracture flow - mechanical and chemical degradation effects on carbonates, *ARMA International Geomechanics Symposium IGS*, Abu Dhabi, UAE.

Cardona A., Fang Y., and Flemings P.B. (2022), Methane hydrate-bearing sediments: in-situ state of stress, *Natural Gas Hydrate Systems: Gordon Research Conference 2022* (*cancelled)*, Oxnard, CA.

Cardona A., Fang Y., O'Connell J., and Flemings P.B. (2021), Validation of hydro-geomechanical properties in high pressure triaxial device for hydrate-bearing core analysis, *AGU 2021*, New Orleans, LA. doi: 10.1002/essoar.10508543.1

Liu, Q., **Cardona, A.** and Santamarina J.C. (2020), Capillarity vs. Saturation in Fracture-Matrix Systems, *InterPore*, online format.

Cardona A., Finkbeiner T., and Santamarina J.C. (2020), Numerical Study of Fractured Reservoirs: Hydromechanical Analysis of the Permeability Tensor, *4th EAGE Workshop on Naturally Fractured Reservoirs*, United Arab Emirates.

Cardona A., Finkbeiner T., and Santamarina J.C. (2020), The Hydro-Mechanical Response of a Single Carbonate Fracture, *International Petroleum Technology Conference*, Saudi Arabia.

Cardona A., and Santamarina J.C. (2018), Matrix Permeability in Carbonate Rocks, *KAUST Research Conference: Recovery of Difficult Hydrocarbons*, Saudi Arabia.

X. RESEARCH PROJECTS AND CONSULTING

Supercomputing Allocations

- Impact of viscoelastic inclusions on the geomechanical behavior of sediments, (2022-2023)
  Source: Texas Advanced Computer Center (TACC), 500 node-hours
  Role: Principal Investigator

XI. SERVICE

Professional contributions

Reviewer of Journal and Conference Articles

- Acta Geotechnica
- Energy & Fuels
- AGU: Geophysical Research Letters, Journal of Geophysical Research: Solid Earth
- Rock Mechanics and Rock Engineering
- ARMA Symposium, American Rock Mechanics Association

Organizer of Conferences, Workshops, or Sessions

- Co-convener, Session on Gas hydrates in Earth's subsurface, *AGU 2023.* Dec 2023.
- Organizer, Pressure core monthly discussion (UT Austin, JAIST, USGS, NETL), *Virtual*, Jan 2022 - Dec 2022
- Co-organizer, Athenaeum on Dissolution and Precipitation: Implications for Energy Geo-Engineering, *KAUST*, Feb 2016

Membership in Professional Organizations

- Society of Petroleum Engineers (SPE)
- American Geophysical Union (AGU)
- The International Society for Porous Media (Interpore)
- American Association of Petroleum Geologists (AAPG)
- European Association of Petroleum Geoscientists (EAGE)

Campus contributions

At UT Austin

- Co-organizer, GeoFORCE K-12 outreach program, July 2022
- Postdoctoral representative, UTIG Diversity, Equity, Inclusion and Accessibility (DEIA) Committee, August 2022 - Present

XII. CLOSE COLLABORATORS

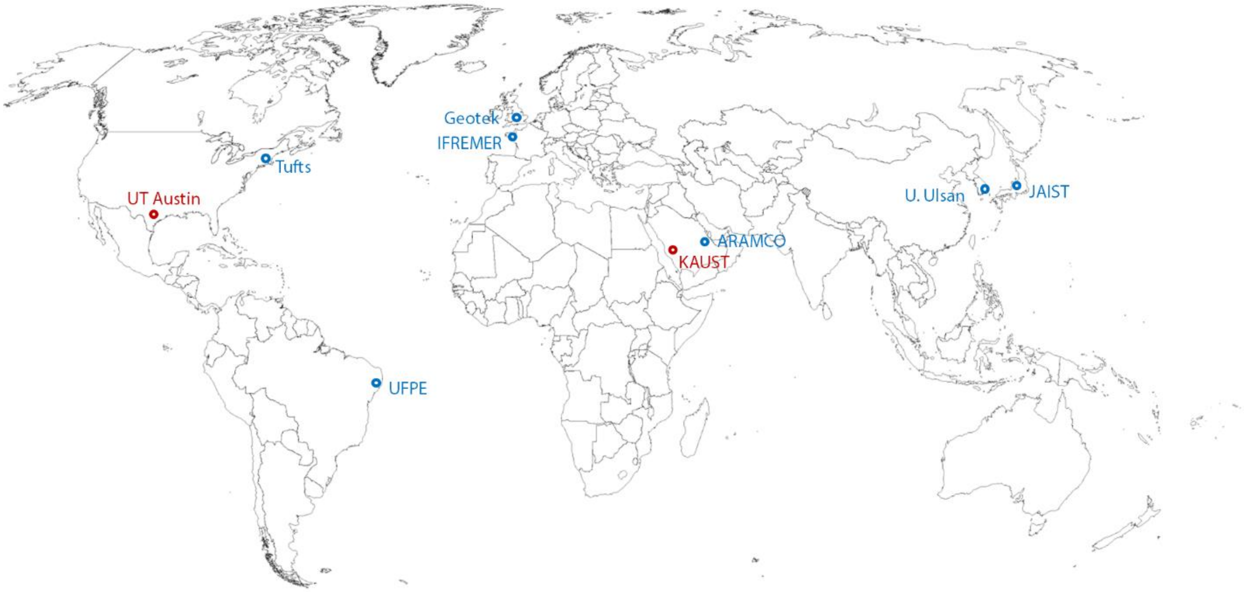

Advisors

- Peter B. Flemings, UT Austin (Postdoctoral Advisor)
- J. Carlos Santamarina, KAUST (PhD Advisor)

Current Collaborators at UT Austin

- Nicolas Espinoza - creep of geomaterials
- Athma R. Bhandari - experimental geomechanics
- Mahdi Heidari - creep of geomaterials
- Carla Thomas - pressure cores
- Joshua O'Connell - pressure cores manipulation and analysis

Active collaborations with academics outside UT Austin

- Thomas Finkbeiner, KAUST - geomechanics
- John Germaine, Tufts - experimental geomechanics
- Qi Liu, KAUST - complex fluids
- Jun Yoneda, JAIST - pressure cores
- Marco Terzariol, IFREMER - hydrate-bearing sediments
- Hosung Shin, U. Ulsan - fractured rocks
- Leonardo do Nascimento Guimarães, UFPE - fractured rocks

Industrial Collaborations

- Nikolaus Bigalke, Geotek - pressure cores
- Peter Schultheiss, Geotek - pressure cores
- Yaser Alzayer, ARAMCO - fractured rocks

Statement of Teaching

Alejandro Cardona

Teaching philosophy. Growth in resource demand, climate change, and inadequate infrastructure are among the most pressing issues facing society, and engineers will provide the solutions to some of these challenges. We as educators, must recognize that, while engineering curricula can only cover a subset of concepts, future professionals must be versatile to solve anticipated future threats and unforeseen technological difficulties. My philosophy builds upon these ideas; students must be strong in long-lasting fundamentals to solve any engineering problem, but with transferrable skillsets that allow them to rapidly apply the learned material in a continuously evolving world.

Background and experience. Being a teaching assistant in the "Experimental Methods in Research" class during Covid-19 times was one of the most enriching scholarly experiences I have had. We had to solve the issue of leading student experiments while being outside of a laboratory. Everyday household items were our reagents, cellphones gained importance as wonderful sensors, and thorough data processing strengthened analyses. I envision building a learning environment that emulates this experience at Purdue; key concepts constitute the essential core and creativity and ingenuity are taught within an engineering framework.

Teaching and learning styles. My teaching agenda will include a small number of techniques to satisfy students' needs. Global implications and facts are presented to motivate learning (e.g., the complex link between energy and economics). For example, to create resource-awareness, I would ask students to find their personal electricity use. Students will use sketch drawings to learn attention to detail. People primary learn when they are actively engaged[1]; therefore, students will develop independent in-depth research projects.

Awareness of students' understanding. Proof that learning is achieved is a hallmark of education. I plan to measure students' learning with homework, exams, and research projects. While each assignment will follow thorough feedback, I will encourage critical thinking. Feedback is more powerful when it addresses flawed interpretations rather than a lack of understanding[2]. I will urge students to collaborate among them to strengthen their teamwork abilities.

Teaching at Purdue University. My experiences as a teaching assistant together with my interdisciplinary research serve as background to teach several existing courses offered in the School of Civil and Environmental Engineering at both undergraduate and graduate levels. I would be able to teach (1) Geotechnical Eng., (2) Rock Mechanics and (3) Foundation Analysis and Design. I look forward to teaching and developing new courses related to (1) Energy and the Environment, (2) Geomechanics for Geo-Energy Applications, (3) Experimental Methods in Research.

Teaching vision. Teaching and learning are intimately related, and good teaching comes from years of trial and error. My vision as an educator is to provide tools for reasoning to create scientifically independent civil engineering professionals, and the evaluations from students will be paramount to achieve this goal. I aim to advance the understanding of engineering systems in a culturally rich, inclusive, and equitable learning environment.

---

[1] Hattie, J., and Timperley, H. (2007), The Power of Feedback. *Review of Educational Research*, vol. 77(1), DOI: 10.3102/003465430298487

[2] Hake, R. (1996), Interactive-engagement versus traditional methods: A six-thousand-student survey of mechanics test data for introductory physics courses, *American Journal of Physics*, vol. 66(64), DOI: 10.1119/1.18809

Statement of Research

Alejandro Cardona

Research vision

The history of civil engineering reflects the changes of societal needs through time, from infrastructure and dams, to earthquake and environmental engineering. Today, we are facing unprecedented challenges related to earth resources, climate change, and resilient infrastructure. Among these challenges, energy and associated environmental costs emerge as primary stressors for a sustainable future. Current estimates project a 30% power demand increase by midcentury worldwide, with a 25% share of the total energy from renewables. My research agenda aims to tackle these challenges by engineering low environmental impact civil systems, with emphasis on *geotechnical solutions.*

My research in *Energy Geotechnology* extends our knowledge of geomaterial behavior to understand geotechnical systems under extreme conditions, saturated and interacting with complex fluids, and subjected to repetitive loads and localizations of all kinds. While the central theme of these studies is energy, results from this research can be extended to strengthen the climate resilience of our infrastructure. These studies are relevant for adaptable offshore infrastructure, thawing permafrost due to global warming, and contaminant remediation and waste storage.

Current Research and Major Contributions

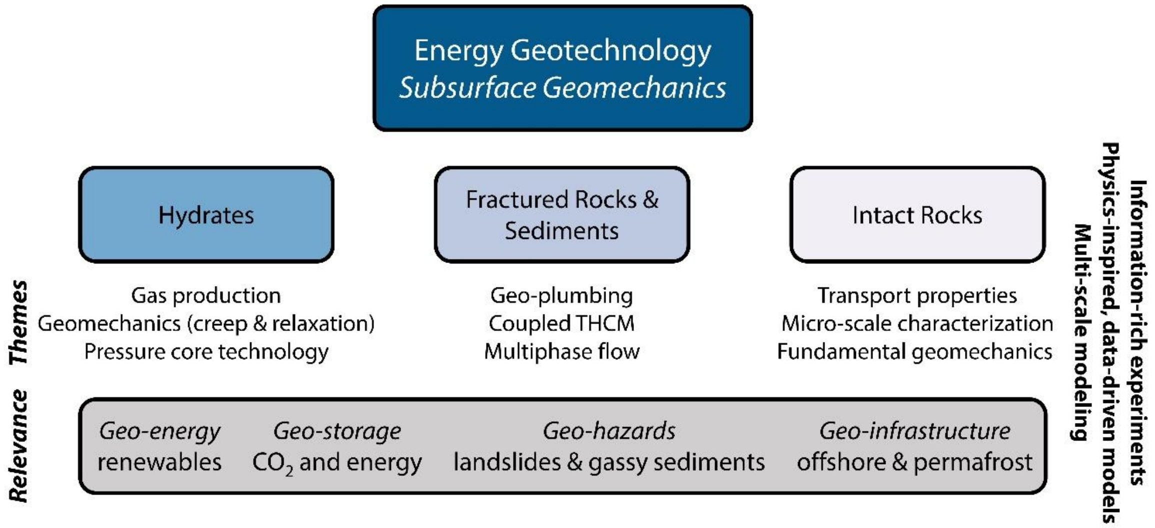

‘Frozen methane’ or gas hydrate is a potential energy resource and an active component in the Earth’s carbon cycle. The geomechanical behavior of hydrate-bearing sediments is critical for gas production, wellbore design and seafloor stability. Using pressure core technology (i.e., hydrates are preserved at high pressure and low temperature during testing), I found hydrate-bearing sediments are viscoplastic materials: deformation, stress and strength are rate-dependent.

Fractured rocks are the host or foundation for many engineered and geological structures related to energy, water, waste, and transportation. Understanding the flow through subsurface fracture rock masses is among the most significant challenges associated to these applications. I have combined fracture digital analogs, experimental studies, and numerical modeling to understand hydromechanical processes in fractures. I found that stress-sensitive fractures dominate flow, whereas fluids in the rock matrix determine the storage capacity of the fractured rock mass.

Rock permeability is defined by the porous network topology and size. However, existing permeability models often overlook pore size-related parameters. I combined extensive databases with permeability measurements and found that permeability can be predicted with the largest percolating pore size. I developed a predictive model and compared its uncertainty with more complex approaches.

Future Research

My approach will combine experimental designs, analytical/numerical studies, and data-driven analyses. Within the next *five years*, my team will develop the following scientific themes.

Repetitive loading response of geomaterials - Energy geo-storage. Renewable energy resources such as wind and solar are intermittent and energy must be stored to accommodate off-peak generation. Energy *geo-storage* such as compressed air and hydrogen provide the storage capacities very challenging to achieve with electrochemical systems. Geomaterials in these applications experience different kinds of repetitive loads (thermal, mechanical, environmental) that can gradually fatigue these systems. I will explore the long-term behavior of geomaterials subjected to multiple cycles and identify optimal strategies for energy storage.

Particle-laden flow and heat transport in fractures - Geothermal energy. The heat in the subsurface is a renewable energy resource available 24/7 regardless of weather. However, the vast majority of these geothermal reservoirs are hosted within low-permeable rocks and a transmissive fracture network must be created to extract heat. I will explore particle-laden flow as means of (i) maintaining fractures open and (ii) avoiding thermal short-circuiting (i.e., flow localization that hinders heat extraction). The proposed study will combine fracture digital analogs, experimental studies, and large-scale numerical modeling.

Hydro-chemo-mechanical phenomena in geomaterials. The flow of reactive fluids through geological media can drive the development of runaway processes. For example, mineral dissolution enlarges the pore sizes, causing flow localization and further dissolution. Civil geosystems must be resilient upon these processes. I will investigate the geomechanical evolution of sediments upon mineral dissolution, targeting caprock (i.e., aquitard) integrity during CO_2 geological storage and foundation stability in dissolvable media.

Geomaterial behavior of gassy soils. Gas exsolution and expansion alter the geomechanical behavior of geomaterials, threatening the stability of civil systems upon changes in pressure and temperature. I will investigate the geomechanical and petrophysical evolution of sediments under these conditions. High-pressure microfluidic studies will be implemented to observe pore-scale interactions while geotechnical testing using samples from recent offshore expeditions will explore these effects at the macroscale. This research will impact CO_2 storage in the subsurface, foundation stability of offshore sediments (i.e., suction caisson), peats and landfills failure.

Contribution to Purdue University

I will establish the “Geo-Energy Processes Laboratory GEPL” in the Lyles School of Civil Engineering. My lab will collaborate with faculty within the geotechnical eng. group; Professors Bobet, Santagata and Prezzi, as well as faculty in the Department of Earth Sciences. I am committed to securing research funding to support my projects. I will pursue opportunities from various funding sources, including the Department of Energy (NETL, FECM, EERE) and National Science Foundation (EAR, OCE, IODP, CMMI, CBET). I will also consider grants provided by the U.S. Geological Survey, American Chemical Society, state-level agencies.

TEXAS Geosciences
The University of Texas at Austin
Jackson School of Geosciences
Institute for Geophysics

Alejandro Cardona
alejandro.cardona@utexas.edu; +1 737 600 9348

Lyles School of Civil Engineering
College of Engineering
Purdue University

Oct 29, 2023

Dear Members of the Faculty Search Committee:

The following persons are willing to write the letter of reference for my application in Civil Engineering at the assistant professor rank.

Dr. Peter B. Flemings
Leonidas T. Barrow Centennial Chair in Mineral Resources and Professor
The University of Texas at Austin
2305 Speedway, JGB, Austin, TX, 78712
pflemings@jsg.utexas.edu
Mobile: +1 512 750 8411

Dr. J. Carlos Santamarina
G. Wayne Clough Chair and Professor
Georgia Institute of Technology
790 Atlantic Dr NW, Atlanta, GA 30332
jcs@gatech.edu
Mobile: +1 404 641 3948

Dr. Thomas Finkbeiner
Research Professor, Ali I. Al-Naimi Petroleum Engineering Research Center
King Abdullah University of Science and Technology
KAUST, Building 5, Sea Side, Level 3, Thuwal, Saudi Arabia, 23955
thomas.finkbeiner@kaust.edu.sa
Mobile: +966 (0) 54 037 8962

Dr. Marco Terzariol
Research Scientist
Ifremer, Institut Français de Recherche pour l'Exploitation de la Mer
Centre Bretagne - ZI de la Pointe du Diable - CS 10070 - 29280 Plouzané
Marco.Terzariol@ifremer.fr
Mobile: +33 (0) 642 39 80 67

Dr. Yi Fang
Machine Learning Engineer
Pilot Company
horusfang@gmail.com
Mobile: +1 562 284 7949

JGR Solid Earth

RESEARCH ARTICLE
10.1029/2023JB026976

Key Points:

- Hydrate-bearing sandy-silts are viscoplastic materials with a relaxation time scale on the order of hours
- The in-situ stress state in hydrate-bearing sandy-silts undergoing burial may be isotropic
- Load-bearing hydrate flow viscously and redistributes the load. A spring-dashpot model captures this behavior

Correspondence to:
A. Cardona,
alejandro.cardona@utexas.edu

Citation:
Cardona, A., Bhandari, A. R., Heidari, M., & Flemings, P. B. (2023). The viscoplastic behavior of natural hydrate-bearing sandy-silts under uniaxial strain compression (K_0 loading). *Journal of Geophysical Research: Solid Earth*, *128*, e2023JB026976. https://doi.org/10.1029/2023JB026976

Received 25 APR 2023
Accepted 18 JUN 2023

Author Contributions:
Conceptualization: Alejandro Cardona, Peter B. Flemings
Formal analysis: Alejandro Cardona, Mahdi Heidari, Peter B. Flemings
Funding acquisition: Peter B. Flemings
Investigation: Alejandro Cardona, Athma R. Bhandari
Methodology: Alejandro Cardona, Athma R. Bhandari, Mahdi Heidari, Peter B. Flemings
Project Administration: Peter B. Flemings
Writing – original draft: Alejandro Cardona, Peter B. Flemings
Writing – review & editing: Alejandro Cardona, Athma R. Bhandari, Mahdi Heidari, Peter B. Flemings

The Viscoplastic Behavior of Natural Hydrate-Bearing Sandy-Silts Under Uniaxial Strain Compression (K_0 Loading)

Alejandro Cardona[1], **Athma R. Bhandari**[1], **Mahdi Heidari**[2], **and Peter B. Flemings**[1,3]

[1]Institute for Geophysics, Jackson School of Geosciences, The University of Texas at Austin, Austin, TX, USA, [2]Bureau of Economic Geology, Jackson School of Geosciences, The University of Texas at Austin, Austin, TX, USA, [3]Department of Geological Sciences, Jackson School of Geosciences, The University of Texas at Austin, Austin, TX, USA

Abstract The in-situ stress state and geomechanical properties of hydrate-bearing sediments impact hydrate formation and gas production strategies. We explore the uniaxial strain compression and stress evolution of natural hydrate-bearing sandy-silts from Green Canyon Block 955 in the deep-water Gulf of Mexico. We performed constant rate of strain uniaxial strain experiments, interrupted by periods where we held the axial stress constant, to explore the vertical deformation and the evolution of the ratio of lateral to axial effective stress (K_0) with time. The hydrate-bearing sandy-silt is stiffer and has a larger K_0 than the equivalent hydrate-free sediment upon loading. During stress holds, the void ratio decreases sigmoidally with the log of time, and K_0 converges to isotropic conditions. We interpret that during loading, the hydrate bears the load and deforms. With time, the hydrate redistributes the load and K_0 increases. We used a viscoelastic model to describe the behavior. The model accurately captures deformation and K_0 trends but does not reproduce all the complex interactions of the hydrate with the porous skeleton. We anticipate that viscous effects within hydrate sediments will impact reservoir compression and stresses during production (hours to days), result in isotropic stress state over geological timescales, and explain the creeping movement in submarine landslides.

Plain Language Summary Natural methane hydrates are ice-like crystalline solids, typically found within and beneath permafrost regions and near the seafloor in the deep ocean. They host large amounts of methane and are envisioned as a potential energy resource, a potential geo-hazard, and an active component in the Earth's carbon cycle. We studied the geomechanical behavior of natural and intact hydrate-bearing sandy-silts recovered from the deep-water Gulf of Mexico. We performed all the experiments at a high pressure and low temperature to maintain the hydrate stable during testing. This study demonstrates that these hydrate-bearing sandy-silts are viscoplastic; deformation and stresses are rate-dependent. Under sustained vertical load, while allowing no lateral deformation, the lateral stress rises with time. This process is known as stress relaxation. Simultaneously, the material undergoes vertical compression with time, a process known as creep. We interpret that these systems deform by hydrate "flowing" and displacing the pore water within the sediment. The hydrate distributes the load in all directions, and stress relaxation takes place. This viscoplastic behavior has important implications for gas hydrate production models, drilling and completing wellbores safely, and may elucidate the mechanisms for submarine landslides.

1. Introduction

Gas hydrates are crystalline solids with gas molecules trapped inside water cavities (Sloan & Koh, 2007). They form at high pressure and low temperature, which delimit their geological occurrence to within and beneath permafrost regions and deep submarine settings (see reviews in Boswell and Collett (2011) and You et al. (2019)). The organic carbon in hydrates is estimated at ~500–2,500 Gt (Milkov, 2004; Ruppel & Kessler, 2017), with high hydrate concentration areas found in sand-rich intervals (Ginsburg et al., 2000). Hydrate deposits have the potential to become an energy resource and are an active component of the global carbon cycle (Collett, 2002; Dickens et al., 1997).

The geomechanical behavior of hydrate-bearing sediments has impacts on the in-situ stress state (Murray et al., 2006), well integrity (Shin & Santamarina, 2017), production behavior of hydrate reservoirs (Moridis et al., 2011; Wu et al., 2020), and seafloor stability (Sultan et al., 2004). For example, hydrate dissociation during production decreases the sediment stiffness and strength (Hyodo et al., 2014; Santamarina et al., 2015; Waite et al., 2009), which in turn causes reservoir compaction and permeability reduction (Rutqvist et al., 2009).

Understanding geomechanical processes in hydrate sediments is critical to assess their response to perturbations, whether caused by climate change or energy production.

The ratio of lateral (σ'_l) to vertical (σ'_v) effective stress under uniaxial strain (K_0) is an important parameter in the analysis of in-situ stresses (Brooker & Ireland, 1965; Mesri & Hayat, 1993).

$$K_0 = \frac{\sigma'_l}{\sigma'_v} \tag{1}$$

K_0 has been widely explored in the geotechnical community (Feda, 1984; Michalowski, 2005), it is commonly determined in the laboratory (Mayne & Kulhawy, 1982), and varies with mineralogy and stress level (Casey et al., 2016). K_0 can also be estimated with semi-empirical relationships; for example, $K_0 = 1\text{-}\sin\phi'$ for normally consolidated sediments (i.e., unloading has not occurred and ϕ' = soil's effective friction angle-Jaky, 1944). Given an estimate of pore pressure and overburden, K_0 is used to calculate the least principal stress in the subsurface (Flemings, 2021).

Three studies document K_0 values for intact hydrate-bearing cores: Fang, Flemings, Germaine, et al. (2022), Yoneda et al. (2022), and Yoneda et al. (2019c) (see Table 1). These studies showed that K_0 varies from 0.4 to 0.45 in hydrate-bearing sands. Yoneda et al. (2022) suggested that the K_0 of the hydrate-bearing sediment is larger than the K_0 of hydrate-free post-dissociated sediment at high stresses. Fang, Flemings, Germaine, et al. (2022) showed that samples with greater K_0 have greater hydrate saturations. Fang, Flemings, Germaine, et al. (2022) and Yoneda et al. (2022) concluded that viscous relaxation of the hydrate phase results in a greater value of K_0 for hydrate-bearing sediments compared to equivalent non-hydrate-bearing sediments. This interpretation of viscous relaxation is supported by creep experiments conducted on polycrystalline methane hydrate (Durham et al., 2003).

Kim et al. (2021) conducted K_0 tests on artificial coarse sand with tetrahydrofuran (THF) hydrate. They found K_0 was less when hydrate was present relative to when it was not. This result contrasts those of Yoneda et al. (2022) and Fang, Flemings, Germaine, et al. (2022) described above. It is not obvious why these results are different; THF and methane hydrate crystals share similar mechanical properties (Lee et al., 2007). However, Kim et al. (2021) did observe an increase in K_0 with time, which they attributed to the creep of the THF hydrate crystals.

The few K_0 measurements made on hydrate-bearing sediments hint that different behavior occurs when hydrate is present than when it is not. This study investigates the geomechanical and viscoplastic behavior of intact hydrate-bearing sandy-silts. We run constant rate uniaxial strain (or one-dimensional compression) experiments (CRS) and measure the lateral stress ratio K_0. In between CRS steps, we hold the axial effective stress constant for ∼1 day to explore the K_0 and deformation with time. We compare the behavior of hydrate-bearing sandy-silt to that of reconstituted specimens of the same material with no hydrate present. We show that hydrate-bearing sandy-silt behave as viscoplastic materials. During stress holds, the void ratio (or porosity) decreases, and K_0 increases with time, converging to isotropic conditions. Conversely, non-hydrate-bearing sandy-silts show no time dependence on K_0 and limited time-dependent compression. We propose a spring-dashpot model to capture these observations. The results presented here suggest the viscoplastic behavior of hydrate-bearing sandy-silts is fundamentally different from the non-hydrate-bearing sediment.

2. Experimental Study: Materials and Methods

2.1. Geological Overview

Green Canyon Block 955 (GC 955) is located at the base of the Sigsbee escarpment in the northern Gulf of Mexico (∼265 km, offshore of Port Fourchon, Louisiana). Seismic analyses and well logging data from the GOM Gas Hydrate Joint Industry Project well (GC 955 H001) revealed the presence of hydrate-bearing sandy-silts in this area (Boswell et al., 2012; Santra et al., 2020). Subsequently, the University of Texas Hydrate Pressure Coring Expedition (UT-GOM2-1) collected pressure cores in GC 955 by drilling two wells within 15 m of the H001 location (i.e., GC 955 H002 and GC 955 H005) (Flemings et al., 2020). The hydrate reservoir at GC955 is composed of two lithofacies: sandy-silt and clayey-silt (Fang et al., 2020; Meazell et al., 2020). Quantitative degassing, P-wave velocities, X-ray scans, and bulk density information suggest the sandy-silt interval contains concentrated hydrate with a saturation (S_h) greater than 80% (Phillips et al., 2020).

Table 1
Pressure Core Analysis Devices Reported in the Literature

Device	Measured properties/ Instrumentation	Maximum axial effective stress[a]	Zero-lateral strain condition	Stress ratio K_0 measurement	Natural sample
Hydrate Autoclave Coring Equipment System in New Tests on Hydrate (HYACINTH)[b,c]	Electrical resistivity P-wave velocities Microbiology cultures	No	No	No	Yes
Instrumented Pressure Testing Chamber (IPTC)[d]	P and S wave velocities Electrical resistivity Cone resistance	No	No	No	Yes
Dynamic Autoclave Piston Corer (DAPC)[e]	X-Ray Quantitative degassing	NA	NA	NA	Yes
Microfocus X-Ray CT (MFXCT)[f]	Micro X-Ray CT	NA	NA	NA	Yes
Transparent Acrylic Cell Triaxial Testing system (TACTT)[g]	Triaxial device Digital image correlation for strain	5 MPa	No	No	Yes
PCATS triaxial[h]	Triaxial device Resonant column	7 MPa	No	No	Yes
Pressure Core Characterization Tools (PCCTS)[i]	Triaxial device (ESC) Direct shear (DSC) Bio-reactor chamber (BIO)	10 MPa	ESC: Quasi-rigid confining cell	No	Yes
High-pressure Oedometer Chamber (HOC)[j,k]	Consolidation	50 MPa	Rigid-wall	Strain-gauge mounted on the cell	Yes
Pore-scale Micro CT[l]	Micro X-Ray CT	NA	NA	NA	Yes
K_0-triaxial[m]	Triaxial device	5 MPa	Quasi-rigid confining cell	Confining pressure	Yes

[a] If equipment stress capacity is not available, we report the maximum axial effective stress shown in the published data. [b] Schultheiss et al. (2006). [c] Schultheiss et al. (2009). [d] Yun et al. (2006). [e] Abegg et al. (2008). [f] Jin et al. (2014). [g] Yoneda et al. (2013). [h] Priest et al. (2015). [i] Santamarina et al. (2012). [j] Yoneda et al. (2022). [k] Yoneda et al. (2019c). [l] Seol et al. (2021). [m] Fang, Flemings, Germaine, et al. (2022).

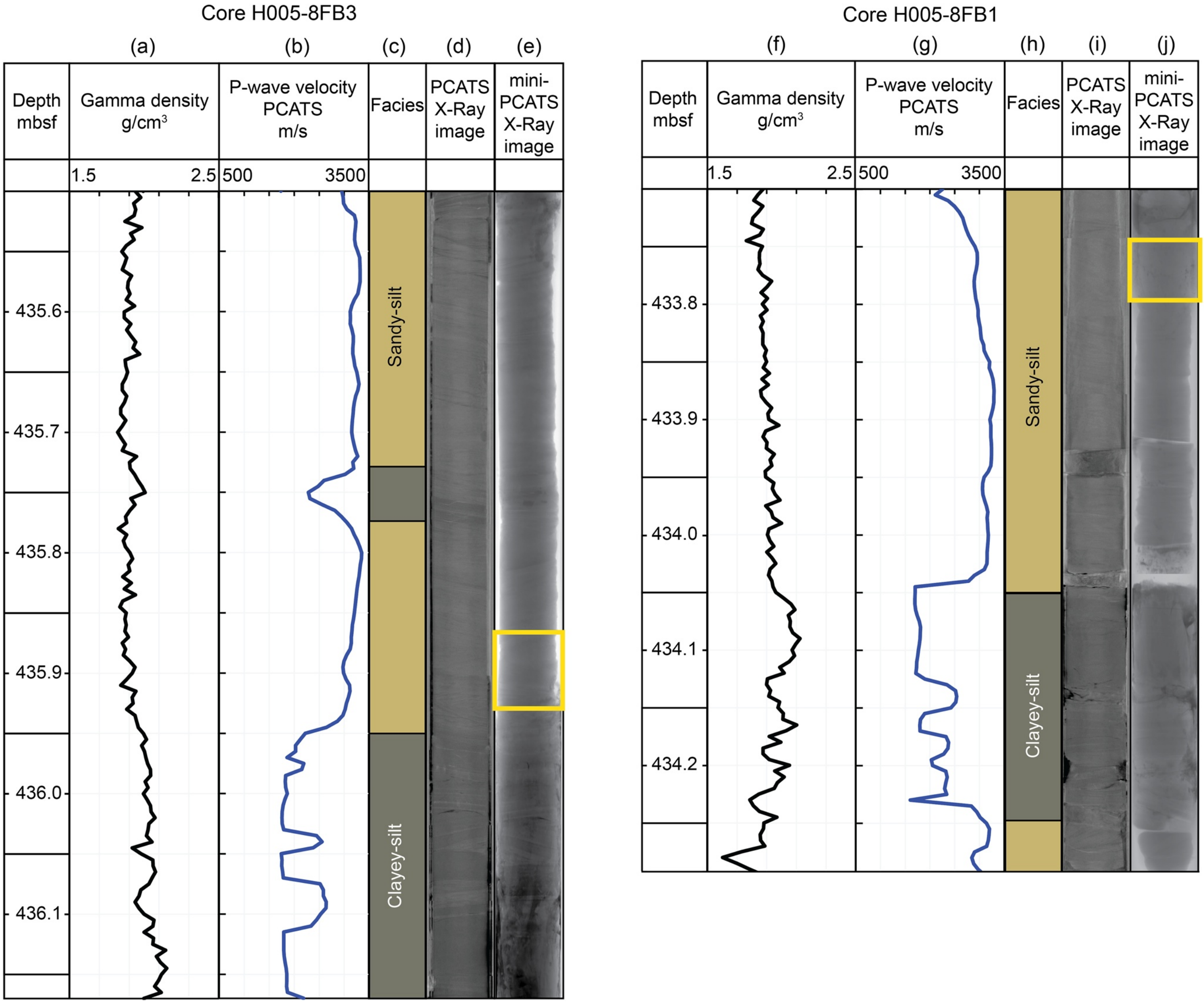

Figure 1. Logs and X-ray images of two intervals of pressure core obtained from PCATS (pressure core analysis and transfer system) for the core H005-8FB3 and H005-8FB1 immediately after coring (a and g) Bulk gamma ray attenuation density. (b and h) P-wave velocities (c and i) Interpreted lithofacies. (d and j) X-ray image. (e and k) X-ray images acquired during this study after several years of storage. The yellow box on the X-ray images indicates the position of the subsample 8FB3-3 and 8FB2-1 tested in this study. Details of PCATS data can be found in Flemings et al. (2020).

2.2. Sample Selection and In-Situ Conditions: GC 955 Hydrate-Bearing Sandy-Silts

We selected sandy-silt samples from core H005-8FB3 and H005-8FB1. The preliminary processing on site of these cores using the Geotek pressure core and transfer system (PCATS) revealed high P-wave velocities and low gamma ray values (Figure 1).

The in-situ vertical effective stress is calculated by subtracting the pore pressure (u) from the overburden stress (σ_v). The water depth at H005 is 2,031.8 m and the hydrate-bearing interval depth ranges from 415 to 449 m below seafloor (mbsf). Then, we integrate the LWD bulk density from GC 955 H001 hole to compute the overburden stress and assume hydrostatic pore pressure (salinity = 3.5 wt. %). The calculated in-situ vertical effective stress $\sigma'_v = \sigma_v - u$ varies from 3.76 MPa (415 mbsf—top) to 4.01 MPa (449 mbsf—bottom). The in-situ pore pressure ranges from 24.6 to 25 MPa.

To estimate the in-situ temperature, we assume the base of the gas hydrate stability (BGHS) is at three-phase equilibrium. We first interpret the BGHS is at 468 mbsf based on the bottom-simulating reflector from the seismic data (details in Flemings et al. (2020)). Then, we estimate a temperature of 20.4°C at the BGHS using

Table 2

Summary of Pressure Cores 8FB3-3 and 8FB1-2 Information and Pressure Core Analysis and Transfer System (PCATS) Scan-Derived Parameters

	8FB3-3	8FB1-2
Lithofacies	Sandy-silt	Sandy-silt
Sample depth, m	435.9	433.8
PCATS P-wave velocity, m/s	3,035	2,928
In-situ vertical effective stress, MPa	3.94	3.92
Initial bulk core volume from X-Ray, cm^3	75.02	66.14
Average sample diameter from X-Ray, cm	4.66	4.40
Volume of solids, cm^3	46.9	25.6
Initial sample length, cm	4.399	4.350
PCATS bulk density, g/cm^3	1.89	1.88
PCATS porosity from bulk density,	0.45	0.46
Gas expelled during dissociation (L)	6.2	3.1

the three-phase diagram curve. The seafloor temperature equals to 4.2°C; therefore, the in-situ temperature ranges between 18.6°C and 19.8°C in the interval cored at GC 955 H005 (i.e., linearly dependent temperature with depth). Table 2 lists the in-situ conditions for the samples tested in this study.

2.3. Specimen Preparation and Test Apparatus (K_0-Triaxial)

Specimen preparation and testing was conducted at 25 MPa inside a cold room ∼6°C. First, pressure cores were connected to the analysis and transfer system (mini-PCATS) for core manipulation. X-ray and P-wave scans were then conducted to identify cores sections that contain hydrates. These sections were sub-sampled using a cutting tool and pushed into the test apparatus (K_0-triaxial) before being transferred to an external chamber. This chamber was pressure-matched, and the ball valve was opened to extrude the sample out of the core liner. The extrusion was complete when the sample was fully surrounded by the butyl rubber membrane, and there was a slight contact with the top steel cap, as measured by the load cell (Figure 2). Fang, Flemings, Daigle, et al. (2022) presents additional details of the specimen preparation and test device.

We used the K_0-triaxial apparatus to measure compression and lateral stress under uniaxial strain. The pressure-balanced drive assembly (not shown in Figure 2) consisted of a servomotor and encoder, and can exert axial effective stress up ∼20 MPa. The lateral stress (or confining stress) was imposed hydraulically and recorded with a pressure transducer (Keller Series 33x-resolution = 10 kPa). Axial displacements were obtained from the piston location; a position encoder tracked the servomotor rotary movement to derive linear displacements (resolution = 0.01 mm). A submersible load cell (GDS-100 kN-resolution = 0.1 kN) compensates for fluid pressure, thus, axial effective stresses were measured directly. We independently controlled three hydraulic pumps (Quizix Q600): confining pump P_C for lateral stress, sample pump P_S for pore pressure, and piston pressure P_P. The K_0-triaxial was calibrated using a steel sample to account for apparatus compressibility in displacement measurements.

We imposed uniaxial strain by adjusting the confining pressure to maintain constant sample area (A_{sample}). The area A_{sample} was obtained from averaging the specimen diameter observed in the X-ray images (Figures 1e and 1k). Our approach, which is widely used in the geotechnical field, assumed the volume change ΔV in the sample equals the volume of pore fluid expelled measured by the pump. This assumption implies the solid grains and the fluid are incompressible. During uniaxial strain, this volume change must equal the axial displacement multiplied by the cross-sectional area (A_{sample}). Therefore, throughout the test, the confining pump injected or withdrew fluid to ensure that the volumetric change equals the axial displacement multiplied by A_{sample} (i.e., $\Delta V = A_{\text{sample}}\ \Delta L$).

2.4. Compression: Loading, Stress Holds, and Hydrate Dissociation

We first compressed specimens to an isotropic effective stress of ∼0.4 MPa at a pore pressure of 25 MPa using the confining pressure and the piston. This seals the membrane. Then, we axially loaded specimens at a constant strain rate (CRS) of ∼1%/hr while measuring deformation and lateral stress, and allowing fluid to drain from both ends of the sample. During this CRS-loading phase, we held the axial total stress constant three times and monitored the axial deformation and lateral stress with time (gray regions, Figure 3). Then, specimens were unloaded both axially and laterally to zero effective stresses and the pore pressure was lowered from 25 to 5 MPa to move toward near the hydrate phase boundary.

Hydrate dissociation was conducted using stepwise depressurization. We decreased the pore pressure with a back-pressure regulator (BPR) and monitored the amount of gas expelled in a bubbling chamber at each step. When hydrate dissociation was complete, water was flowed through the specimen, and removed it from the K_0-triaxial for additional characterization.

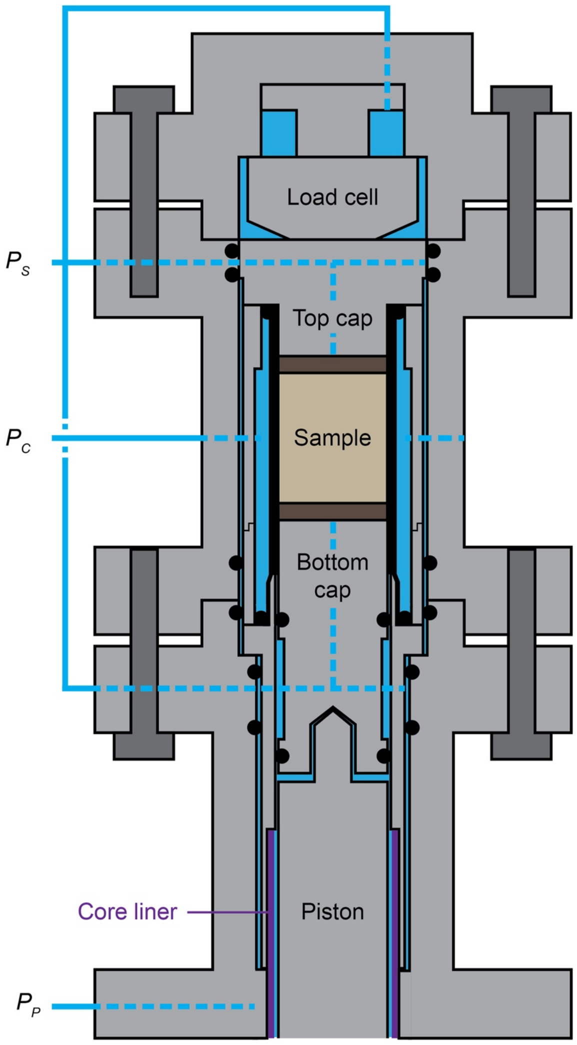

Figure 2. The K_0-triaxial is a triaxial device designed to conduct uniaxial strain compression tests in pressure cores. The device is connected to three independent hydraulic pumps: confining pressure P_C, sample pressure P_S and piston pressure P_P.

2.5. Depressurized Sediment: Index Properties

The total mass of solids and the moisture and density (MAD) porosity was measured in order to back-calculate the void ratio e (or porosity $n = e/(1 + e)$) during the test. Additional index properties were obtained for the dissociated samples, including liquid limit (Casagrande method), grain size distribution from laser diffraction, and grain density with a pycnometer.

2.6. Reconstituted Samples: Compression, Lateral Stress, and Creep

We processed the sandy-silt lithofacies from degassed pressure cores from the same hydrate reservoir and used this material to conduct compression tests without hydrate. This approach avoids the effects of fine migration (Fang, Flemings, Daigle, et al., 2022), and eliminates sample variability, producing a uniform bulk material representative of the sandy-silt lithofacies (Casey et al., 2016). This reconstitution approach homogenizes the sediments and any layering is lost.

First, each core was oven-dried at 105–110°C, gently crushed with a pestle to break aggregates, and dried again to remove the moisture trapped inside the aggregates. Then, we measured the grain size distribution using laser diffraction to confirm the lithofacies. We used the blending method to mix the different cores in a controlled manner and thereby create a homogeneous mixture (Germaine & Germaine, 2009). We term this batch as Reconstituted Green Canyon Sandy-Silt (RGCSS). Table 3 lists the index properties gathered for this material, measured following ASTM guidelines: liquid (w_L) and plastic (w_P) limits with Casagrande cup and rolling (ASTM, 2018), grain density in a pycnometer (ASTM, 2016), and mineralogy by X-ray powder diffraction.

We measured the compression behavior of the sandy-silt lithofacies without hydrate using a triaxial cell (GDS HP14/76). The oven-dried material was reconstituted using dry pluviation (Germaine & Germaine, 2009). Then, specimens were saturated with a 3.5 wt.% natural sea salt brine and back/pore pressure was increased to 0.34 MPa and confining pressure to 0.50 MPa. Next, we uniaxially loaded the specimens at a constant lateral stress rate ~0.24 MPa/hr. This protocol slightly differed from the K_0-triaxial; the built-in software ramps the lateral stress and adjusts the axial strain ε_a to

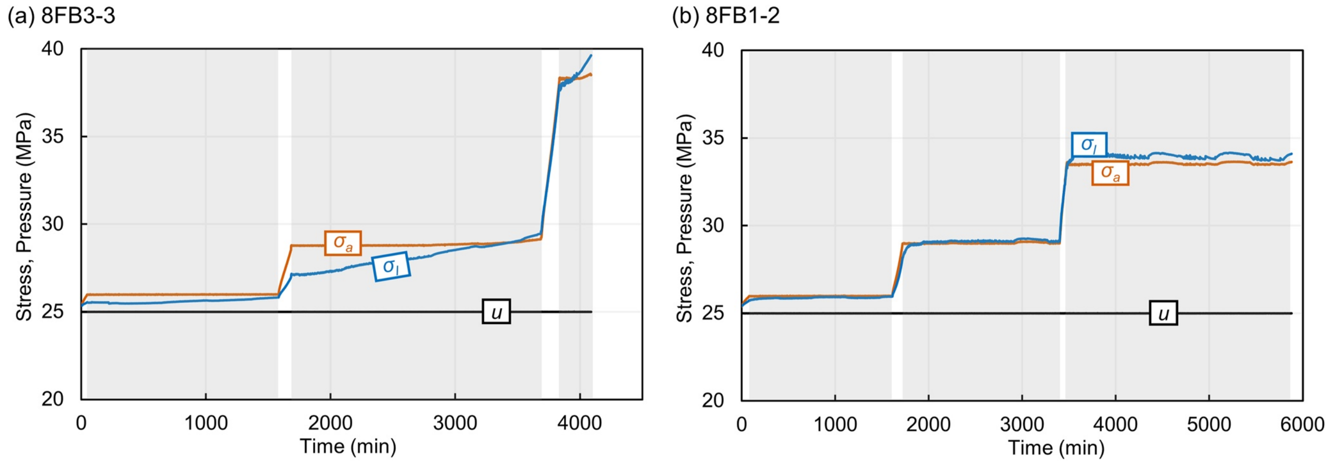

Figure 3. Compression test program for the pressure core sample (a) 8FB3-3 and (b) 8FB1-2 (pore pressure u; total axial stress σ_a; total lateral stress σ_l).

Table 3
Index Properties and X-Ray Diffraction (XRD) Mineralogy of the Reconstituted GC955 Sandy-Silt Lithofacies (RGCSS)

		RGCSS
Clay fraction by grain size (<2 μm), %		5
D_{50}, μm		48
Liquid limit, w_L		23.0
Plastic limit, w_P		19.5
Grain density ρ_g, g/cm^3		2.675
Mineralogy by XRD Analysis, %	Quartz	44
	Plagioclase	18.7
	K-feldespar	11.1
	Calcite	4.7
	Dolomite	8.2
	Pyrite	0.1
	Halite	0.1
	Amphibole	1.9
	Muscovite	0.9
	Chlorite (Tri)	1.6
	Illite + Smectite	8.7

match the volumetric strain ε_v. Consolidation was complete when the lateral effective stress reached σ_l ~8 MPa, which corresponded to an axial effective stress of σ_a ~14 MPa. This uniaxial strain procedure does not allow us to perform stress holds. We conducted one uniaxial compression test with stress hold at σ_a ~1.9 MPa using a radial strain sensor. After the uniaxial consolidation, the specimen was sheared under drained conditions at a constant strain rate of 3.6%/hr. We conducted three shear tests to obtain the friction angle.

We obtained the secondary compression coefficient $C_\alpha = \Delta e/\Delta \log(t)$ of the sandy-silt material using an oedometer following an incremental loading protocol. The sample preparation consisted of dry-pluviation inside a rigid wall ring, and the specimen saturation was conducted with a 3.5 wt.% natural sea salt brine and back/pore pressure of 0.34 MPa. The incremental loading test was performed by applying a series of constant stress levels to the specimen using a load-increment-ratio of 1 (i.e., the load is doubled each time), where each increment was maintained for 1–24 hr and the axial deformation was monitored with time.

3. Results

3.1. In-Situ Porosity

The in-situ porosity (n) of the sandy-silt lithofacies in GC 955 is $n = 0.38$ at an in-situ vertical effective stress of 3.8 MPa (details in Fang et al. (2020)). We assume this porosity for our samples (8FB3-3 and 8FB1-2) at the end of the second stress hold ($\sigma'_a \approx 3.8$ MPa). We attempted to measure porosity directly using two methods: total volume of solids and sample, and back-calculated from moisture and density porosity. However, both techniques resulted in unreliable values due to significant sample disturbance. Porosities derived from PCATS gamma ray bulk density are greater than the in-situ porosity (Table 1), which indicates volumetric compression from a zero-effective stress condition during PCATS scanning to a loaded in-situ state.

3.2. Compression

3.2.1. Void Ratio During Compression

The compression behavior for samples 8FB3-3 and 8FB1-2 is illustrated in Figure 4a (blue and red curves). The void ratio decreases with the log of axial effective stress following a concave-down curvature. The slope of these curves is the compression index (C); we do not distinguish if the sediment has been subjected to axial stresses above or equal to the in-situ effective stress. C increases with stress by a factor of ~2 (Figure 4a). Immediately after the stress holds, both samples are initially stiffer (flatter e vs. log σ'_a slope), and as the loading continues, the slope steepens and approaches the general compression trend. Sample 8FB1-2 shows an apparent softer behavior (i.e., higher C) before $\sigma'_a = 1$ MPa compared to 8FB3-3, which diminishes after the first stress hold.

The reconstituted, hydrate-free, sandy silt sample also exhibits a concave downward compression curve (Figure 4a, black curve) and the compression index C increases by a factor of ~3 during the test. These C values are greater than the hydrate-bearing samples at axial effective stresses above 1 MPa. Thus, the hydrate-free samples are more compressible than the pressure cores.

3.2.2. Hydrate Saturation During Compression

The saturation for sample 8FB1-2 increases from ~0.68 to ~0.82 at the end of the test (Figure 4b). For sample 8FB3-3, the hydrate saturation derived from the expelled gas and pore volume yielded unrealistic saturations. The volume of gas expelled was much larger than expected, resulting in hydrate saturation $S_h \approx 1.3$ at in-situ stress. We interpret that loose hydrate produced during cutting remained trapped inside the piston pressure chamber in the K_0-triaxial but was not extruded inside the membrane (see Figure 2). Alternatively, dissolved methane in the water during long-term storage could have been transferred into the K_0-triaxial and result in unaccounted methane. Therefore, we assume the in-situ hydrate saturation of sample 8FB3-3 is $S_h = 0.85$ based on extensive previous

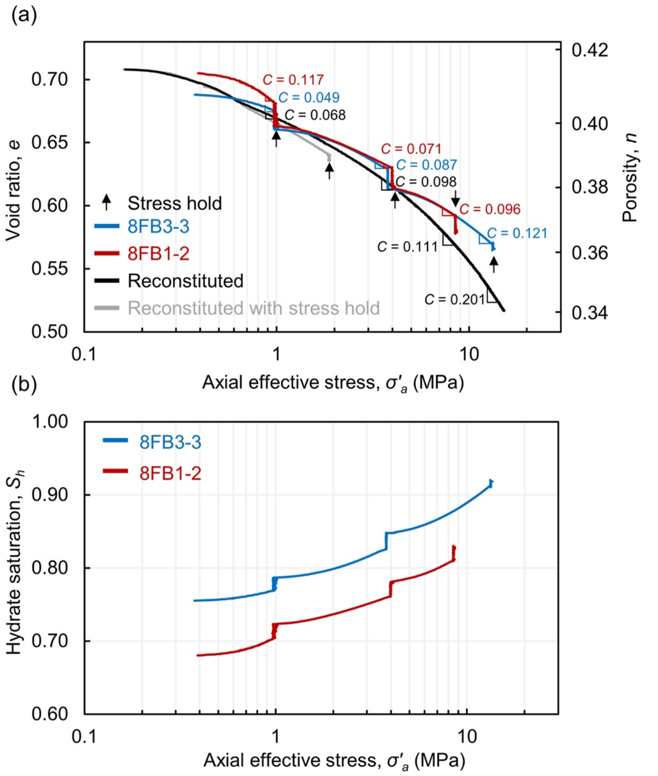

Figure 4. (a) Evolution of void ratio *e* and with axial effective stress σ'_a during uniaxial strain compression for pressure core samples 8FB3-3 (blue) and 8FB1-2 (red), and reconstituted sandy-silt material (black). The compression is paused three times in the pressure cores, holding the axial stress constant while maintaining uniaxial strain conditions (stress hold-black arrows). One reconstituted sandy-silt test included a stress hold at the end of the compression phase (gray). (b) Hydrate saturation of the samples 8FB3-3 and 8FB1-2 with axial effective stress. We assumed hydrate and solid grains are incompressible and the hydrate loss via dissolution is small.

measurements of this lithofacies (Fang, Flemings, Daigle, et al., 2022; Fang, Flemings, Germaine, et al., 2022; Phillips et al., 2020, 2022). Given this assumed in-situ saturation at 3.8 MPa, the saturation increases from $S_h \approx 0.85$ ($\sigma'_a = 3.8$ MPa) to $S_h \approx 0.95$ ($\sigma'_a = 13$ MPa) during the test.

3.2.3. Compression With Time

During the stress holds (black arrows, Figure 4a), the void ratio decreases significantly for the hydrate-bearing specimens. The ratio of the void ratio loss during the CRS compression phase (Δe_{CRS}) relative to that during the subsequent stress hold ($\Delta e_{\sigma\text{-hold}}$) decreases with stress, with $\Delta e_{\sigma\text{-hold}}/\Delta e_{\mathrm{CRS}} = 1.1$, 0.5, and 0.1 for sample 8FB3-3 and 0.7, 0.4, and 0.6 for sample 8FB1-2. The loss in void ratio is much smaller for the non-hydrate-bearing reconstituted material, with $\Delta e_{\sigma\text{-hold}}/\Delta e_{\mathrm{CRS}} = 0.06$.

We define the stress-hold compression index ($C_{\sigma\text{-hold}} = \Delta e/\Delta \log(t)$) to characterize the time-dependent deformation rate in the hydrate-bearing samples. We avoid the use of the secondary compression coefficient C_α used in the geotechnical community (Lambe & Whitman, 1969), as C_α is derived from incremental loading tests.

During a stress hold, the void ratio with log time is sigmoidal (Figure 5): it is initially fairly flat, then steepens, and eventually levels off. Thus, $C_{\sigma\text{-hold}}$ starts at low values, gradually increases over time, and ultimately decreases. The maximum stress-hold compression index ($C^{\max}_{\sigma-\mathrm{hold}}$) at a given stress hold remains constant in the first and second stress hold (Figures 5a–5b and 5d–5e), but decreases in the last stress hold (Figures 5c and 5f).

We compare the $C_{\sigma\text{-hold}}$ evolution in the sediment containing hydrates to the C_α in the non-hydrate-bearing sandy-silt obtained from incremental loading tests. Figure 6a shows the void ratio versus log(*t*) is linear for the reconstituted material; thus, $C_\alpha = 0.006$ is constant with time. This value is lower than the $C^{\max}_{\sigma-\mathrm{hold}}$ measured in the hydrate-bearing intact sample at a similar stress level; $C^{\max}_{\sigma-\mathrm{hold}} = 0.010$ in the second stress hold for sample 8FB3-3 (Figure 6a).

3.3. Lateral to Axial Effective Stress Ratio (K_0)

3.3.1. K_0 During Compression

Figure 7 illustrates the evolution of the stress ratio K_0 with effective stress for the hydrate-bearing samples. Pressure core samples are axially loaded from an initial isotropic condition ($K_0 \approx 1.0$). As the load increases, the stress ratio decreases to $K_0 \approx 0.55$ (8FB3-3) and 0.74 (8FB1-2) at $\sigma'_a = 1$ MPa. During the first stress hold ($\sigma'_a = 1$ MPa), K_0 increases to 0.85 (8FB3-3) and 0.94 (8FB1-2). Once loading is restarted, the stress ratio decreases to 0.56 (8FB3-3) and 0.79 (8FB1-2) at the in-situ axial effective stress ($\sigma'_a = 3.8$ MPa) and increases toward isotropic conditions during the second stress hold. K_0 remains near 1.0 during further increments in stress and slightly increase above 1.0 during the third stress hold.

We compare the K_0 behavior of the hydrate-bearing specimens with the reconstituted sandy-silt material without hydrate. K_0 for the hydrate-free sample shows a gradual decrease from isotropic conditions and then remains fairly constant $K_0 \approx 0.51$ during compression (black line, Figure 7). The K_0 in the hydrate-bearing samples converges to higher values than in the non-hydrate-bearing samples in the CRS loadings (blue and red lines, Figure 7).

3.3.2. K_0 With Time and Stress Relaxation

During stress holds, K_0 in the hydrate-bearing sandy-silt increases with time in all cases (Figure 5). However, the increase in K_0 is delayed in sample 8FB3-3 relative to sample 8FB1-2. K_0 rise starts at ~100–400 min (black dot in Figures 5a–5c), after more than half the compression has occurred (Δe in Figures 5a–5c). This K_0 increase in 8FB3-3 occurs very rapidly toward isotropic conditions (Figures 5a and 5b). 8FB1-2 shows a gradual K_0 increase over time without the delay response (Figures 5d–5f). K_0 remains near or slightly above 1.0 in the third stress

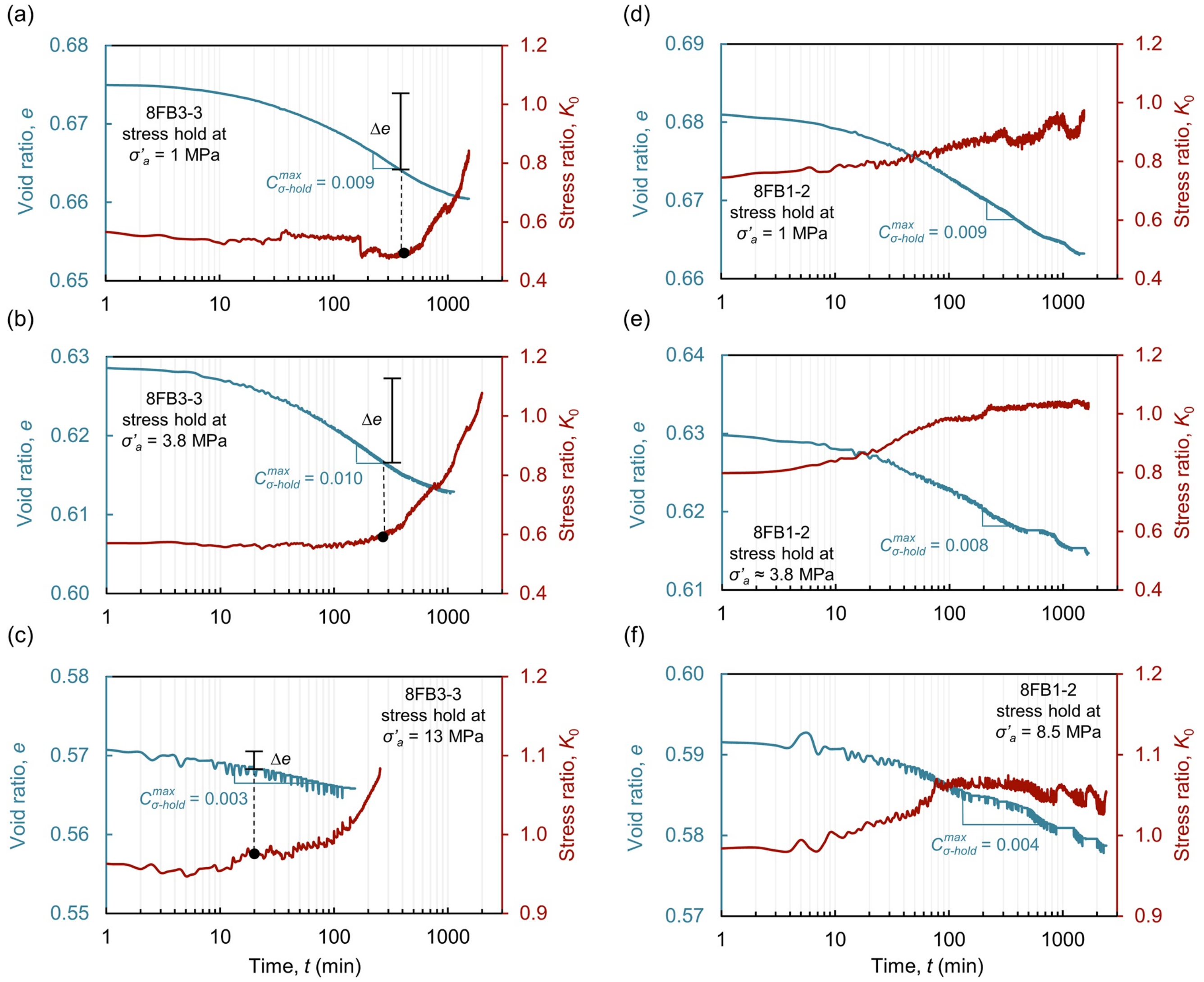

Figure 5. Time-dependent evolution of the void ratio (blue) and stress ratio K_0 (red) during the stress holds at (a) 1 MPa, (b) 3.8 MPa, (c) 13 MPa for sample 8FB3-3, and at (d) 1 MPa, (e) 3.8 MPa, (f) 8.5 MPa for sample 8FB1-2. The initial time corresponds to the beginning to the stress hold. The $\boldsymbol{C^{max}_{\sigma-hold}}$ denotes the maximum stress hold compression index during a stress hold. The onset for the K_0 rise in 8FB3-3, shown as a black dot in (a–c), occurs at 400, 250 and 20 min for stress-holds $\sigma'_a = 1.0$, 3.8, and 13 MPa, respectively. Over half the compression Δe occurs before the K_0 rise. Sample 8FB2-1 does not display the delayed K_0 response. The stress relaxation times, defined as $1/e$ of the initial deviatoric stress, are $\tau_\sigma \approx 25$, 18, 1 and 12, 1, 0.2 hr for sample 8FB3-3 and 8FB1-2, respectively.

hold for both samples (Figures 5c and 5f). We attribute the K_0 greater than 1.0 to potential experimental errors in the uniaxial strain protocol, possibly due to an underestimated sample diameter or unaccounted equipment compressibility (Appendix B).

The evolution of K_0 with time for the reconstituted sandy-silt is shown in Figure 6b. $K_0 \approx 0.53$ and is constant with time for the entire stress hold at $\sigma'_a = 1.9$ MPa. This is very different from the hydrate-bearing sandy-silt behavior, where K_0 increases with time toward isotropic conditions (e.g., Figures 5 and 6b).

We define the timescale of stress relaxation τ_σ as the time when the deviatoric stress $q = \sigma'_a(1 - K_0)$ is equal to $1/e$ of the initial value $q^{t=0}$ in each stress-hold. Alternatively, this is equivalent to the time when $K_0 = 1 - (1 - K_0^{t=0})/e$. These stress relaxation times are $\tau_\sigma \approx 25$, 18, 1 and 12, 1, 0.2 hr for sample 8FB3-3 and 8FB1-2, respectively (Figure 5).

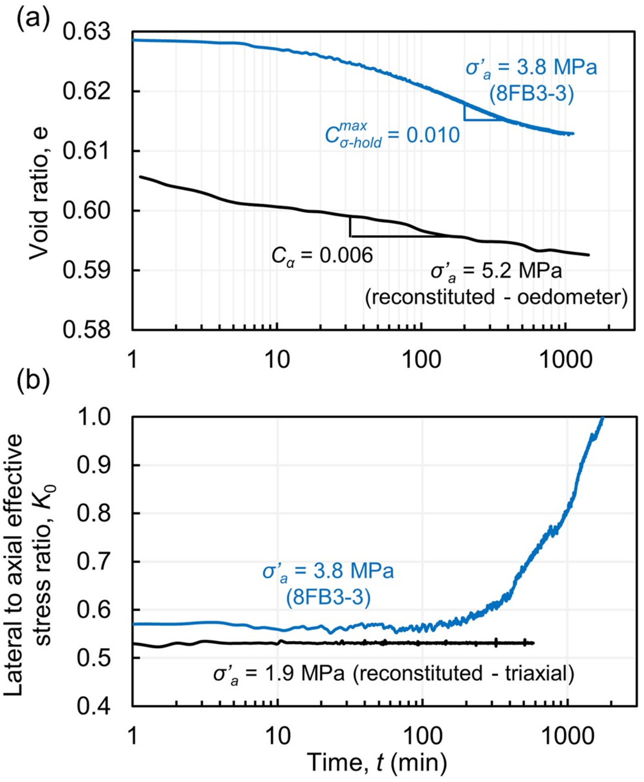

Figure 6. Time-dependent compression and stress ratio K_0 behavior for the reconstituted sandy-silt measured with an oedometer and triaxial cell, respectively. 8FB3-3 data for the second stress hold is superimposed. (a) Void ratio with time at a given axial effective stresses. (b) K_0 evolution with time.

4. Discussion

4.1. Compression Behavior

4.1.1. GC 955 Hydrate-Bearing Sandy-Silts Compression—Comparison

We compare our results to previous work describing the compression behavior of hydrate-bearing cores from the same sandy-silt hydrate reservoir (Figure 8). These previous data were gathered using incremental loading (circles, Figure 8). All of the data show compression curves that are concave-down in semi-log space, including the reconstituted sandy-silt. This concave downward curvature is characteristic for silts and sands and it is attributed to grain sliding, rolling and crushing (Pestana & Whittle, 1995). Samples that are slightly coarse display less compression for a given stress level relative to those that are slightly finer, as measured by the mean grain diameter D_{50}.

4.1.2. CRS Compressibility of Hydrate-Bearing Sandy-Silts

We fit the hydrate-bearing CRS-compression curves with a polynomial to examine the compression behavior without the stress-hold deformation (Figure 9a). The slope of the polynomial is the compression index C (Figure 9b). C of the non-hydrate-bearing sample is higher in almost all cases than the hydrate-bearing specimens (Figure 9b). The hydrate-bearing material behaves more stiffly than the non-hydrate-bearing specimens. We interpret the 8FB1-2 high compressibility below $\sigma'_a = 1$ MPa is due to compression of loose sediment; thus, the fitted polynomial starts at slightly lower void ratio.

4.1.3. Uniaxial Deformation With Time in Hydrate-Bearing Sandy-Silts

The hydrate-bearing samples deform significantly during the stress holds (Figure 5), with its deformation rate described by $C_{\sigma\text{-hold}}$. The maximum deformation rate in each stress hold ($C^{\max}_{\sigma-\text{hold}}$) decreases with stress (Figure 10a). This trend contrasts the non-hydrate-bearing sandy-silt behavior, where C_α does increase with stress level, ranging from 0.002 to 0.007 (Figure 10a).

We characterize the time-dependent deformation with the ratio of $C_{\sigma\text{-hold}}/C$. The analogous C_α/C ratio is fairly constant for a given material without hydrate and of order ~0.025 for sands and ~0.06 for organic clays (Mesri & Castro, 1987; Mesri & Godlewski, 1977). Our measurements of C_α/C for the reconstituted sandy-silt with no hydrate is ~0.03 (Figure 10b), and thus reflects the generally expected behavior for sediment without hydrate. By contrast, the $C_{\sigma\text{-hold}}/C$ ratio in hydrate-bearing sandy-silts is initially much larger and declines dramatically with increasing stress to ~0.03 (Figure 10b).

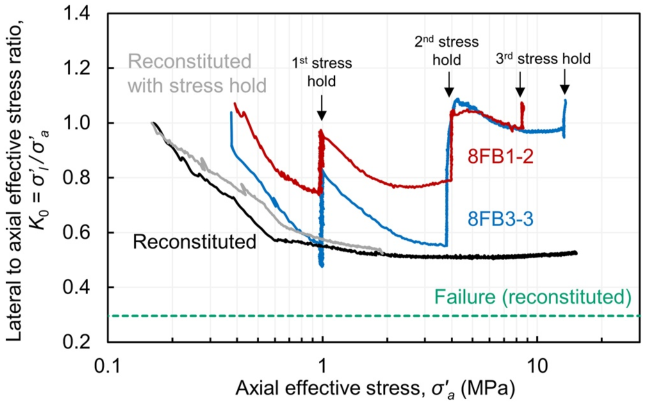

Figure 7. Evolution of the lateral to axial effective stress ratio (K_0) during uniaxial strain compression (blue: 8FB3-3, red: 8FB1-2, black and gray: reconstituted sandy-silt material from the same hydrate reservoir). The stress ratio at failure $K_f = (1 - \sin\phi')/(1 + \sin\phi')$ for the reconstituted material is superimposed.

Previous incremental loading tests in hydrate-bearing samples from GC 955 report a C_α that increases with time, and decreases with stress level (Yoneda et al., 2022). Yoneda et al.'s data follow the same stress and time trends and are in close agreement with our measured values; for instance, C_α is 0.01 ($\sigma'_a = 2$ MPa), 0.08 ($\sigma'_a = 3.8$ MPa) and 0.003 ($\sigma'_a = 10$ MPa).

During a stress hold, the change in void ratio with log time is sigmoidal for hydrate-bearing sandy-silts and linear for non-hydrate-bearing sediments (Figure 6a). In fact, the hydrate-bearing material compresses in a manner that is similar to primary consolidation in response to a step load: deformation steepens and then flattens with the log of time, as overpressured water is expelled out of the pores (Craig, 2005). However, the time scales of this dissipation are much longer than expected for primary consolidation. For example, the excess pore pressure Δu in a CRS test with axial strain rate $\dot{\varepsilon}_a$

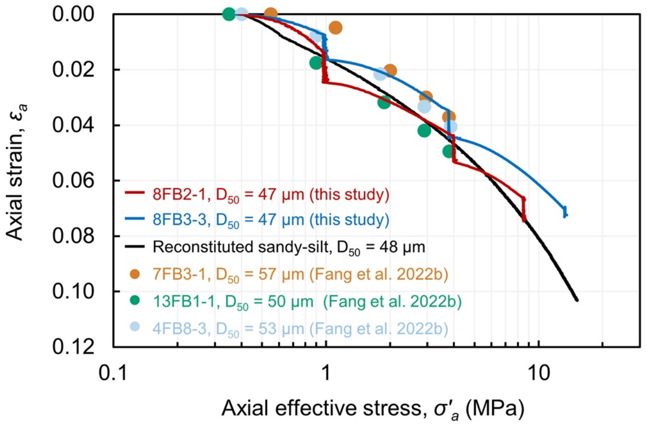

Figure 8. Uniaxial strain compression of natural and intact hydrate-bearing samples from the Gulf of Mexico GC 955. Data gathered in this study (blue line: 8FB3-3, red line: 8FB1-2) is superimposed with data obtained by Fang, Flemings, Germaine, et al. (2022) (filled circles; orange: 7FB3-1, green: 13FB1-1, light blue: 4FB8-3). The reconstituted sandy-silt compression without hydrate is shown as a black line.

and initial drainage length H_0 (= half sample length for our test conditions) is (ASTM, 2012)

$$\Delta u = \frac{\dot{\varepsilon}_a H H_0 \eta}{2k} \tag{2}$$

where H is the drainage length throughout the test, η is fluid viscosity and k is the effective water permeability (i.e., the permeability of water in the presence of hydrate). We use the lowest effective permeability ($k \approx 7 \times 10^{-17}$ m^2) reported in Fang, Flemings, Daigle, et al. (2022) and find that the excess pore pressure is less than 1% of the applied axial stress. Thus, since the effective stress at the end of the CRS-loading and at "infinite" time shows only a minor change, any strain resulting from overpressure water during the stress hold is unlikely.

We interpret that the sigmoidal shape of the compression curve records the viscoplastic deformation of the hydrate within the sediment pores. Upon loading, the pore-filling hydrate crystal bears a significant fraction of the applied load (Figure 11a). With time, the hydrate flows viscously into the space vacated by the expelled pore water (Figure 11b). As this occurs a fraction of the load is transferred from the hydrate to the solid framework.

4.2. Lateral Stress Behavior

During constant strain-rate loading, the lateral stress ratio (K_0) in the hydrate-bearing samples converges to a value higher than is observed in the non-hydrate-bearing sediment during CRS-loading (Figure 12). At axial effective stresses greater than 1 MPa, these values are higher than those measured by Fang, Flemings, Germaine, et al. (2022) during incremental loading (circles, Figure 12). For example, at in-situ vertical effective stress of 3.8 MPa, the $K_0 \approx 0.56$ (8FB3-3) and 0.79 (8FB1-2) and Fang, Flemings, Germaine, et al. (2022) measurements suggested $K_0 \approx 0.40$ to 0.46. Yoneda et al. (2022) obtained $K_0 \approx 0.40$ for similar sediments during incremental loading. We interpret the differences between our results and these studies can be attributed to two effects. First, the viscous behavior implies the K_0 changes as a function time or strain rate; thus, different hold-times between incremental loading and stress-hold periods would result in different K_0. Furthermore, each experimental apparatus or testing technique has its own limitations, which can affect measured values (Section 4.5).

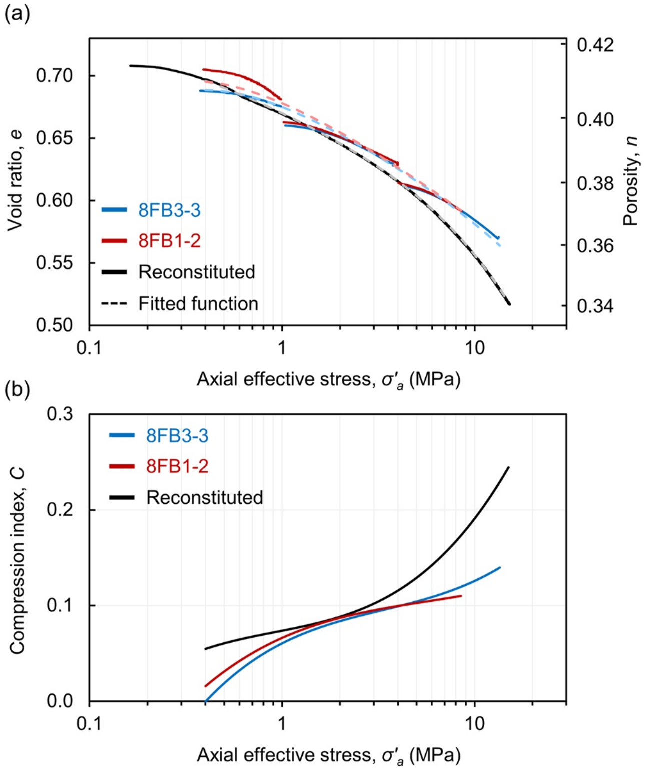

Figure 9. (a) Compression behavior for the pressure core 8FB3-3 (blue), 8FB1-2 (red), and reconstituted sandy-silt (black). The compression curves are fitted with a fourth-degree polynomial (dashed lines). (b) Compression index *C* of the fitted polynomials.

We interpret that upon loading, the hydrate crystal bears a significant fraction of the applied load (Figure 12a). With time, the hydrate relaxes toward an isotropic state ($K_0 = 1.0$). During this process, the hydrate distributes the load, and increases the lateral stress relative to the vertical stress, which results in an increase in K_0 (Figure 11b). The K_0 rise onset roughly correlates with the start of the diminishing $C_{\sigma\text{-hold}}$ stage in sample 8FB3-3. In contrast, for sample 8FB1-2, deformation and K_0 increase occur simultaneously (Figure 5). In this case, the load-bearing hydrate transfers load while viscously flowing.

4.3. Viscoelastic Model for Hydrate-Bearing Sandy-Silts

We present a spring and dashpot model to explore the mechanical behavior of hydrate-bearing sandy-silts. We consider two elements in parallel: the elastic element representing the soil skeleton, and the viscoelastic element representing the hydrate skeleton (Figure 13). This lumped-element model captures both stress relaxation and creep (Findley et al., 1976), and has been suggested to represent viscoelastic behavior in geomaterials (Hagin & Zoback, 2004;

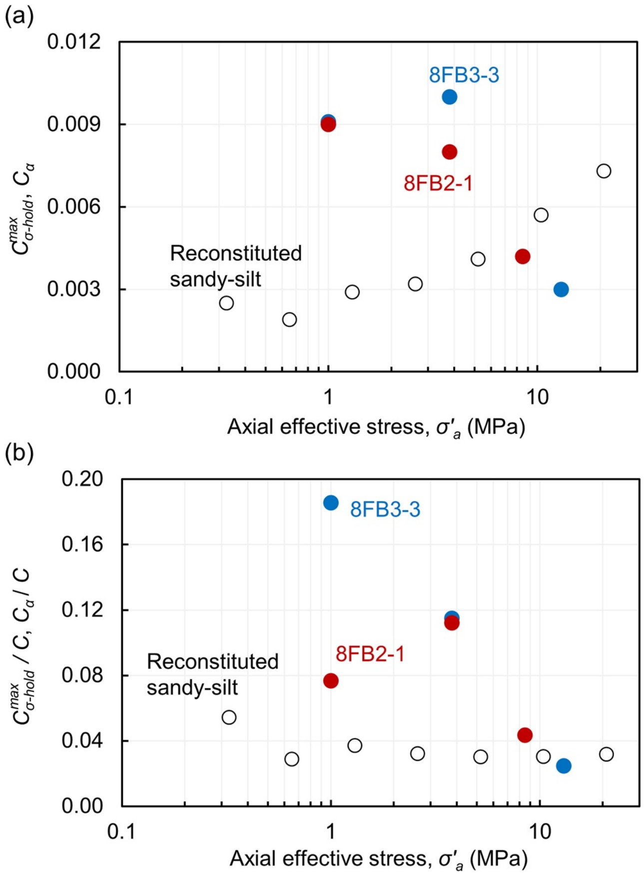

Figure 10. (a) Evolution with stress of the secondary compression coefficient C_α (reconstituted sandy-silt - black circles) and maximum stress-hold compression index $C^{\max}_{\sigma-\text{hold}}$ (hydrate-bearing samples - blue and red circles). (b) Ratio of C_α and $C^{\max}_{\sigma-\text{hold}}$ with respect to the compression index (C) We use the C-values shown in Figure 4 to calculate $C^{\max}_{\sigma-\text{hold}}/C$ and C_α/C.

Mavko et al., 2009). The model parameters shown in Table 4 represent fitting quantities rather than true material properties. The governing equations and numerical scheme are presented in Appendix A.

We obtain the elastic soil skeleton parameters (E^s, ν^s) using the reconstituted sandy-silt measurements. Then, we use the 8FB3-3 data from the second CRS loading ($\sigma'_a = 1.0$–3.8 MPa) and stress-hold ($\sigma'_a = 3.8$ MPa) to find the hydrate skeleton parameters (the viscoelastic arm of the model-Figure 13b). We adopt a very high volumetric viscosity η^h_{vol}, thus its contribution is negligible to model results. The asymptotic strain value during the stress hold constrain the elastic hydrate constants (E^h, ν^h), while the shear viscosity η^h_{sh} dictates the rate at which deformation and stresses change.

The model captures the compression behavior of the sediment effectively (Figures 14a and 14c). The modeled sediment with hydrate (yellow line, Figure 14a) follows the measured data (blue line, Figure 14a). The modeled behavior of the hydrate-free material (green line, Figure 14a) fits the reconstituted sandy-silt data. Both model and data reveal that the hydrate-bearing sample is stiffer than the hydrate-free sediment. The time-dependent compression model (yellow line, Figure 14c) clearly captures the sigmoidal shape of the compression whereas the modeled strain of the hydrate-free material does not change with time (green line, Figure 14c).

The CRS-compression phase starts from near-isotropic stress conditions. As the material is loaded under uniaxial strain, the K_0 gradually declines (blue line, Figure 14b). The model captures this decline in K_0 with stress (yellow line, Figure 14b), and reaches a value higher than that of the non-hydrate-bearing sediment (black line, Figure 14b). The hydrate-free model (green line, Figure 14b) gradually approaches the reconstituted data (black line, Figure 14b), and converges toward a lower K_0 relative to the modeled trend for the hydrate (yellow line, Figure 14b).

During the stress hold, the modeled K_0 increases with time (yellow line, Figure 14d). In contrast, K_0 modeled without hydrate does not change with time (green line, Figure 14d). This is because we have not included a viscous component in the soil skeleton (Figure 13b). The model with hydrate predicts the K_0 will asymptote to a constant value with time. This asymptotic value depends on the initial soil and hydrate stresses and combines the K_0 in each component; K_0 in the hydrate skeleton will reach 1.0 whereas in the soil skeleton, K_0 reaches a value of $\nu^s/(1 - \nu^s)$, where ν^s is the Poisson's ratio (Table 4).

The relaxation time τ is the ratio of viscosity to shear modulus (Poirier, 1985). Given the parameters in Table 4, $\tau \approx 2$ hr. This value correlates with the time when $C_{\sigma\text{-hold}}$ reaches its maximum value ($C^{\max}_{\sigma-\text{hold}}$-Figure 5). This analysis suggests that there would be considerable stress relaxation and creep over short time scales (i.e., within a day).

The spring-dashpot model captures much of the behavior that we observe, but is not complete. The viscosity in the model is constant; however, the decrease in stress relaxation time τ_σ with initial deviatoric stress (q_0) may indicate a stress-dependent viscosity (e.g., $\tau_\sigma = 25$ and 18 hr for $q_0 = 0.5$ and 1.7 MPa). In fact, a range of studies in quartz, ice, pure hydrate and hydrate-bearing porous media document a power-law rheology, $\dot{\varepsilon} = Aq^n$ (Alley, 1992; Durham et al., 2003; Hirth et al., 2001; Yoneda et al., 2022): the viscosity depends on the deviatoric stress. In addition, we observe that $K_0 = 1$ with time; however, the model predicts some deviatoric stresses will be preserved. The model also anticipates that K_0 rises with increasing deformation, while the experimental data are equivocal: K_0 in 8FB3-3 increases significantly later than the deformation does whereas in 8FB1-2, K_0 does rise simultaneously with deformation (Figure 5). Ultimately, the separation of the material behavior to a spring-dashpot model cannot capture some of the complex interactions of the hydrate with the porous skeleton. Fang, Flemings, Germaine, et al. (2022) and Flemings et al. (2022) have suggested a slightly different conceptual model wherein the loading of hydrate-bearing material is akin to undrained loading of water saturated sediment.

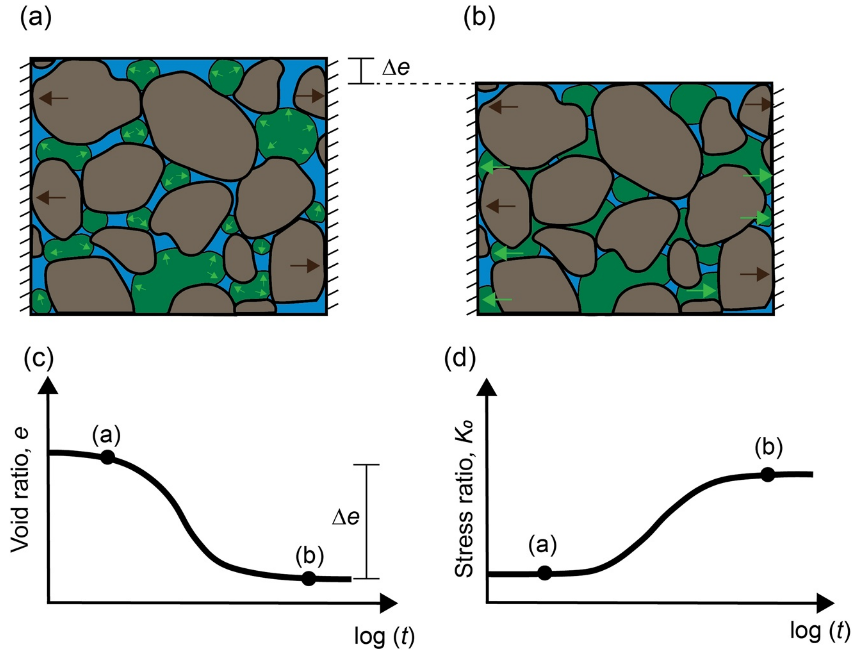

Figure 11. Conceptual model for deformation of hydrate-bearing sandy-silt. (a) Initially, the applied load is supported by both the soil skeleton and the hydrate (small green arrows). (b) With time, the hydrate flow into the space vacated by displacing the pore water and the connected hydrate phase transfers the load laterally (green arrows). (c) Inferred compression and (d) inferred response of K_0 with log time.

This analogy, based on concepts in the ice community (Ladanyi & Morel, 1990), would result in a value of $K_0 = 1$ at high hydrate saturation.

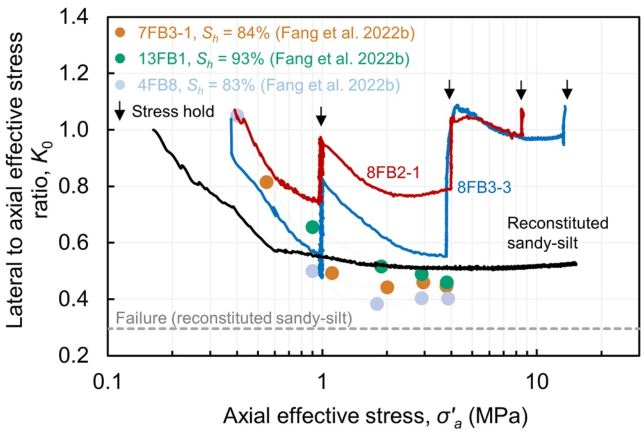

Figure 12. Ratio of lateral to axial effective stress (K_0) as a function of effective stress under uniaxial strain for hydrate-bearing (colored lines and symbols) and non-hydrate-bearing sediments (black line) from GC 955: 8FB3-3, 8FB1-2 (blue and red lines, this study), 7FB3-1, 13FB1, 4FB (filled circles, Fang, Flemings, Germaine, et al., 2022). Fang et al.'s measurements record the lateral stress ratio after incremental loading. Our measurements are made at a constant rate of strain that are interrupted by three stress holds during the tests (black arrows). The reconstituted sandy-silt lithofacies K_0 behavior and shear failure are superimposed.

4.4. Viscoplastic Behavior of Hydrate-Bearing Sediments—Previous Studies

This work further illuminates the time dependent material behavior of hydrate-bearing porous media. This was initially explored by Miyazaki et al. (2007); they showed with triaxial compression tests that deformation rate is proportional to deviatoric stress. Yoneda et al. (2019b, 2022) and Deusner et al. (2019) subsequently documented similar behavior. Isotropic creep tests showed the deformation induced by creep increases with hydrate saturation (Lei et al., 2020). Triaxial tests with deviatoric stress holds indicated the creep rate accelerates near the hydrate phase boundary, either by increasing the temperature or reducing the pressure (Lei & Seol, 2020). Triaxial creep tests depict similar results with an increase in temperature (Li et al., 2019; Zhu et al., 2022). Yoneda et al. (2019a) found opposing behavior on massive natural gas hydrates, where there was no strain-rate dependency for uniaxial compressive strength. Our study is the first work that has described creep and the response of lateral stress under uniaxial strain. We have also begun the challenging task of simulating the behavior observed.

4.5. Experimental Challenges in K_0 Tests—Hydrate-Bearing Sediments

The limited number of K_0 measurements made on hydrate-bearing sediments (natural and artificial) have hinted that hydrate-bearing porous media behave

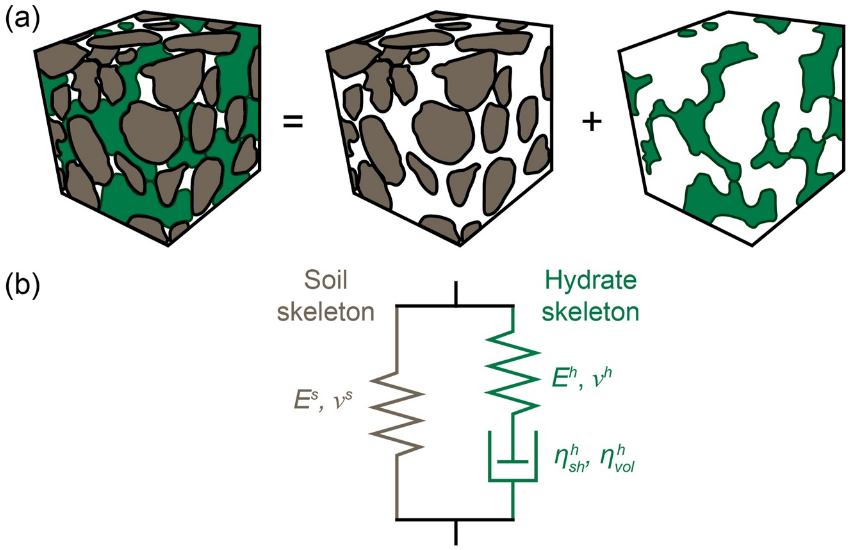

Figure 13. (a) The hydrate-bearing sandy-silts is represented as composite made of the soil and hydrate skeletons. (b) The spring-dashpot model involves an elastic soil (Young modulus E^s; Poisson ratio ν^s) and a Maxwell viscoelastic hydrate skeleton (Young modulus E^h; Poisson ratio ν^h; shear viscosity η^h_{sh}; volumetric viscosity η^h_{vol}).

differently than the porous media alone. However, the challenges of making these measurements may be responsible for some of the contrasting observations in the literature.

Fang, Flemings, Germaine, et al. (2022) used the device shown in this study (K_0-triaxial); however, their protocol to maintain uniaxial strain differed from ours. In Fang, Flemings, Germaine, et al. (2022), the confining chamber is locked; thus, fluid cannot move in our out and forms a nearly incompressible lateral boundary. However, Fang, Flemings, Germaine, et al. (2022) found samples experienced a radial widening of 0.16% during the consolidation process. The apparent K_0 values are highly sensitive to small deviations from uniaxial strain conditions (Roscoe & Burland, 1968). Radial widening implies lower lateral stresses compared to uniaxial strain conditions, which leads to lower apparent K_0 values. In contrast, our method to conduct uniaxial strain compression results in a radial strain of only of 0.005% (Appendix B). We anticipate our method resembles more closely the true uniaxial strain K_0 values.

Yoneda et al. (2022) used a rigid-wall cell. In this case, samples that have a reduced diameter (e.g., core degradation) would radially expand as they come into contact with the rigid ring. Lateral stress estimates are sensitive to this initial radial expansion (Ofer, 1981; Okochi & Tatsuoka, 1984; Roscoe & Burland, 1968). Kim et al. (2021) also used a rigid-wall cell for their synthetic hydrate-bearing sand tests. While in this case, the sample is fully in contact with the rigid wall, the lateral stress interpretation from diaphragm-type transducer must consider the soil to cell stiffness ratio (Clayton & Bica, 1993), stress re-distribution near sensors (Weiler & Kulhawy, 1982), and side-wall friction (Oldecop & Alonso, 2017). These effects can result in lower estimates of lateral stress, and therefore, underpredict K_0 values.

Table 4
Parameters Adopted for the Spring-Dashpot Model

Parameter	Value
Young modulus—sediment, E^s [Pa]	6.3×10^7
Poisson ratio—sediment, ν^s	0.34
Young modulus—hydrate, E^h [Pa]	4×10^7
Poisson ratio—hydrate, ν^h	0.15
Shear viscosity, η_{sh} [Pa.s]	1.2×10^{11}
Volumetric viscosity, η_{vol} [Pa.s]	1×10^{16}
Initial load fraction by the hydrate—CRS compression	0.0
Initial load fraction by the hydrate—stress hold	1.0

4.6. Implication of Viscoplastic Behavior at the Production and Geological Time Scales

Our experimental results show that the presence of hydrate-bearing sandy-silts will undergo creep and relaxation. The significant deformation during the stress holds and the near isotropic stress conditions, are examples of this viscoplastic behavior. Moreover, the time scales for stress relaxation and creep are within 1 day, which suggests that on the time scale of hydrate production (days to months), the viscous nature of the hydrate will impact reservoir geomechanical state.

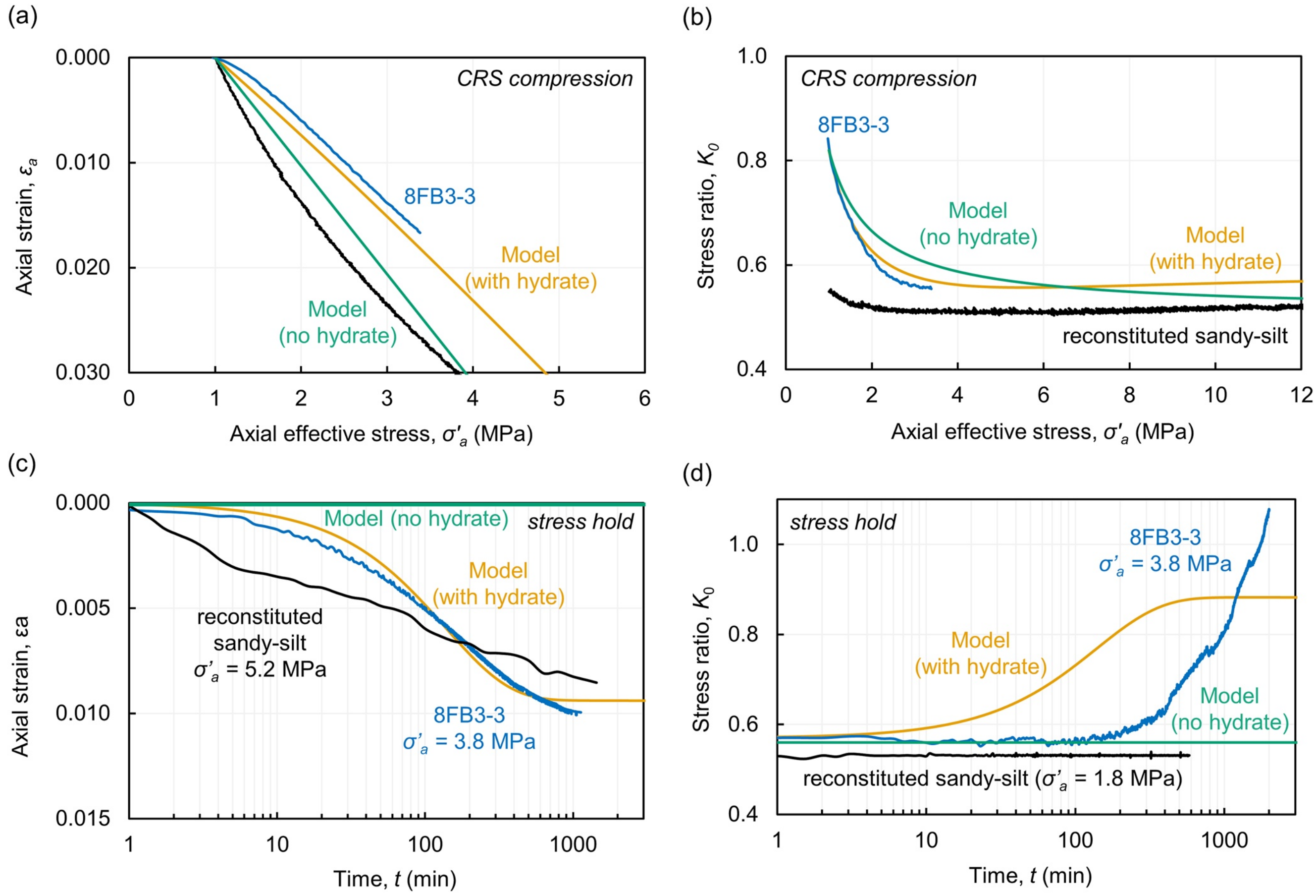

Figure 14. Modeled strain and stress ratio (K_0) using the spring-dashpot model. (a) Axial strain and (b) K_0 response during the second CRS-compression. Reconstituted sandy-silt data is superimposed. (c) Axial strain and (d) K_0 response during the second stress-hold. The reconstituted sandy-silt data for the incremental loading test at $\sigma'_a = 5.2$ MPa and the stress-hold at $\sigma'_a = 1.8$ MPa are superimposed.

Most existing models of hydrate production assume compression depends on effective stresses, material compressibility, hydrate saturation, temperature, and pressure (Kimoto et al., 2010; Sanchez et al., 2018). Only a few models consider time dependency (e.g., Zhou et al., 2022). These effects are important for compaction-driven production; viscous deformation will occur as the pore pressure is reduced. This time-dependent compression will impact the water flow far from the wellbore, which in turn, will affect gas and water flow rates closer to the production zone.

We suggest that hydrate-bearing sandy-silts loaded by burial will relax over geological time-scales; thus, the stress state in these strata will be isotropic and equal to the overburden stress. This situation is also found in salt bodies which also exhibit viscous behavior (Urai & Spiers, 2007; Wawersik & Stone, 1986). A practical consequence is that the least principal stress in the hydrate reservoir will be high and equal to the overburden stress (Figure 15a). This means that the borehole will withstand very high pressures before hydraulic fracturing will occur. An interesting consequence of this is that if a hydrate reservoir is hydraulically fractured, it will be difficult to contain the fractures to the hydrate bearing layer because the least principal stress state in the bounding layers will be lower. Furthermore, because the stresses are isotropic, there will not be a preferred fracture orientation when these strata are hydraulically fractured. In addition, during drilling, if the well is underbalanced, where the borehole fluid pressure is significantly beneath the least principal stress, we would expect hole closure due to viscous flow in the reservoir. This is again observed in salt systems (Dusseault et al., 2004; C. M. Kim, 1988).

Borehole breakouts in hydrate-bearing layers are seldom observed, with only few instances documented in fine-grained sediments that contain hydrate-filled fractures or the bounding strata of such systems (Birchwood &

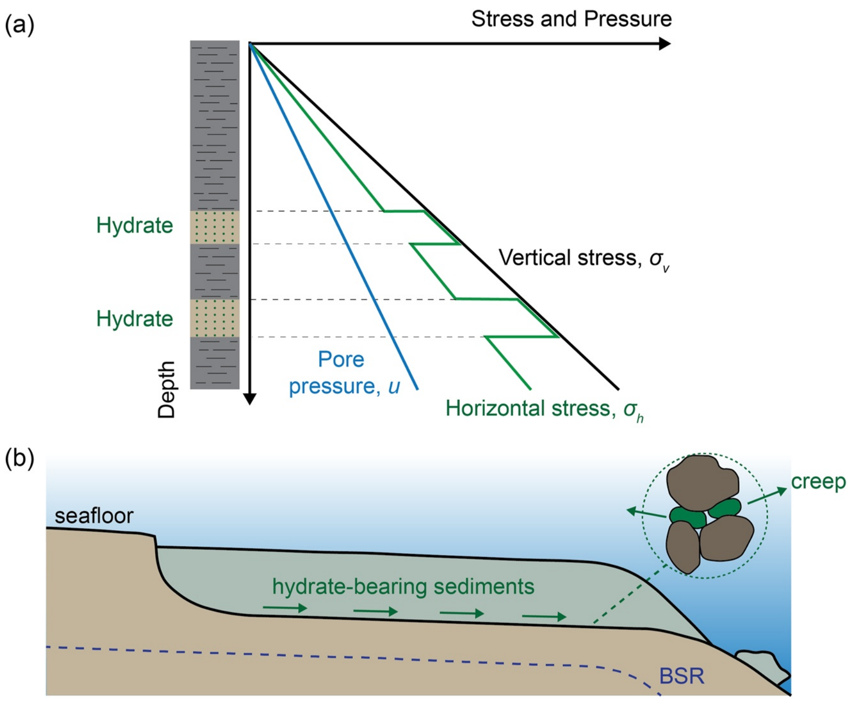

Figure 15. Geological implications of viscoplastic behavior of hydrate-bearing sandy-silts. (a) In-situ stress profile with depth. The least principal horizontal stress is higher in hydrate-bearing layers ($K_0 \approx 1.0$) than in the bounding mudrock ($K_0 \approx 0.45$). (b) Proposed schematic illustration of a hydrate-driven landslide (after Mountjoy et al. (2014)). The viscoplastic hydrate layer facilitates the slow creeping movement. The bottom-simulating reflector (BSR) is parallel to the seafloor.

Noeth, 2012; Cook et al., 2008, 2014). Conversely, stable boreholes have been observed in hydrate-bearing sands, suggesting either an isotropic stress state or a highly competent wellbore.

Several studies have suggested that submarine landslides occur as a slow creeping process (Barnes et al., 2019; Mountjoy et al., 2014). Mountjoy et al. (2014) proposed that the viscoplastic nature of hydrate-bearing sediments enables a glacial-like deformation, similar to water-ice mix rock glaciers (Arenson et al., 2002). Our experimentally observed time-dependent behavior supports this hypothesis, where the presence of hydrate facilitates long-term deformation under sustained load (Figure 15b). Although the mechanisms triggering submarine landslides associated to gas hydrates remain unclear, this is an intriguing proposal.

5. Conclusions

We investigated the geomechanical behavior of natural and intact hydrate-bearing sediments from GC 955 in the deep-water GOM. Our uniaxial strain experiments demonstrate that hydrate-bearing sandy-silts behave viscoplastically.

Under constant strain rate (CRS) uniaxial loading, hydrate-bearing sandy-silts are stiffer than equivalent non-hydrate-bearing sediments. When the axial stress is fixed after CRS-loading, the void ratio in hydrate-bearing sandy-silts decline in a sigmoidal fashion with the log of time. In contrast, the void in non-hydrate-bearing sediments decreases linearly with log of time. The stress ratio K_0, is higher in hydrate bearing sandy-silts than in sediments without hydrate during CRS-loading. During stress holds, K_0 increases toward isotropic stress conditions ($K_0 = 1.0$) within hours.

We interpret that upon loading, the hydrate bears a significant fraction of the applied load. With time, the hydrate flows viscously into the space vacated by the expelled pore water. During this process, the hydrate phase relaxes and redistributes the load, which results in the increase of K_0 toward an isotropic state. Much, but not all of the complex interplay between deformation and viscoplastic deformation is captured by a spring and dashpot model.

Our results hint that hydrate reservoirs that have undergone loading by burial have high horizontal stresses and can experience creep during production time scales. This will impact borehole stability and completion strategies that use hydraulic fracturing. The presence of significant time-dependent deformation over hours in the laboratory also suggests creep may play a role during reservoir depletion, a process not generally included in reservoir simulation models.

Appendix A: Governing Equations for the Standard Linear Solid

The model consists of two systems in parallel (Figure 13b). The elastic soil skeleton (Young modulus E^s; Poisson ratio ν^s) and the viscoelastic element that represents the hydrate (Young modulus E^h; Poisson ratio ν^h; shear viscosity η^h_{sh}; volumetric viscosity η^h_{vol}). This representation assumes the strains in the hydrate and the soil skeleton are the same. For the viscoelastic arm (hydrate), we use the Maxwell representation where the spring and dashpot are in series (i.e., effective stresses in the spring and dashpot are the same for the hydrate viscoelastic arm).

The effective stress σ' is a combination of the effective stress carried by the soil skeleton (σ'_s) and that carried by the hydrate (σ'_h).

$$\sigma' = \sigma'_h + \sigma'_s \tag{A1}$$

The pore pressure acts equally in both the hydrate and the skeleton; therefore, a total stress analysis results in

$$\sigma = \sigma'_h + \sigma'_s + u \tag{A2}$$

The strain rates ($\dot{\varepsilon}$) are the same in the skeleton and the hydrate, $\dot{\varepsilon} = \dot{\varepsilon}_h = \dot{\varepsilon}_s$. We analyze the response in terms of the elastic skeleton strain rate ($\dot{\varepsilon}^e_{\mathrm{s}}$) and hydrate viscoelastic hydrate strain rate ($\dot{\varepsilon}^e_h + \dot{\varepsilon}^v_h$),

$$\dot{\varepsilon}_s = \dot{\varepsilon}^e_{\mathrm{s}} = \frac{1}{9K^s}\, tr\left(\dot{\sigma}'_s\right) I + \frac{1}{2\mu^s}\, \mathrm{dev}\left(\dot{\sigma}'_s\right) \tag{A3}$$

$$\dot{\varepsilon}_h = \dot{\varepsilon}^e_h + \dot{\varepsilon}^v_h = \left(\frac{1}{9K^h}\, tr\left(\dot{\sigma}'_h\right) + \frac{1}{9\eta_{\mathrm{vol}}}\, tr\left(\dot{\sigma}'_h\right)\right) I + \frac{1}{2\mu^h}\, \mathrm{dev}\left(\dot{\sigma}'_h\right) + \frac{1}{2\eta_{sh}}\, \mathrm{dev}\left(\dot{\sigma}'_h\right) \tag{A4}$$

where I is the identity matrix, and *tr* and *dev* are the trace and deviatoric components of the stress tensor, respectively. The elastic constants are: $K = E/(3\,(1-2\nu))$ and $\mu = E\nu/((1+\nu)\,(1-2\nu))$. Since the hydrate and soil skeleton strains are the same, Equations A3 and A4 are equal and simplified for our uniaxial strain representation. The only non-zero strain is in the axial direction (i.e., one-dimensional compression). Equation A1 is also simplified, as there are only two principal stresses, that is, axial and lateral. We solve the set of equations using a forward numerical scheme, where the strain rate $\dot{\varepsilon}$ from the previous iteration is used to estimate the current strain ε.

Appendix B: Validation Using Resedimented Samples (RBBC)

We conducted a validation study to assess the accuracy of our K_0-triaxial measurement system. We prepared Boston Blue Clay (RBBC) specimens using the resedimentation technique (Germaine & Germaine, 2009). RBBC is well-characterized over a wide range of stresses (Adams et al., 2013; Casey et al., 2015; Day-Stirrat et al., 2011). Dry material was mixed with 1.6 wt.% NaCl brine at water content equal twice the liquid limit, $w_L = 47\%$. Mixing for 5 hr was performed to fully disaggregate and mix the sediment suspension. Vacuum for ~8 hr removed any trapped air inside the overnight equilibrated slurry. We incrementally loaded the specimen up to ~0.5 MPa. The specimen is then extruded into a core liner tube, trimmed and placed inside the K_0-triaxial with the core liner.

We conducted two loading cycles under uniaxial strain conditions at a constant rate of strain ~0.7%/hr (Figure B1a). First, we loaded up to ~5 MPa of axial effective stress, held the stress constant for ~16 hr while maintaining uniaxial conditions, and unloaded at the same strain rate. We then reloaded up to ~18 MPa and held the stress constant following the same procedure.

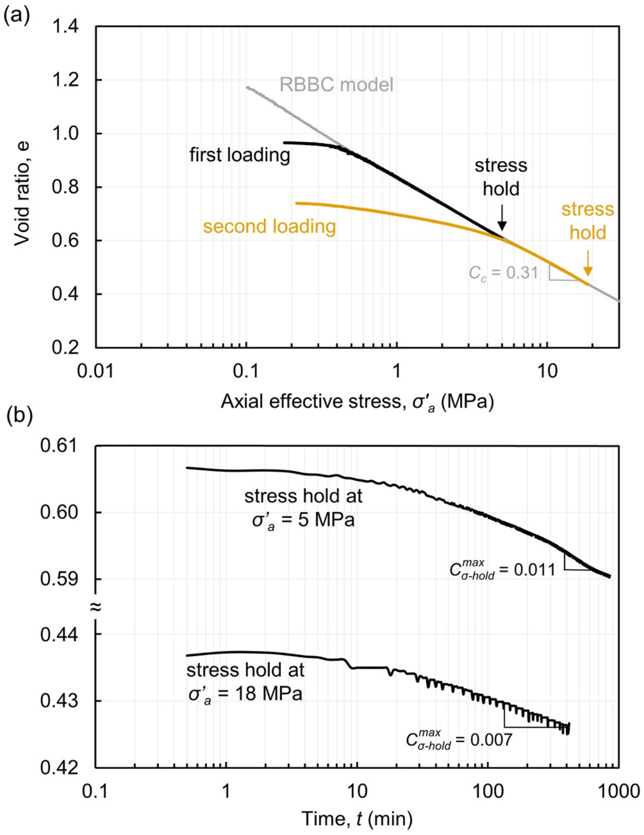

Figure B1. Uniaxial strain compression behavior of resedimented Boston Blue Clay (RBBC). (a) Evolution of void ratio e with increasing axial effective stress. We have omitted unloading and stress hold data for clarity. The RBBC model is derived from multiple tests conducted in this material (Nordquist, 2015). (b) Evolution of void ratio with time during the two stress holds at $\sigma'_a = 5$ and 18 MPa. The initial time corresponds to the start of the stress hold.

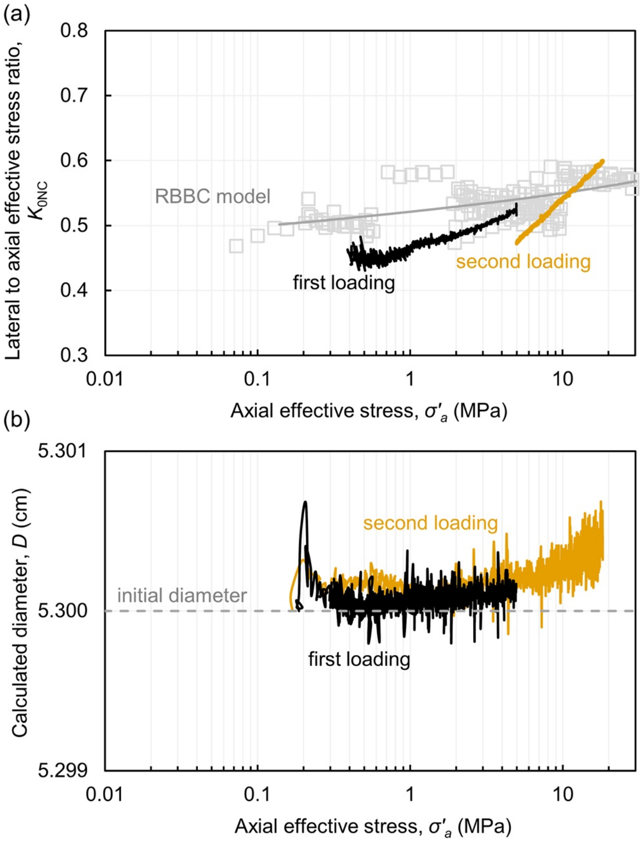

Figure B2. Stress ratio K_{0NC} and inferred diameter evolution with axial effective stress. (a) Results for K_0 ratio gathered with the K_0-triaxial (black and yellow lines) are compared with triaxial cell data (markers). Benchmark data is used to infer the resedimented Boston Blue Clay K_{0NC} model. (b) Calculated diameter using the volume expelled during compression and the axial strain. The radial strain remains less than 5×10^{-5} in both loading cycles.

The compression curves for the two loading cycles have two distinct slopes: an initial flatter part (recompression) until the vertical effective stress exceeds the preconsolidation stress (i.e., 0.5 MPa for the first loading and 5 MPa for the second loading, respectively) followed by a steeper curve (virgin) with slope C_c (compression index).

We compare the compression results obtained from the K_0-triaxial with constant rate of strain (CRS) rigid-wall cells (Figure B1a). The RBBC model is a fitting curve of multiple tests conducted in this material over the last three decades (Nordquist, 2015). Virgin compression trends are in close agreement between the different data sets and the compression index $C_c = 0.31$ is the same for the 0.5–18 MPa axial effective stress range.

Figure B1b shows the void ratio versus time during the two stress holds. The stress-hold compression index ($C_{\sigma\text{-hold}}$) reaches maximum values of $C^{\max}_{\sigma-\text{hold}} = 0.011, 0.007$ for the stress holds at $\sigma'_a = 5$ and 18 MPa respectively (Figure B1b).

The variation of the lateral stress ratio with axial effective stress for RBBC is shown in Figure B2a. Values before the preconsolidation stress are not shown for clarity; therefore, all stress ratio data refers to normally consolidated conditions K_{0NC}. The K_{0NC} slightly increases from 0.46 ($\sigma'_a = 1$ MPa) to 0.52 ($\sigma'_a = 5$ MPa). The second loading starts a lower $K_{0NC} = 0.45$, but shows a more pronounced increase to 0.6 ($\sigma'_a = 18$ MPa).

We compare these K_{0NC} results with benchmark data obtained from triaxial apparatuses (Figure B2a) (see Casey et al. (2015) for the entire data set). These triaxial data correspond to multiple resedimented specimens and were obtained using a similar uniaxial strain protocol to the K_0-triaxial (i.e., axial and volumetric strains are continuously matched). An empirical fit to these data results in the following expression for the relation between void ratio and stress ratio (model in Figure B2a):

$$K_{0\mathrm{NC}} = 0.64 - 0.26\frac{e}{1+e} \tag{B1}$$

Our K_0-triaxial data captures the $K_{0\mathrm{NC}}$ versus σ'_a upward trends. Differences between the model and our data set may be attributed to unaccounted compressibility effects in the K_0-triaxial. We conducted apparatus compressibility tests with a steel sample that confirm this observation.

Figure B2b shows the calculated sample diameter using the pore volume expelled during consolidation (i.e., volumetric strain ε_v) and the axial strain (ε_a). These results indicate a maximum radial strain expansion of $\varepsilon_r \approx 5 \times 10^{-5}$. This calculation assumes the sample has a constant diameter and there is no bulging or diametric contraction.

Nomenclature

A_{sample}	sample cross sectional area, L^2 (m^2)
C	compression index-slope of the e versus $\log(\sigma'_a)$
$C_{\sigma\text{-hold}}$	slope of the e versus $\log(t)$-stress hold
C_α	slope of the e versus $\log(t)$-incremental loading
CRS	constant rate of axial strain
D	sample average diameter, L (m)
D_{50}	mean grain size, L (m)
E	Young modulus, $\mathrm{ML}^{-1}\mathrm{T}^{-2}$ (Pa)
e	void ratio
k	permeability, L^2 (m^2)
K_0	lateral to vertical effective stress ratio under uniaxial strain conditions
$K_{0\mathrm{NC}}$	K_0 under normally consolidated conditions
K_f	lateral to vertical effective stress ratio at failure
L	sample length, L (m)
n	porosity
P	fluid pressure (subindex-C: confining chamber; subindex-S: sample; subindex-P: piston chamber), $\mathrm{ML}^{-1}\mathrm{T}^{-2}$ (Pa)
q	deviatoric stress, $\mathrm{ML}^{-1}\mathrm{T}^{-2}$ (Pa)
u	sample pressure, $\mathrm{ML}^{-1}\mathrm{T}^{-2}$ (Pa)
S_h	hydrate saturation
w_L	liquid limit
w_P	plastic limit
Δe	change in void ratio (subindex-CRS: constant rate of strain; subindex-σ-hold: stress hold)
ΔV	change in sample volume, L^3 (m^3)
ε	strain (subindex-a: axial; subindex-v: volumetric; subindex-l: lateral)
ν	Poisson's ratio
η	viscosity, $\mathrm{ML}^{-1}\mathrm{T}^{-1}$ (Pa.s)
τ_σ	stress relaxation time, T (s)
ρ_g	grain density, ML^{-3} ($\mathrm{g/cm}^3$)
σ	total stress (subindex-a: axial; subindex-l: lateral), $\mathrm{ML}^{-1}\mathrm{T}^{-2}$ (Pa)
σ’	effective stress (subindex-a: axial; subindex-l: lateral), $\mathrm{ML}^{-1}\mathrm{T}^{-2}$ (Pa)
ϕ'	friction angle

Data Availability Statement

Datasets presented as part of this study are available from the Texas Data repository (Cardona et al., 2022).

Acknowledgments

This research was supported by the U.S. Department of Energy under Award DE-FE0023919. Joshua O'Connell and Donnie Brooks provided technical support for pressure core manipulation, cutting, and triaxial cell setup.

References

Abegg, F., Hohnberg, H. J., Pape, T., Bohrmann, G., & Freitag, J. (2008). Development and application of pressure-core-sampling systems for the investigation of gas- and gas-hydrate-bearing sediments. *Deep Sea Research Part I: Oceanographic Research Papers*, *55*(11), 1590–1599. https://doi.org/10.1016/j.dsr.2008.06.006

Adams, A. L., Germaine, J. T., Flemings, P. B., & Day-Stirrat, R. J. (2013). Stress induced permeability anisotropy of resedimented Boston Blue Clay. *Water Resources Research*, *49*(10), 6561–6571. https://doi.org/10.1002/wrcr.20470

Alley, R. B. (1992). Flow-law hypotheses for ice-sheet modeling. *Journal of Glaciology*, *38*(129), 245–256. https://doi.org/10.3189/S0022143000003658

Arenson, L., Hoelzle, M., & Springman, S. (2002). Borehole deformation measurements and internal structure of some rock glaciers in Switzerland. *Permafrost and Periglacial Processes*, *13*(2), 117–135. https://doi.org/10.1002/ppp.414

ASTM. (2012). *ASTM D4186-06: Standard test method for one-dimensional consolidation properties of saturated cohesive soils using controlled-strain loading*. ASTM International. https://doi.org/10.1520/D4186_D4186M-12E01

ASTM. (2016). *ASTM D854-14: Standard test methods for specific gravity of soil solids by water pycnometer*. ASTM International. https://doi.org/10.1520/D0854-14

ASTM. (2018). *ASTM D4318-17e1: Standard test methods for liquid limit, plastic limit, and plasticity index of soils*. ASTM International. https://doi.org/10.1520/D4318-17E01

Barnes, P. M., Pecher, I. A., LeVay, L. J., Bourlange, S. M., Brunet, M. M. Y., Cardona, S., et al. (2019). Proceedings of the International Ocean Discovery Program, 372A. In I. A. Pecher, P. M. Barnes, & L. J. LeVay (Eds.), *Creeping gas hydrate slides*. International Ocean Discovery Program. https://doi.org/10.14379/iodp.proc.372A.101.2019

Birchwood, R., & Noeth, S. (2012). Horizontal stress contrast in the shallow marine sediments of the Gulf of Mexico sites Walker Ridge 313 and Atwater Valley 13 and 14 – Geological observations, effects on wellbore stability, and implications for drilling. *Marine and Petroleum Geology*, *34*(1), 186–208. https://doi.org/10.1016/j.marpetgeo.2012.01.008

Boswell, R., & Collett, T. S. (2011). Current perspectives on gas hydrate resources. *Energy and Environmental Science*, *4*(4), 1206–1215. https://doi.org/10.1039/C0EE00203H

Boswell, R., Frye, M., Shelander, D., Shedd, W., McConnell, D. R., & Cook, A. (2012). Architecture of gas-hydrate-bearing sands from Walker Ridge 313, Green Canyon 955, and Alaminos Canyon 21: Northern deepwater Gulf of Mexico. *Marine and Petroleum Geology*, *34*(1), 134–149. https://doi.org/10.1016/j.marpetgeo.2011.08.010

Brooker, E. W., & Ireland, H. O. (1965). Earth pressures at rest related to stress history. *Canadian Geotechnical Journal*, *2*(1), 1–15. https://doi.org/10.1139/t65-001

Cardona, A., Bhandari, A. R., Heidari, M., & Flemings, P. B. (2022). *Data for "The viscoplastic behavior of natural hydrate-bearing sediments under uniaxial strain compression (K0 loading)*. Texas Data Repository. https://doi.org/10.18738/T8/T0FHHR

Casey, B., Germaine, J. T., Flemings, P. B., & Fahy, B. P. (2015). Estimating horizontal stresses for mudrocks under one-dimensional compression. *Marine and Petroleum Geology*, *65*, 178–186. https://doi.org/10.1016/j.marpetgeo.2015.02.001

Casey, B., Germaine, J. T., Flemings, P. B., & Fahy, B. P. (2016). In situ stress state and strength in mudrocks. *Journal of Geophysical Research: Solid Earth*, *121*(8), 5611–5623. https://doi.org/10.1002/2016jb012855

Clayton, C. R. I., & Bica, A. V. D. (1993). The design of diaphragm-type boundary total stress cells. *Géotechnique*, *43*(4), 523–535. https://doi.org/10.1680/geot.1993.43.4.523

Collett, T. S. (2002). Energy resource potential of natural gas hydrates. *AAPG Bulletin*, *86*(11), 1971–1992. https://doi.org/10.1306/61EEDDD2-173E-11D7-8645000102C1865D

Cook, A. E., Goldberg, D., & Kleinberg, R. L. (2008). Fracture-controlled gas hydrate systems in the northern Gulf of Mexico. *Marine and Petroleum Geology*, *25*(9), 932–941. https://doi.org/10.1016/j.marpetgeo.2008.01.013

Cook, A. E., Goldberg, D. S., & Malinverno, A. (2014). Natural gas hydrates occupying fractures: A focus on non-vent sites on the Indian continental margin and the northern Gulf of Mexico. *Marine and Petroleum Geology*, *58*, 278–291. https://doi.org/10.1016/j.marpetgeo.2014.04.013

Craig, R. F. (2005). *Soil mechanics* (7th ed.). Spon Press.

Day-Stirrat, R. J., Schleicher, A. M., Schneider, J., Flemings, P. B., Germaine, J. T., & van der Pluijm, B. A. (2011). Preferred orientation of phyllosilicates: Effects of composition and stress on resedimented mudstone microfabrics. *Journal of Structural Geology*, *33*(9), 1347–1358. https://doi.org/10.1016/j.jsg.2011.06.007

Deusner, C., Gupta, S., Xie, X.-G., Leung, Y. F., Uchida, S., Kossel, E., & Haeckel, M. (2019). Strain rate-dependent hardening-softening characteristics of Gas hydrate-bearing sediments. *Geochemistry, Geophysics, Geosystems*, *20*(11), 4885–4905. https://doi.org/10.1029/2019GC008458

Dickens, G. R., Castillo, M. M., & Walker, J. C. G. (1997). A blast of gas in the latest Paleocene: Simulating first-order effects of massive dissociation of oceanic methane hydrate. *Geology*, *25*(3), 259–262. https://doi.org/10.1130/0091-7613(1997)025<0259:ABOGIT>2.3.CO;2

Durham, W. B., Kirby, S. H., Stern, L. A., & Zhang, W. (2003). The strength and rheology of methane clathrate hydrate. *Journal of Geophysical Research*, *108*(B4). https://doi.org/10.1029/2002jb001872

Dusseault, M. B., Maury, V., & Santarelli, F. J. (2004). Drilling through salt: Constitutive behavior and drilling strategies. Paper presented at the Gulf Rocks 2004, the 6th North America Rock Mechanics Symposium (NARMS).

Fang, Y., Flemings, P. B., Daigle, H., Phillips, S. C., Meazell, P. K., & You, K. (2020). Petrophysical properties of the Green Canyon Block 955 hydrate reservoir inferred from reconstituted sediments: Implications for hydrate formation and production. *AAPG Bulletin*, *104*(9), 1997–2028. https://doi.org/10.1306/01062019165

Fang, Y., Flemings, P. B., Daigle, H., Phillips, S. C., & O'Connell, J. (2022). Permeability of methane hydrate-bearing sandy silts in the deep-water Gulf of Mexico (Green Canyon Block 955). *AAPG Bulletin*, *106*(5), 1071–1100. https://doi.org/10.1306/08102121001

Fang, Y., Flemings, P. B., Germaine, J. T., Daigle, H., Phillips, S. C., & O'Connell, J. (2022). Compression behavior of hydrate-bearing sediments. *AAPG Bulletin*, *106*(5), 1101–1126. https://doi.org/10.1306/01132221002

Feda, J. (1984). K0-coefficient of sand in triaxial apparatus. *Journal of Geotechnical Engineering*, *110*(4), 519–524. https://doi.org/10.1061/(ASCE)0733-9410(1984)110:4(519)

Findley, W. N., Lai, J. S., & Onaran, K. (1976). *Creep and relaxation of nonlinear viscoelastic materials with an introduction to linear viscoelasticity*. North Holland.

Flemings, P. B. (2021). *A concise guide to geopressure: Origin, prediction, and applications*. Cambridge Press. https://doi.org/10.1017/9781107326309

Flemings, P. B., Cook, A. E., Collett, T., & Boswell, R. (2022). Gas hydrates in Green Canyon Block 955, deep-water Gulf of Mexico: Part II, insights and future challenges. *AAPG Bulletin*, *106*(5), 937–947. https://doi.org/10.1306/bltnintro030922

Flemings, P. B., Phillips, S. C., Boswell, R., Collett, T. S., Cook, A. E., Dong, T., et al. (2020). Pressure coring a Gulf of Mexico deep-water turbidite gas hydrate reservoir: Initial results from the University of Texas–Gulf of Mexico 2-1 (UT-GOM2-1) hydrate pressure coring Expedition. *AAPG Bulletin*, *104*(9), 1847–1876. https://doi.org/10.1306/05212019052

Germaine, J. T., & Germaine, A. V. (2009). *Geotechnical laboratory measurements for engineers*. John Wiley. https://doi.org/10.1002/9780470548790

Ginsburg, G., Soloviev, T., Matveeva, T., & Andreeva, T. (2000). Sediment grain size control on gas hydrate presence, Sites 994, 995, and 997. *Proceedings of the Ocean Drilling Program*, *164*, 237–245. https://doi.org/10.2973/odp.proc.sr.164.236.2000

Hagin, P. N., & Zoback, M. D. (2004). Viscous deformation of unconsolidated reservoir sands—Part 2: Linear viscoelastic models. *Geophysics*, *69*(3), 742–751. https://doi.org/10.1190/1.1759460

Hirth, G., Teyssier, C., & Dunlap, J. W. (2001). An evaluation of quartzite flow laws based on comparisons between experimentally and naturally deformed rocks. *International Journal of Earth Sciences*, *90*(1), 77–87. https://doi.org/10.1007/s005310000152

Hyodo, M., Li, Y., Yoneda, J., Nakata, Y., Yoshimoto, N., & Nishimura, A. (2014). Effects of dissociation on the shear strength and deformation behavior of methane hydrate-bearing sediments. *Marine and Petroleum Geology*, *51*, 52–62. https://doi.org/10.1016/j.marpetgeo.2013.11.015

Jaky, J. (1944). The coefficient of Earth pressure at Rest. *Journal of the Society of Hungarian Architects and Engineers*, 355–358.

Jin, Y., Konno, Y., & Nagao, J. (2014). Pressurized subsampling system for pressured gas-hydrate-bearing sediment: Microscale imaging using X-ray computed tomography. *Review of Scientific Instruments*, *85*(9), 094502. https://doi.org/10.1063/1.4896354

Kim, C. M. (1988). Field measurement of borehole closure across salt formation: Implementation to well cementing. P*aper presented at the 63rd SPE Annual Technical Conference and Exhibition*. https://doi.org/10.2118/18030-MS

Kim, J., Seol, Y., & Dai, S. (2021). The coefficient of Earth pressure at rest in hydrate-bearing sediments. *Acta Geotechnica*, *16*(9), 2729–2739. https://doi.org/10.1007/s11440-021-01174-0

Kimoto, S., Oka, F., & Fushita, T. (2010). A chemo–thermo–mechanically coupled analysis of ground deformation induced by gas hydrate dissociation. *International Journal of Mechanical Sciences*, *52*(2), 365–376. https://doi.org/10.1016/j.ijmecsci.2009.10.008

Ladanyi, B., & Morel, J.-F. (1990). Effect of internal confinement on compression strength of frozen sand. *Canadian Geotechnical Journal*, *27*(1), 8–18. https://doi.org/10.1139/t90-002

Lambe, T. W., & Whitman, R. V. (1969). *Soil mechanics*. John Wiley.

Lee, J. Y., Yun, T. S., Santamarina, J. C., & Ruppel, C. (2007). Observations related to tetrahydrofuran and methane hydrates for laboratory studies of hydrate-bearing sediments. *Geochemistry, Geophysics, Geosystems*, *8*(6), Q06003. https://doi.org/10.1029/2006GC001531

Lei, L., Gai, X., & Seol, Y. (2020). Load-bearing characteristic of methane hydrate within coarse-grained sediments – Insights from isotropic consolidation. *Marine and Petroleum Geology*, *121*, 104571. https://doi.org/10.1016/j.marpetgeo.2020.104571

Lei, L., & Seol, Y. (2020). Pore-scale investigation of methane hydrate-bearing sediments under triaxial condition. *Geophysical Research Letters*, *47*(5), e2019GL086448. https://doi.org/10.1029/2019GL086448

Li, Y., Wu, P., Sun, X., Liu, W., Song, Y., & Zhao, J. (2019). Creep behaviors of methane hydrate-bearing frozen sediments. *Energies*, *12*(2), 251. https://doi.org/10.3390/en12020251

Mavko, G., Mukerji, T., & Dvorkin, J. (2009). *The rock physics handbook*. Cambridge University Press. https://doi.org/10.1017/CBO9780511626753

Mayne, P., & Kulhawy, F. H. (1982). K0 - OCR Relationships in soil. *Journal of the Geotechnical Engineering Division*, *108*(6), 851–872. https://doi.org/10.1061/AJGEB6.0001306

Meazell, K., Flemings, P. B., Santra, M., & Johnson, J. E. (2020). Sedimentology and stratigraphy of a deep-water gas hydrate reservoir in the northern Gulf of Mexico. *AAPG Bulletin*, *104*(9), 1945–1969. https://doi.org/10.1306/05212019027

Mesri, G., & Castro, A. (1987). Cα/Cc concept and K0 during secondary compression. *Journal of Geotechnical Engineering*, *113*(3), 230–247. https://doi.org/10.1061/(asce)0733-9410(1987)113:3(230)

Mesri, G., & Godlewski, P. M. (1977). Time- and stress-compressibility interrelationship. *Journal of the Geotechnical Engineering Division*, *103*(5), 417–430. https://doi.org/10.1061/AJGEB6.0000421

Mesri, G., & Hayat, T. M. (1993). The coefficient of Earth pressure at rest. *Canadian Geotechnical Journal*, *30*(4), 647–666. https://doi.org/10.1139/t93-056

Michalowski, R. L. (2005). Coefficient of Earth pressure at rest. *Journal of Geotechnical and Geoenvironmental Engineering*, *131*(11), 1429–1433. https://doi.org/10.1061/(ASCE)1090-0241(2005)131:11(1429)

Milkov, A. V. (2004). Global estimates of hydrate-bound gas in marine sediments: How much is really out there? *Earth-Science Reviews*, *66*(3–4), 183–197. https://doi.org/10.1016/j.earscirev.2003.11.002

Miyazaki, K., Masui, A., Sakamoto, Y., Haneda, H., Ogata, Y., Aoki, K., et al. (2007). Strain rate dependency of sediment containing synthetic methane hydrate in triaxial compression test. *MMIJ*, *123*(11), 537–544. https://doi.org/10.2473/journalofmmij.123.537

Moridis, G., Collett, T., Pooladi-Darvish, M., Hancock, S. H., Santamarina, J. C., Boswell, R., et al. (2011). Challenges, uncertainties, and issues facing Gas production from Gas-hydrate deposits. *SPE Reservoir Evaluation and Engineering*, *14*(01), 76–112. https://doi.org/10.2118/131792-pa

Mountjoy, J. J., Pecher, I., Henrys, S., Crutchley, G., Barnes, P. M., & Plaza-Faverola, A. (2014). Shallow methane hydrate system controls ongoing, downslope sediment transport in a low-velocity active submarine landslide complex, Hikurangi Margin, New Zealand. *Geochemistry, Geophysics, Geosystems*, *15*(11), 4137–4156. https://doi.org/10.1002/2014GC005379

Murray, D. R., Kleinberg, R. L., Sinha, B. K., Fukuhara, M., Osawa, O., Endo, T., & Namikawa, T. (2006). Saturation, acoustic properties, growth habit, and state of stress of a gas hydrate reservoir from well logs. *Petrophysics*, *47*(2), 129–137.

Nordquist, T. J. (2015). *Permeability anisotropy of resedimented mudrocks*. Master's thesis. Massachusetts Institute of Technology. Retrieved from https://dspace.mit.edu/handle/1721.1/99578

Ofer, Z. (1981). Laboratory instrument for measuring lateral soil pressure and swelling pressure. *Geotechnical Testing Journal*, *4*(4), 177–182. https://doi.org/10.1520/GTJ10787J

Okochi, Y., & Tatsuoka, F. (1984). Some factors affecting K0-values of sand measured in triaxial cell. *Soils and Foundations*, *24*(3), 52–68. https://doi.org/10.3208/sandf1972.24.3_52

Oldecop, L. A., & Alonso, E. E. (2017). Measurement of lateral stress and friction in rockfill oedometer tests enabling the analysis of the experimental Results in the p′-q space. *Geotechnical Testing Journal*, *40*(5), 822–832. https://doi.org/10.1520/GTJ20160038

Pestana, J. M., & Whittle, A. J. (1995). Compression model for cohesionless soils. *Géotechnique*, *45*(4), 611–631. https://doi.org/10.1680/geot.1995.45.4.611

Phillips, S. C., Flemings, P. B., Holland, M. E., Schultheiss, P., Waite, W. F., Jang, J., et al. (2020). High concentration methane hydrate in a silt reservoir from the deep-water Gulf of Mexico. *AAPG Bulletin*, *104*(9), 1971–1995. https://doi.org/10.1306/01062018280

Phillips, S. C., Flemings, P. B., You, K., & Waite, W. F. (2022). Thermodynamic insights into the production of methane hydrate reservoirs from depressurization of pressure cores. *AAPG Bulletin*, *106*(5), 1025–1049. https://doi.org/10.1306/08182120216

Poirier, J. P. (1985). *Creep of crystals: High-temperature deformation processes in metals, ceramics and minerals*. Cambridge University Press. https://doi.org/10.1017/CBO9780511564451

Priest, J. A., Druce, M., Roberts, J., Schultheiss, P., Nakatsuka, Y., & Suzuki, K. (2015). PCATS triaxial: A new geotechnical apparatus for characterizing pressure cores from the Nankai Trough, Japan. *Marine and Petroleum Geology*, *66*, 460–470. https://doi.org/10.1016/j.marpetgeo.2014.12.005

Roscoe, K. H., & Burland, J. B. (1968). On the generalized stress-strain behaviour of "wet" clay. In J. Heyman & F. A. Leckie (Eds.), *Engineering plasticity* (pp. 535–609). Cambridge University Press.

Ruppel, C. D., & Kessler, J. D. (2017). The interaction of climate change and methane hydrates. *Reviews of Geophysics*, *55*(1), 126–168. https://doi.org/10.1002/2016RG000534

Rutqvist, J., Moridis, G. J., Grover, T., & Collett, T. (2009). Geomechanical response of permafrost-associated hydrate deposits to depressurization-induced gas production. *Journal of Petroleum Science and Engineering*, *67*(1), 1–12. https://doi.org/10.1016/j.petrol.2009.02.013

Sanchez, M., Santamarina, J. C., Teymouri, M., & Gai, X. (2018). Coupled numerical modeling of Gas hydrate-bearing sediments: From laboratory to field-scale analyses. *Journal of Geophysical Research: Solid Earth*, *123*(12), 10326–10348. https://doi.org/10.1029/2018JB015966

Santamarina, J. C., Dai, S., Jang, J., & Terzariol, M. (2012). Pressure core characterization tools for hydrate-bearing sediment. *Scientific Drilling*, *14*, 44–48. https://doi.org/10.2204/iodp.sd.14.06.2012

Santamarina, J. C., Dai, S., Terzariol, M., Jang, J., Waite, W. F., Winters, W. J., et al. (2015). Hydro-bio-geomechanical properties of hydrate-bearing sediments from Nankai Trough. *Marine and Petroleum Geology*, *66*, 434–450. https://doi.org/10.1016/j.marpetgeo.2015.02.033

Santra, M., Flemings, P. B., Meazell, K., & Scott, E. (2020). Evolution of gas hydrate–bearing deep-water channel-levee system in abyssal Gulf of Mexico: Levee growth and deformation. *AAPG Bulletin*, *104*(9), 1921–1944. https://doi.org/10.1306/04251918177

Schultheiss, P., Francis, T. J. G., Holland, M., Roberts, J. A., Amann, H., Thjunjoto, et al. (2006). Pressure coring, logging and subsampling with the HYACINTH system. In *New techniques in sediment core analysis* (Vol. 267). Geological Society of London. https://doi.org/10.1144/gsl.Sp.2006.267.01.11

Schultheiss, P., Holland, M., & Humphrey, G. (2009). Wireline coring and analysis under pressure: Recent use and future Developments of the HYACINTH system. *Scientific Drilling*, *7*(7), 44–50. https://doi.org/10.5194/sd-7-44-2009

Seol, Y., Lei, L., Jarvis, K., Hill, D., Choi, J. H., Park, T., et al. (2021). Tools for pressure core sub-coring and pore-scale micro-CT (computed tomography) scans. *Scientific Drilling*, *29*, 59–67. https://doi.org/10.5194/sd-29-59-2021

Shin, H., & Santamarina, J. C. (2017). Sediment–well interaction during depressurization. *Acta Geotechnica*, *12*(4), 883–895. https://doi.org/10.1007/s11440-016-0493-1

Sloan, E. D., & Koh, C. (2007). *Clathrate Hydrates of Natural Gases* (3rd ed.). CRC Press.

Sultan, N., Cochonat, P., Foucher, J. P., & Mienert, J. (2004). Effect of gas hydrates melting on seafloor slope instability. *Marine Geology*, *213*(1–4), 379–401. https://doi.org/10.1016/j.margeo.2004.10.015

Urai, J. L., & Spiers, C. J. (2007). The effect of grain boundary water on deformation mechanisms and rheology of rocksalt during long-term deformation. In *Paper presented at the 6th Conference on the Mechanical Behavior of Salt, 'SaltMech6', Hannover, Germany*.

Waite, W. F., Santamarina, J. C., Cortes, D. D., Dugan, B., Espinoza, D. N., Germaine, J., et al. (2009). Physical properties of hydrate-bearing sediments. *Reviews of Geophysics*, *47*(4), RG4003. https://doi.org/10.1029/2008rg000279

Wawersik, W. R., & Stone, C. M. (1986). Experience with hydraulic fracturing tests for stress measurements in the WIPP. *Paper presented at the 27th U.S. Symposium on Rock Mechanics (USRMS), Tuscaloosa, AL.*

Weiler, W. A., & Kulhawy, F. H. (1982). Factors affecting stress cell measurements in soil. *Journal of the Geotechnical Engineering Division*, *108*(12), 1529–1548. https://doi.org/10.1061/AJGEB6.0001393

Wu, P., Li, Y., Liu, W., Sun, X., Kong, X., & Song, Y. (2020). Cementation failure behavior of consolidated gas hydrate-bearing sand. *Journal of Geophysical Research: Solid Earth*, *125*(1), e2019JB018623. https://doi.org/10.1029/2019JB018623

Yoneda, J., Jin, Y., Muraoka, M., Oshima, M., Suzuki, K., Waite, W. F., & Flemings, P. B. (2022). Comprehensive pressure core analysis for hydrate-bearing sediments from Gulf of Mexico Green Canyon Block 955, including assessments of geomechanical viscous behavior and nuclear magnetic resonance permeability. *AAPG Bulletin*, *106*(5), 1143–1177. https://doi.org/10.1306/04272120204

Yoneda, J., Kida, M., Konno, Y., Jin, Y., Morita, S., & Tenma, N. (2019a). In situ mechanical properties of shallow Gas hydrate deposits in the deep seabed. *Geophysical Research Letters*, *46*(24), 14459–14468. https://doi.org/10.1029/2019GL084668

Yoneda, J., Masui, A., Tenma, N., & Nagao, J. (2013). Triaxial testing system for pressure core analysis using image processing technique. *Review of Scientific Instruments*, *84*(11), 114503. https://doi.org/10.1063/1.4831799

Yoneda, J., Oshima, M., Kida, M., Kato, A., Konno, Y., Jin, Y., et al. (2019b). Pressure core based onshore laboratory analysis on mechanical properties of hydrate-bearing sediments recovered during India's National Gas Hydrate Program Expedition (NGHP) 02. *Marine and Petroleum Geology*, *108*, 482–501. https://doi.org/10.1016/j.marpetgeo.2018.09.005

Yoneda, J., Oshima, M., Kida, M., Kato, A., Konno, Y., Jin, Y., & Tenma, N. (2019c). Consolidation and hardening behavior of hydrate-bearing pressure-core sediments recovered from the Krishna–Godavari Basin, offshore India. *Marine and Petroleum Geology*, *108*, 512–523. https://doi.org/10.1016/j.marpetgeo.2018.09.021

You, K., Flemings, P. B., Malinverno, A., Collett, T. S., & Darnell, K. (2019). Mechanisms of methane hydrate formation in Geological systems. *Reviews of Geophysics*, *0*(ja), 1146–1196. https://doi.org/10.1029/2018rg000638

Yun, T. S., Narsilio, G. A., Santamarina, J. C., & Ruppel, C. D. (2006). Instrumented pressure testing chamber for characterizing sediment cores recovered at in situ hydrostatic pressure. *Marine Geology*, *229*(3), 285–293. https://doi.org/10.1016/j.margeo.2006.03.012

Zhou, B., Sanchez, M., Oldecop, L., & Santamarina, J. C. (2022). A Geomechanical model for Gas hydrate bearing sediments Incorporating high Dilatancy, temperature, and Rate effects. *Energies*, *15*(12), 4280. https://doi.org/10.3390/en15124280

Zhu, Y., Chen, C., Luo, T., Song, Y., & Li, Y. (2022). Creep behaviours of methane hydrate-bearing sediments. *Environmental Geotechnics*, *9*(4), 199–209. https://doi.org/10.1680/jenge.18.00196

Rock Mechanics and Rock Engineering (2021) 54:5827–5844
https://doi.org/10.1007/s00603-021-02565-1

ORIGINAL PAPER

Natural Rock Fractures: From Aperture to Fluid Flow

Alejandro Cardona[1,2] · **Thomas Finkbeiner**[1] · **J. Carlos Santamarina**[1]

Received: 20 October 2020 / Accepted: 26 June 2021 / Published online: 7 August 2021

Abstract

Fractures provide preferential flow paths and establish the internal "plumbing" of the rock mass. Fracture surface roughness and the matedness between surfaces combine to delineate the fracture geometric aperture. New and published measurements show the inherent relation between roughness wavelength and amplitude. In fact, data cluster along a power trend consistent with fractal topography. Synthetic fractal surfaces created using this power law, kinematic constraints and contact mechanics are used to explore the evolution of aperture size distribution during normal loading and shear displacement. Results show that increments in normal stress shift the Gaussian aperture size distribution toward smaller apertures. On the other hand, shear displacements do not affect the aperture size distribution of unmated fractures; however, the aperture mean and standard deviation increase with shear displacement in initially mated fractures. We demonstrate that the cubic law is locally valid when fracture roughness follows the observed power law and allows for efficient numerical analyses of transmissivity. Simulations show that flow trajectories redistribute and flow channeling becomes more pronounced with increasing normal stress. Shear displacement induces early aperture anisotropy in initially mated fractures as contact points detach transversely to the shear direction; however, anisotropy decreases as fractures become unmated after large shear displacements. Radial transmissivity measurements obtained using a torsional ring shear device and data gathered from the literature support the development of robust phenomenological models that satisfy asymptotic trends. A power function accurately captures the evolution of transmissivity with normal stress, while a logistic function represents changes with shear displacement. A complementary hydro-chemo-mechanical study shows that positive feedback during reactive fluid flow heightens channeling.

Keywords Fractures · Flow · Roughness · Shear · Stress · Aperture · Rock · Transmissivity

List of symbols

$A_c(\sigma)$ (m^2)	True fracture contact area
A_f (m^2)	Apparent fracture area
A_H	Fitting parameter in Lomize's hydraulic aperture model
A_s	Fitting parameter in Tezuka's fracture transmissivity—shear displacement model
B_H	Fitting parameter in Partir and Cheng's hydraulic aperture model
B_s (MPa)	Fitting parameter in Tezuka's fracture transmissivity—shear displacement model
C_H	Fitting parameter in Partir and Cheng's hydraulic aperture model
c	Ratio true contact area to fracture apparent area
c_f (m/N)	Gouge production coefficient
C_p (m^{-1})	Roughness peak curvature
f_0	Fitting parameter in Plesha's dilation model
G (m^3)	Power spectral density
h_G (m)	Geometric aperture
h_H (m)	Hydraulic aperture
h_{H0} (m)	Hydraulic aperture at zero normal stress
JRC$_{\mathrm{mob}}$	Equivalent joint roughness coefficient for shear
K	Roughness kurtosis
k (s^{-1})	Kinetic rate

✉ Alejandro Cardona
alejandro.cardonaramirez@kaust.edu.sa

Thomas Finkbeiner
thomas.finkbeiner@kaust.edu.sa

J. Carlos Santamarina
carlos.santamarina@kaust.edu.sa

[1] Energy Resources and Petroleum Engineering, King Abdullah University of Science and Technology KAUST, Thuwal 23955-6900, Saudi Arabia

[2] Present Address: Institute for Geophysics, Jackson School of Geosciences, The University of Texas at Austin, Austin, TX, USA

m	Roughness mean slope
N	Number of digital values in a signal
P (MPa)	Fluid pressure
R_a (m)	Average roughness
RMS (m)	Roughness root mean square
$s(\tau)$	Semivariogram
s_G (m)	Standard deviation of the geometric aperture
S_k	Roughness skewness
T (cm^2/s)	Fracture transmissivity
T_c (cm^2/s)	Characteristic fracture transmissivity
$T_{\sigma 0}$ (cm^2/s)	Transmissivity asymptote as $\sigma' \rightarrow 0$
$T_{\sigma\infty}$ (cm^2/s)	Transmissivity asymptote as $\sigma' \rightarrow \infty$
$T_{\delta 0}$ (cm^2/s)	Transmissivity asymptote as $\delta_s \rightarrow 0$
$T_{\delta\infty}$ (cm^2/s)	Transmissivity asymptote as $\delta_s \rightarrow \infty$
W_p (N.m/m^2)	Plastic shear work
$X(\lambda)$ (m)	Asperity amplitude for a given wavelength
z_i (m)	Asperity height
α (m^3)	Spectral density at $\lambda = 1$ m
β	Power spectral density sensitivity to wavelength
δ_n (mm)	Fracture normal displacement
δ_s (mm)	Fracture shear displacement
δ_{sc} (mm)	Characteristic shear displacement
Δx (m)	Sampling interval
$\phi(\lambda)$	Asperity phase
γ	Fracture sensitivity to effective normal stress
η	Fracture sensitivity to shear displacement
λ (m)	Asperity wavelength
μ (Pa s)	Fluid viscosity
μ_G (m)	Mean of the geometric aperture
θ	Fourier transform of the aperture correlation function
ρ (kg/m^3)	Fluid density
σ (MPa)	Normal stress
σ' (MPa)	Effective normal stress
σ_{yield} (MPa)	Yield stress of the material
σ_c (MPa)	Characteristic normal stress
τ	Discrete correlation distance
ζ	Fitting parameter in Swan's fracture transmissivity—normal stress model

1 Introduction

Fractures provide preferential flow paths that define the rock mass internal "plumbing", especially in low matrix-permeability rocks. Therefore, the rock mass hydraulic response results from the fracture density, orientation, and the stress-sensitive fracture transmissivity (Barton et al. 1995; Zimmerman and Bodvarsson 1996). In turn, fluid conduction in fractured rock masses affects the pore pressure distribution and effective stress field, flow rates, and immiscible fluid invasion (Aydin 2000; Shin and Santamarina 2019). Consequently, fracture transmissivity is critical to the engineering design of geotechnical structures, resource recovery, contaminant transport, and the geological storage of nuclear waste or CO$_2$.

The void space between two rough fracture surfaces governs fracture transmissivity (Hakami and Larsson 1996; Olsson and Barton 2001), controls the fracture deformation during normal loading (Tsang and Witherspoon 1981; Brown and Scholz 1986), and determines fracture dilation during shear displacement (Patton 1966; Saeb and Amadei 1992; Lee and Cho 2002).

This study explores the effects of surface roughness on geometric aperture and hydraulic transmissivity as a function of normal stress and shear displacement. The manuscript is organized into three complementary sections: geometric aperture, contact mechanics, and flow. Each section includes an overview of previous research, provides new laboratory data, and advances analyses toward the enhanced understanding and modeling of fracture transmissivity. Altogether, the different sections provide new physical insight into fracture transmissivity and the effects of normal stress and shear displacement. The concise presentation is complemented by seminal references for further details.

2 Geometric Aperture: Fracture Roughness and Matedness

Rock characteristics and fracture genesis define surface roughness and the matedness or geometric correlation between fracture surfaces. For example, fresh tensile fractures exhibit higher degrees of matedness than shear fractures (Odling 1994; Al-Fahmi et al. 2018). Either cross-grain or inter-granular fracture propagation and frictional wear dominate roughness at the sub-meter scale, while kinematics, fracture convergence and the coalescence of secondary fractures control roughness at larger scales (Lee and Bruhn 1996; Candela et al. 2012; Brodsky et al. 2016). Furthermore, post-genesis stress changes and associated displacements, asperity crushing, cataclasis, creep and ploughing, fines generation, chemical dissolution and precipitation alter the void space and lead to complex hydro-thermo-chemo-mechanically coupled phenomena (Berkowitz 2002; Rutqvist et al. 2002; Taron et al. 2009).

The "geometric aperture" h_G (m) reflects both the roughness of the two rock surfaces in contact and the matedness between them (Barton et al. 1985). The direct measurement of aperture in the laboratory relies on resin injection and casting, or tomographic imaging based on X-rays or nuclear magnetic resonance NMR. However, limitations in these techniques such as specimen size, partial fluid invasion, volume changes during curing, and low resolution limited by specimen size hinder the accuracy of casting and imaging methods (Pyrak-Nolte et al. 1987; Sharifzadeh et al. 2008; Keller 1998; Dijk et al. 1999; Bertels et al. 2001). On the other hand, indirect methods measure the roughness of the two fracture surfaces and infer geometric aperture numerically for a given relative positioning of the two surfaces (Brown and Kranz 1986; Lanaro 2000; Vogler et al. 2018).

The following sub-sections introduce the tested materials and roughness measurements, present analyses based on power spectra either compiled from the literature or computed from the measurements and digitized JRC profiles, and advance a protocol to create synthetic fracture surfaces using power spectra information. These synthetic surfaces, combined with fracture matedness define the fracture aperture.

2.1 Fracture Surface Roughness—Measurement

Empirical approaches simplify the characterization of surface roughness for engineering analyses, however, they are not adequate for quantitative aperture studies. The qualitative joint roughness coefficient JRC is a salient example (Barton 1973; Beer et al. 2002).

Detailed fracture roughness measurement techniques use either contact probes or optical techniques (Leach 2011; Tarolli 2014). In particular, optical methods from field devices such as LIDAR to laboratory electron microscopy span 8–10 orders of magnitude in scale, and often involve laser scanning or light interferometry.

We measured the surface roughness of natural and artificially fractured limestones using a table-top chromatic confocal interferometer (Nanovea ST400). Smooth surfaces were produced using a polishing device (Kent KGS618), whereas sandblasted surfaces used a water–sand jet (MBA Wet Blaster). We also measured the roughness of a natural fracture present in a limestone core. Insets in Fig. 1 present the scans obtained for 15 × 15 mm polished and sandblasted limestone surfaces and a 10 × 10 mm natural fracture surface. The height resolution is 0.2 μm. The peak-to-valley distance ranges from 60 μm for the polished surface to 600 μm for the sandblasted and natural surfaces.

2.2 Fracture Surface Roughness—Analysis

The analysis of roughness data involves amplitude and texture descriptors. Amplitude refers to elevation normal to the mean fracture plane, while texture considers patterns on the

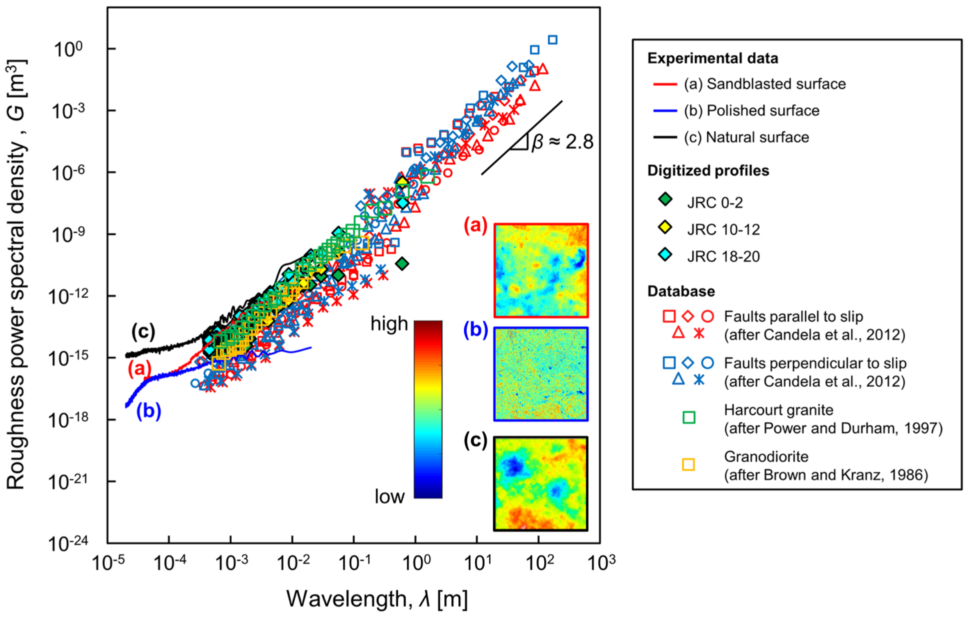

Fig. 1 Roughness power spectral density $G(\lambda)$ derived from 1D fractures and faults profiles. The wavelength λ scale spans eight orders of magnitude. As the legend on the right indicates, empty markers correspond to published data (references below) filled markers are data from digitized JRC-profiles, and solid lines correspond to the average power spectrum of the three carbonate specimens profiles tested in this study. Insets correspond to interferometer surface scans of three tested specimens: **a** 15 × 15 mm sandblasted specimen (color-bar indicates surface roughness and varies from 0 to 600 μm); **b** 15 × 15 mm polished specimen (roughness color-bar varies from 0 to 60 μm); **c** 10 × 10 mm natural fracture (color-bar varies from 0 to 600 μm). Empty red markers indicate profiles of exhumed faults surfaces parallel to slip and blue markers show profiles perpendicular to the slip direction. Squares: Magnola, Diamonds: Corona Heights; Triangles: Vuache-Sillingly; Circles: Dixie Valley; Star: Bolu (after Candela et al. 2012). Green empty squares are a natural surface in Harcourt Granite (after Power and Durham 1997). Orange empty squares correspond to a granodiorite from Fenton Hill, New Mexico (after Brown and Kranz 1986)

plane. Table 1 summarizes statistical parameters that are used to evaluate amplitude and texture. These parameters readily reveal the challenges in roughness characterization; for example, slope and curvature values are not unique but depend on the sampling interval and computation method, and amplitude distributions depend on specimen length and suggest nonstationary randomness (Majumdar and Bhushan 1990; Sayles and Thomas 1978). In fact, roughness studies highlight the inherent link between roughness values, the measurement scale, and resolution.

The surface roughness power spectral density provides unbiased amplitude and texture information (Power and Tullis 1991; Jacobs et al. 2017). We followed a five-step procedure to compute the surface roughness power spectrum: (1) measure 500 parallel roughness profiles on the specimen surface (lateral spacing between linear scans = 20 µm), (2) remove the linear trend for each profile, (3) window the detrended signal with a 3% cosine taper to reduce leakage, (4) compute the normalized power spectral density G (m^3) using the Fast Fourier Transform and (5) average the spectra for the 500 parallel profiles to obtain an equivalent 1D representation. Inherently, this procedure imposes a high-pass filter whereby wavelengths longer than the specimen size are filtered out. Figure 1 shows the roughness power spectral densities for three limestone surfaces: polished, sandblasted and a natural fracture.

2.3 Fracture Surface Roughness—Database

We compiled an extensive database of power spectra for rock surfaces in various lithologies including carbonates and granites. Surfaces involved exhumed faults parallel and perpendicular to slip (i.e., meter scale), laboratory specimens (i.e., centimeter scale), and digitized JRC fracture profiles. Laboratory specimens included fractures recovered from cores, created during strength testing, or sawed-polished, and sandblasted surfaces (measured in this study—Sect. 2.1). Figure 1 presents spectral densities as a function of wavelength λ (m) for the complete dataset. The various datasets involved different devices (i.e., LiDAR, profilometers, and interferometers) and spectral data analyses, yet, most of the data collapses onto a narrow trend. In fact, the roughness power spectrum of laboratory and natural fractures and faults follows a power law with respect to wavelength:

$$G(\lambda) = \alpha \left(\frac{\lambda}{[m]} \right)^{\beta}. \tag{1}$$

The power law implies a fractal surface topography (Mandelbrot et al. 1984; Katz and Thompson 1985; Power and Durham 1997). The parameters for the overall trend are $\alpha = 6 \times 10^{-7}$ m^3 and $\beta = 2.8$, where the α-factor is the spectral density for $\lambda = 1$ m, and the β-exponent is related to the fractal dimension (Brown 1995).

The fractal nature of surface roughness extends from geological features (e.g., strata in sedimentary rocks and faults) to the grain/crystal scale. Indeed, data in Fig. 1 suggest that this power law relationship remains valid over six orders of magnitude, and provides a convenient framework to relate laboratory measurements to the field scale.

We analyzed the individual roughness trends for all specimens in the database. In all cases, spectral densities fall along the main power trend in Fig. 1, but exhibit a range of α-factors [2×10^{-10} to 7×10^{-4} m^3] and β-exponents [1.9–3.0]. The α-factor and β-exponent increase with JRC roughness (for example: $\alpha = 2 \times 10^{-8}$ m^3 and $\beta = 2.1$ for JRC 0–2, while $\alpha = 4 \times 10^{-7}$ m^3 and $\beta = 2.4$ for JRC 18–20). Deviations from the global trend occur at large wavelengths for "smooth" profiles, e.g., $\lambda > 10^{-3}$ m for our polished limestone surface and $\lambda > 10^{-2}$ m for the JRC 0–2. These results indicate non-natural smoothness and suggest inherent limitations in the use of artificially roughened specimens to study fracture processes. Similar studies refer to this transition as corner frequency (Chen and Spetzler 1993).

The following sub-section uses this power–law relationship and proposes a methodology to create synthetic fracture surfaces.

Table 1 Amplitude and texture descriptors for fracture roughness (Thomas 1998; Magsipoc et al. 2020)

Amplitude descriptor		Texture descriptor	
Average roughness, R_a	$R_a = \frac{1}{N}\sum_{i=1}^{N} \lvert z_i \rvert$	Mean slope, m	$m = \frac{1}{N-1}\sum_{i=1}^{N-1} \frac{z_{i+1}-z_i}{\Delta z}$
Root-mean-square, RMS	$\text{RMS} = \sqrt{\sum_{i=1}^{N} z_i^2 \frac{1}{N}}$	Peak curvature, C_p	$C_p = \frac{1}{N-2}\sum_{i=1}^{N-2} \frac{2z_i - z_{i-1} - z_{i+1}}{\Delta z^2}$
Skewness, S_k	$S_k = \frac{1}{N\,\text{RMS}^3}\sum_{i=1}^{N} z_i^3$	Semivariogram, $s(\tau)$	$s(\tau) = \frac{1}{2(N-\tau)}\sum_{i=1}^{N-\tau} \left(z_{i+h} - z_i\right)^2$
Kurtosis, K	$K = \frac{1}{N\,\text{RMS}^4}\sum_{i=1}^{N} z_i^4$		

2.4 Numerical Generation of Rough Surfaces

The power spectral density $G(\lambda)$ for a given wavelength λ is a function of the corresponding sinusoid amplitude $X(\lambda)$ (m):

$$G(\lambda) = \frac{N\Delta x}{4}[X(\lambda)]^2, \tag{2}$$

where N is the number of digital values in a given profile and Δx (m) the sampling interval. Note that the scaling factor ($N\Delta x/4$) in Eq. 2 depends on the selected Fourier pair and transform definition (i.e., one-sided vs. two-sided). Nevertheless, Eqs. 1 and 2 relate amplitudes X_u and X_v to their corresponding wavelengths λ_u and λ_v regardless of the scaling factor

$$\frac{X_u}{X_v} = \left(\frac{\lambda_u}{\lambda_v}\right)^{\beta/2}. \tag{3}$$

Alternatively, given a signal length $N \cdot \Delta x$, the sinusoid amplitude $X(\lambda)$ for a given wavelength can be computed in terms of the fitted α and β parameters

$$X(\lambda) = 2\sqrt{\frac{1}{N\Delta x}\alpha\left(\frac{\lambda}{[m]}\right)^{\beta}}. \tag{4}$$

The power spectrum lacks phase information, thus we assumed a uniformly distributed random phase $\phi(\lambda)$. Together $X(\lambda)$ and $\phi(\lambda)$ define the fracture roughness in the frequency domain. We imposed a wavelength cutoff of one-fifth of the fracture length to avoid the lower order periodicity in computed profiles (i.e., high-pass filtering): this cutoff value is the longest wavelength that does not generate preferentially oriented ridges and valleys (Matsuki et al. 2006; Briggs et al. 2017). Finally, we computed the Inverse Fast Fourier Transform to determine roughness profiles in space. This methodology can be readily extended to 2D surfaces, and both the linear 1D and surface 2D algorithms satisfy Parseval's identity.

2.5 Matedness

We created fractures by bringing two rough surfaces together. Perfectly mated fractures have zero geometric aperture, thus null hydraulic transmissivity. Power spectral analyses help assess the characteristic length for surfaces matching, i.e., a mismatched length scale (Glover et al. 1997; Ogilvie et al. 2006). However, the lack of phase information in power spectra means that two surfaces with identical spectra can result in mismatched topography and non-zero apertures. Other matedness descriptors rely on contact area or joint matching coefficient JMC but disregard the wavelength-dependent correlation between the surfaces (Zhao 1997; Grasselli 2001).

3 Contact Mechanics

This section combines numerical realizations of fracture surfaces (Sect. 2.4), contact mechanics, and kinematic deformation to anticipate fracture deformation and the resulting aperture during normal loading and shear displacement. The simple yet robust approach proposed herein is physics-based and further validated against experimental data.

3.1 Normal Stress

The fracture contact area and stiffness increase and the mean aperture decreases with increasing normal stress (Iwano and Einstein 1995; Nemoto et al. 2009). Some analyses adopt a non-linear elastic contact model whereby the fracture roughness is an assembly of spheres or cylinders (Greenwood et al. 1966; Hopkins et al. 1987). Other analyses assume that fracture surfaces interpenetrate and overlap each other to reach a prescribed displacement, contact area, or fluid transmissivity (Watanabe et al. 2008; Li et al. 2015; Souley et al. 2015). These are inherently non-elastic fracture models and often involve numerical algorithms that incorporate elasto-plastic behavior of the contacts (Walsh et al. 2008; Kling et al. 2018).

We adopted the interpenetration model and assumed a perfectly rigid-plastic rock response. Since the true contact area $A_c(\sigma)$ (m^2) is minimal compared to the fracture apparent area A_f (m^2), we assumed that all contact points reached the yield stress of the material σ_{yield} (MPa); then, equilibrium with the far field normal stress σ (MPa) implies:

$$\frac{\sigma}{\sigma_{\text{yield}}} = \frac{A_c(\sigma)}{A_f}. \tag{5}$$

The algorithm brings fracture surfaces together by imposing a displacement δ_v until the interpenetration contact area $A_c(\sigma)$ is sufficient to resist the applied stress σ. Figure 2 compares experimental and numerical results for the sandblasted limestone specimen. The fitted yield stress $\sigma_{\text{yield}} = 200$ MPa exceeds the measured unconfined compressive strength UCS = 70–90 MPa by a factor of three; this reflects differences in mono-crystal asperities vs. poly-crystal specimens, boundary conditions, and the low aspect ratio of the asperities compared to the 2:1 ratio used for cylindrical specimens during UCS testing (ASTM 2014; Tuncay and Hasancebi 2009). The insets in Fig. 2 illustrate the apertures computed at 0 MPa ($\delta_v = 0$ mm) and 12 MPa ($\delta_v \approx 0.2$ mm). The preferential deformation around edges reflects the global convex geometry observed in sandblasted specimens.

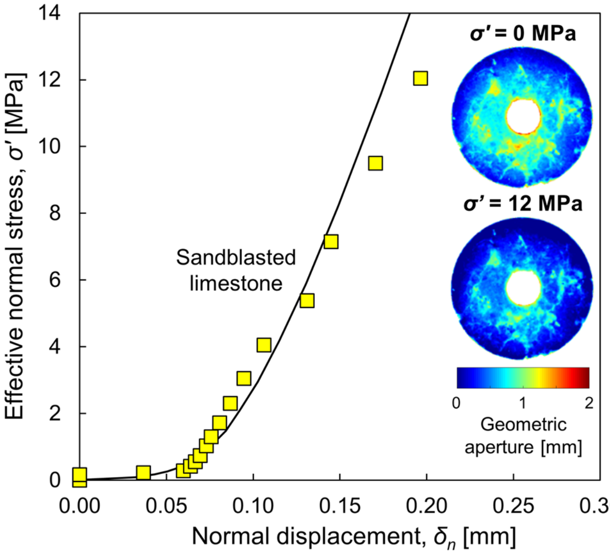

Fig. 2 Fracture normal displacement data due to applied normal stress. Sandblasted limestone specimen (yellow markers). Predicted response (continuous line): the rigid-plastic contact model assumes a yield stress of 200 MPa. Insets reflect aperture maps computed at 0 MPa ($\delta_v = 0$ mm) and 12 MPa ($\delta_v \approx 0.2$ mm), respectively

We explore the effect of normal stress on aperture size distribution using numerically generated surfaces. Figure 3a shows the distribution of local aperture for a normally compressed fracture; Fig. 3b shows mean trends computed from 1000 unmated synthetic fracture realizations (following the approach described in Sect. 2.4). Increments in normal stress shift the aperture size distribution toward smaller values; the cutoff at zero aperture corresponds to the true contact area $A_c(\sigma)$. Truncated Gaussian distributions properly represent the computed histograms in all cases tested as part of this study (see also Barr and Sherrill 1999; Xiong et al. 2018).

3.2 Shear Displacement

Shear-induced dilation and contraction are a consequence of surface roughness and initial matedness, asperity overriding, roughness wear, and degradation, and the consequent progressive generation of gouge material. The normal stress on the fracture surface determines the tradeoff between dilation during asperity overriding and asperity breakage (Barton 1973; Gutierrez et al. 2000). Typical normal versus shear displacement behavior exhibits some initial contraction followed by dilation toward an asymptotic aperture. The dilatancy rate is maximum at peak shear strength. Existing models attempt to capture these effects through geometrical descriptors, spectral information, or JRC-based qualifiers (Grasselli et al. 2002; Asadollahi and Tonon 2010).

Initial matedness is particularly relevant to the evolution of aperture size distributions during the early stages of shear displacement. In the following analysis, we used synthetically generated 1D roughness profiles to explore two matedness cases: (1) an initially "perfectly mated" fracture composed of two mirror surfaces, and (2) an initially "unmated" fracture composed of two distinct surfaces each created with the amplitude power law $X(\lambda)$ and random phase $\phi(\lambda)$ for each wavelength. Figure 4 illustrates the mean aperture size distribution obtained using 1000 realizations for unmated fractures. These results suggest that shear displacement does not affect the aperture size distribution of initially unmated fractures. By contrast, the mean and standard deviation increase with shear displacement in initially mated fractures, and reach a maximum mean aperture value when the shear displacement δ_s is half of the longest roughness wavelength, $\delta_s \sim \lambda_{\max}/2$ (Fig. 5a).

We extended the previous analysis to include the combined effects of shear displacement (imposed first) and normal stress (Eq. 5). Figure 5a displays the mean aperture size

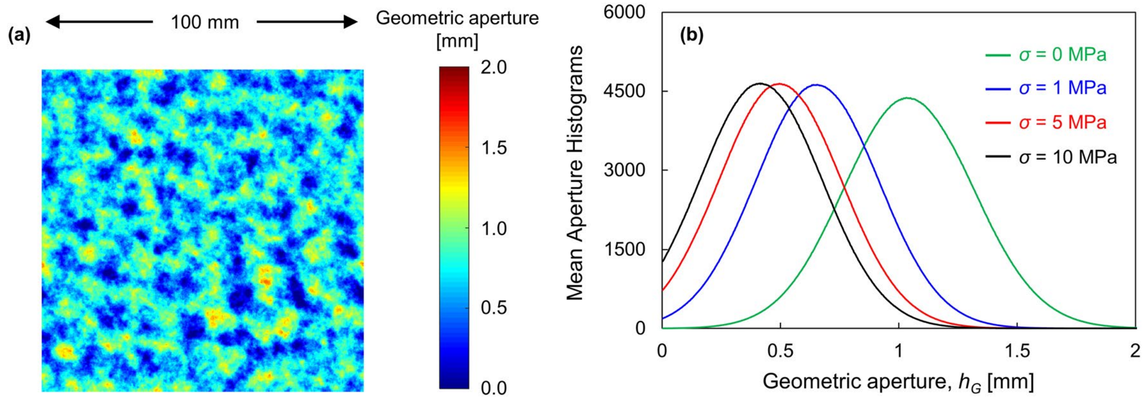

Fig. 3 Evolution of aperture size distribution during normal loading for numerically generated surfaces. **A** Aperture field estimated using the contact yield model at 1 MPa for a fracture composed of two unmated synthetic surfaces. **B** Evolution of the aperture size distribution with normal stress (mean of 1000 realizations—$\sigma_{yield} = 200$ MPa). 1D profiles are 100 mm long, and wavelengths range between $\lambda_{min} = 0.02$ mm and $\lambda_{max} = 20$ mm

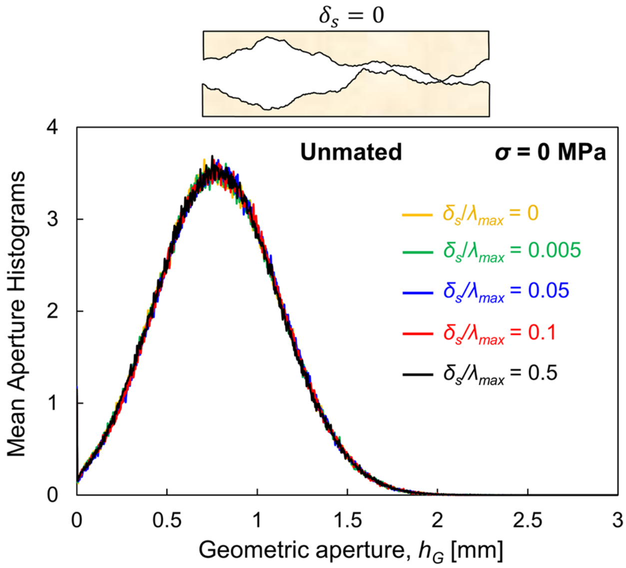

Fig. 4 Aperture size distributions during shear displacement for initially unmated fractured surfaces. Mean aperture histograms for 1000 roughness realizations. Numerically generated surfaces are 100 mm long and have a maximum wavelength $\lambda_{max} = 20$ mm. The shear displacement δ_s is normalized by λ_{max} shows the lateral offset. Note: the roughness profile shown has an exaggerated vertical scale for clarity

distribution obtained from 1000 realizations at normal stress $\sigma = 0$ MPa for initially mated fracture surfaces after four different shear displacements. Figure 5b shows aperture histograms after normal loading to $\sigma = 10$ MPa. The effects of normal loading and asperity yield after shear displacement on aperture size distribution are more pronounced as matedness decreases with increased shear displacement. Note that the adopted contact model does not consider asperity shear.

4 Flow: Hydraulic Aperture

Flow follows the path of least drag in a variable aperture field. Thus, flow trajectories deviate from linear streamlines. A fracture's "hydraulic aperture" h_H is the equivalent aperture between two parallel flat plates that allow the same flow for the same pressure gradient assuming the cubic law (Witherspoon et al. 1980). Estimates of the hydraulic aperture are based on statistics (Table 2). Interestingly, most models anticipate that the hydraulic aperture decreases as the aperture coefficient of variation s_G/μ_G increases where s_G is the aperture standard deviation and μ_G its mean. Analogous conclusions using network models for a wide range of pore size distributions can be found in Jang et al. (2011). Numerical studies, new experimental data, and data compiled from published studies are used herein to extend previous fracture flow analyses.

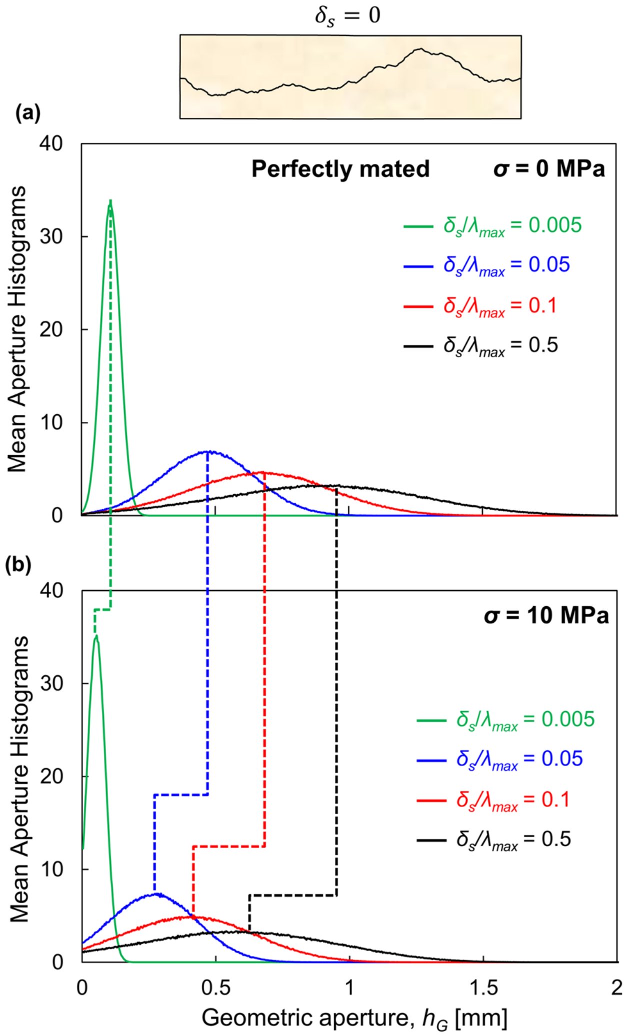

Fig. 5 Evolution of aperture size distribution during shear displacement for initially mated fractures. Mean aperture histograms for 1000 realizations. **A** $\sigma = 0$ MPa, **B** Normal stress $\sigma = 10$ MPa imposed after shear displacement. Dashed lines relate histograms before and after normal load. Note: the roughness profile shown has an exaggerated vertical scale for clarity

4.1 Numerical Study: Evolution of Transmissivity with Normal Stress and Shear Displacement

We assumed the cubic law to be locally valid. Then, Stokes flow and continuity requirements result in the following expression, similar to the seepage flow equation for a heterogeneous medium (Oron and Berkowitz 1998):

$$\frac{\partial}{\partial x}\left(h_G^3 \frac{\partial P}{\partial x}\right) + \frac{\partial}{\partial y}\left(h_G^3 \frac{\partial P}{\partial y}\right) = 0, \tag{6}$$

where h_G is geometric aperture.

This equation assumes that (1) roughness amplitudes X are much smaller than the roughness wavelength λ ($\lambda/X \gg 1$),

Table 2 Hydraulic aperture models

Model	References
$\frac{h_H^3}{\mu_G^3} = \left(\frac{\mu_G/\mu m}{\mathrm{JRC}^{2.5}}\right)^3$	Barton et al. (1985); Esaki et al. (1999)
$\frac{h_H^3}{\mu_G^3} = \frac{1}{1+A_H\left(\frac{2\mu_G}{s_G}\right)^{1.5}}$	Lomize (1951), Brown (1987)
$\frac{h_H^3}{\mu_G^3} = \left(1 - C_H\, e^{-B_H\left(\frac{\mu_G}{s_G}\right)}\right)$	Partir and Cheng (1978)
$\frac{h_H^3}{\mu_G^3} = \frac{\mu_G}{s_G}\frac{(1-c)}{(1+c)}$	Brown (1987)
$\frac{h_H^3}{\mu_G^3} = (1 - 2c)$	Li et al. (2008)
$\frac{h_H^3}{\mu_G^3} = \left[1 - 1.5\left(\frac{s_G}{\mu_G}\right)^2\right](1 - 2c)$	Zimmerman and Bodvarsson (1996); Chen et al. (2017)
$\frac{h_H^3}{\mu_G^3} = \left(1 + 3(1 - 3\alpha)S^2 + \cdots\right)$; $S = \frac{s_G}{\mu_G}; \alpha = \int \frac{\theta(\kappa)}{2\pi^2}\mathrm{d}\kappa$	Inoue and Sugita (2003); Auradou (2009)

and (2) the wavelength is much greater than the aperture ($\lambda/h_G \gg 1$). The power function between roughness and wavelength automatically satisfies the first assumption (Fig. 1 and Eqs. 1 and 3). The second assumption is valid taking into consideration the wavelength that controls the aperture. Note that two sinusoidal surfaces in contact create a $h_G = 4X$ aperture when the shear displacement is $\lambda/2$, i.e., a π-shift.

We solved Eq. 6 using finite differences and explored the implications of changes in geometrical aperture on flow due to changes in effective normal stress. Numerical results in Fig. 6 show the decrease in fracture transmissivity as the effective normal stress increases for different yield stress values σ_{yield}. Besides the reduction in aperture, the increase in contact area leaves a smaller available fracture cross section for flow. Figure 6a shows flow rate magnitudes at different stress levels for a synthetic unmated fracture: flow trajectories redistribute and flow channeling becomes more pronounced at later stages of loading because larger aperture channels remain open and control flow. In fact, the fracture area responsible for 90% of the flow reduces during loading (Fig. 6b).

Transmissivity data gathered in the field suggest that shear dilation in critically stressed natural fractures enhances fluid flow, predominantly in crystalline rocks (Barton et al. 1995). Shear displacement induces aperture anisotropy. Contact points increase in the direction of shear, detach transversely to the shear direction, and therefore, aperture ridges emerge on the fracture aperture field (Gentier et al. 1997; Yeo et al. 1998; Auradou et al. 2005; Matsuki et al. 2010). Consider a synthetic initially mated rough fracture (i.e., zero aperture) subjected to shear displacement in the y-direction (Fig. 7a). The geometric aperture field at different levels of shear displacement in Fig. 7a displays a clear alignment of

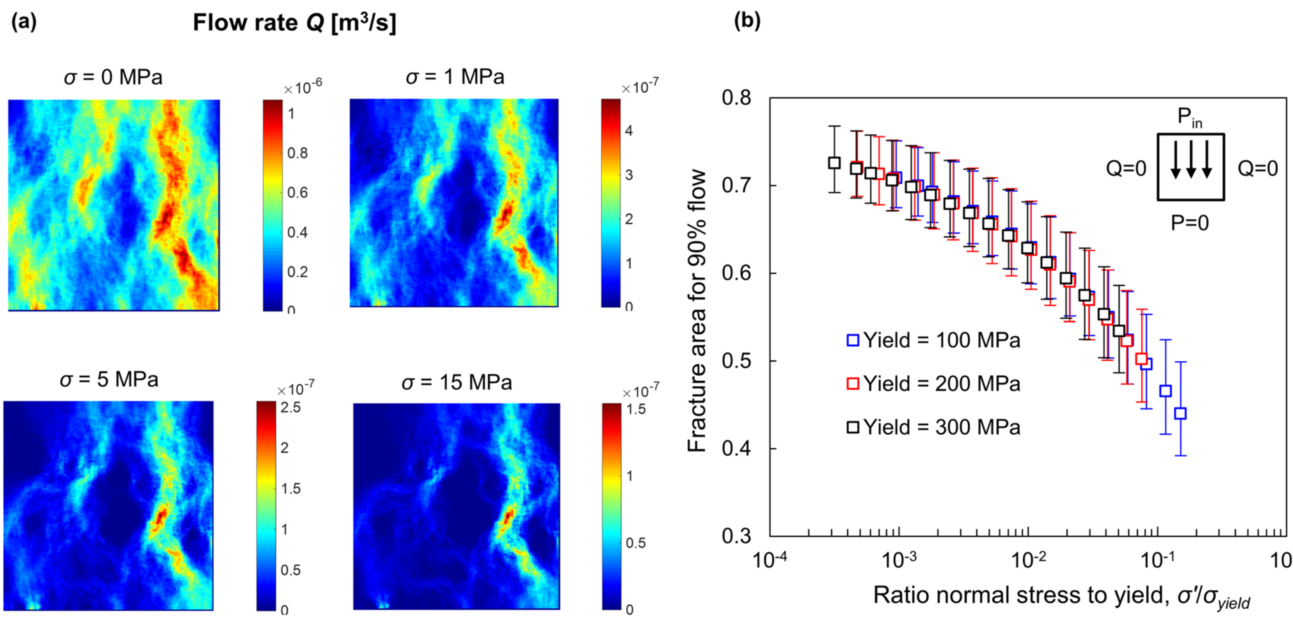

Fig. 6 Transmissivity changes due to normal load. **A** Estimated flow rates through an unmated fracture using the contact yield and local cubic law approximations for different normal stresses ($\sigma' = 0$, 1, 5, and 15 MPa—Eq. 5 for an assumed yield stress of 200 MPa). **B** The fraction of the fracture area that carries 90% of the total flow for 1000 realizations. Vertical bars indicate the 25th and 75th percentiles. The inset shows the assumed pressure gradient (top to bottom) and the no-flow side boundaries

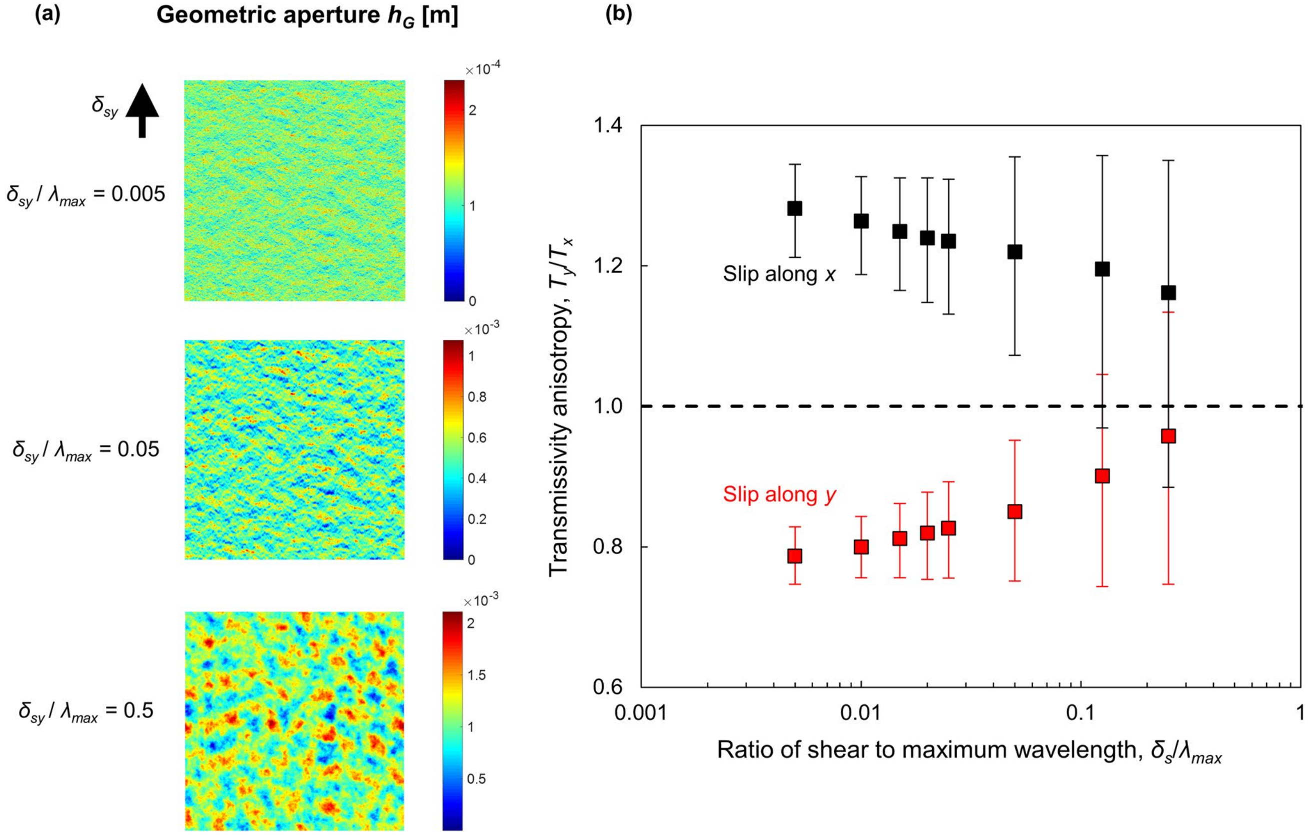

Fig. 7 Transmissivity changes during shear displacement. **A** Geometric apertures for different levels of shear displacement at 0 MPa of normal stress and initially perfectly mated fracture. **B** Evolution in transmissivity anisotropy for shear displacement along *x* and *y* directions (1000 realizations). Vertical bars indicate the 25th and 75th percentiles

apertures transverse to the shear direction at early stages of shear as discussed above. The ensuing transmissivity anisotropy is most pronounced soon after shear displacements starts $\delta_s/\lambda_{max} < 0.1$, and gradually decreases toward isotropic conditions at large shear displacements when all surface correlations are lost (Fig. 7b). Datapoints in Fig. 7b are averages of 1000 realizations, and error bars show that the anisotropy variability increases with shear displacement due to the higher probability of dominant flow paths.

4.2 Experimental Study: Torsional Ring Shear Device

Numerical results highlight profound differences in the evolution of geometric aperture and flow during normal loading and shear displacement, and the impact on natural fracture surface roughness and matedness. A focused experimental study complements this numerical study.

We designed and manufactured a torsional ring shear device to subject a pre-fractured cylindrical specimen to normal stresses up to 30 MPa, to independently apply a torsional shear displacement, and to impose radial flow through the annular fracture plane (Fig. 8). This device benefits from accurate normal stress and shear displacement control, imposes precise flow boundaries without the need for jacketed specimens, maintains a constant nominal fracture area throughout the test, and reduces stress localization (for comparison, see: linear shear in Esaki et al. 1999; biaxial tests in Makurat et al. 1990; triaxial configuration in Teufel 1987; and torsional shear in Olsson 1992).

The reaction load frame houses a pressure-controlled hydraulic jack to impose the vertical load, and two horizontal screw positioners to exert the torsional moment via diametrically opposite lever arms. Fluid is injected into the fracture plane through a small central hole drilled into the specimen's lower half. The instrumentation includes a LVDT to record the normal displacement, strain-gages mounted on the lever arms to measure torque, and two pressure transducers to monitor the fluid pressure at low and high pressure ranges.

The limestone specimen preparation method involved five steps: (1) core two 56 mm diameter cylindrical plugs, (2) modify the fracture surface by either sandblasting or polishing, (3) cut a cross-shaped groove on the other side

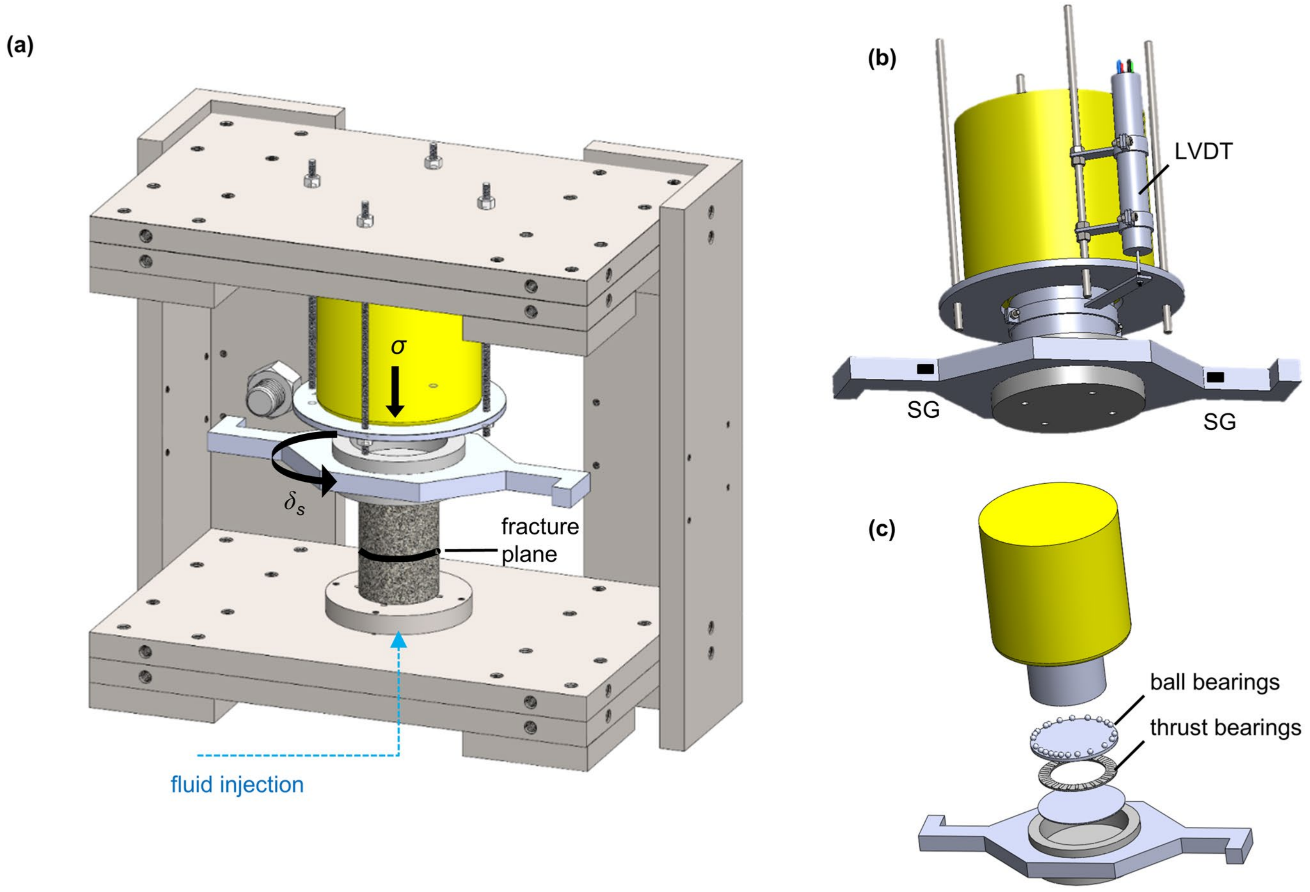

Fig. 8 Torsional shear device to assess fracture transmissivity as a function of normal stress and shear displacement. **A** Reaction frame, hydraulic cylinder for vertical load, lever arm and specimen. **B** Instrumentation: LVDT to monitor the fracture normal displacement and strain gages SG to measure the applied torque. **C** Ball bearings in the annular space between the cap and the plunger preserve the coaxility

of each plug to accommodate the torque transmission cap, (4) drill the central hole and chamber in one of the two plugs for fluid injection (hole diameter = 3.5 mm, chamber diameter = 18 mm), and (5) attach with epoxy the two steel caps onto the rock cylinders. For natural fractures, we cored across the fracture and implemented steps 3, 4, and 5 detailed above.

Figure 9 shows typical experimental results where transmissivity decreases with effective normal stress. The smooth and rough limestone specimens start with distinct geometrical aperture fields, yet their transmissivities converge as the effective normal stress exceeds ~ 1 MPa (Fig. 9a). On the other hand, the high roughness variability in a natural fracture plane, with longer asperity wavelength, localizes contact yield at few asperities; there is a reduced effect on the governing large flow channels and transmissivity exhibits lower sensitivity to normal stress (Fig. 9b). A set of five tests conducted with limestone plugs confirmed these observations.

Results in Fig. 7 call for the analysis of hydro-mechanical boundary conditions in experimental and numerical studies, relative to field conditions. For example, radial flow in our ring shear device is normal to the shear direction; on the other hand, most numerical and experimental studies impose flow collinear with shear. In addition, radial flow and torsional shear imply a radial gradient in fluid velocity and shear displacement; we minimize radial effects by limiting the ratio between the external specimen diameter and the internal chamber size (56 mm/18 mm in this study).

4.3 Transmissivity Models: Normal Stress and Shear Displacement

We compiled a database of fracture transmissivity evolution with normal stress and shear displacement for various rock types. Data sources cover a wide range of measurement techniques (e.g., linear, biaxial, and torsional shear) and boundary conditions (i.e., linear and radial flow). This database, which includes published results and our experimental results, allow us to advance new physics-inspired yet data-driven transmissivity models.

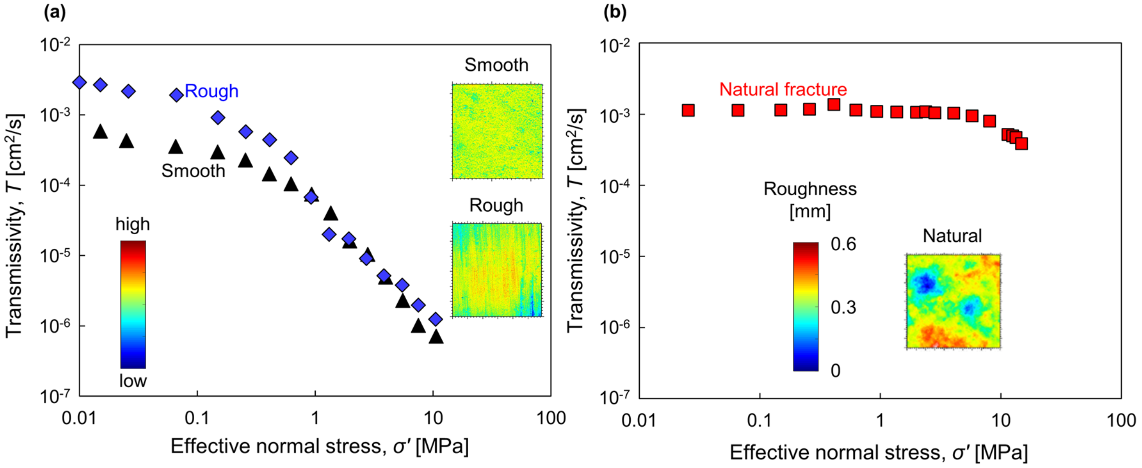

Fig. 9 Evolution of transmissivity with normal stress—Experimental data. **A** Limestone specimen with two different surface roughness. Insets correspond to roughness scans for the smooth (2.3×2.3 mm) and rough (6×6 mm) fracture surfaces. Color bar values range from 0 to 0.06 mm and from 0 to 0.1 mm, respectively. **B** Natural specimen. The inset corresponds to the roughness of a 10×10 mm specimen

4.3.1 Normal Stress

Earlier fracture transmissivity models as a function of normal stress recognized non-linear contact behavior and asperity yield, flow channeling, and the influence of fracture roughness (e.g., Pyrak-Nolte and Nolte 2016). These phenomenological models involve power, logarithmic, or exponential decay functions for transmissivity as a function of normal stress. However, these models fail to capture the asymptotic behavior of fracture transmissivity T (cm^2/s) at very low effective normal stress ($T_{\sigma 0}$ as $\sigma' \to 0$) and very high effective normal stress ($T_{\sigma\infty}$ as $\sigma' \to \infty$) and may be unreliable for general applications.

We modified a selection of published models to satisfy asymptotic behavior so that transmissivity reaches prescribed values when the effective stress approaches zero or infinity (see Table 3). Then, we fitted trends in the database with the various models. The following power–law expression provides the best fit for all cases analyzed in this study:

$$\frac{T(\sigma') - T_{\sigma_\infty}}{T_{\sigma_0} - T_{\sigma_\infty}} = \left(\frac{\sigma' + \sigma_c}{\sigma_c}\right)^{-\gamma}. \tag{7}$$

This four parameter model indicates that transmissivity $T(\sigma')$ at a given effective normal stress σ' normalized by the asymptotic values $T_{\sigma 0}$ and $T_{\sigma\infty}$ is a function of the normalized effective normal stress with respect to the characteristic stress σ_c, where the γ-exponent captures the transmissivity stress-sensitivity (Fig. 10). Note that the normalized transmissivity is $2^{-\gamma}$ when the normal stress is equal to the characteristic stress $\sigma' = \sigma_c$. Complementary numerical simulations not shown here indicate that (1) fracture roughness and matedness control the transmissivity asymptotes $T_{\sigma 0}$ and $T_{\sigma\infty}$, and (2) σ_c is a function of the rock yield stress σ_{yield}.

Figure 10 illustrates data clustering according to rock type: fractures in sandstones are more sensitive to stress (γ = 3-to-20), whereas the transmissivity in igneous and metamorphic rocks exhibits a lower stress-sensitivity (γ = 0.4-to-2). The exponent γ for limestone specimens tested in this study ranges from γ = 3-to-8.

4.3.2 Shear Displacement

Previous empirical models for transmissivity during shear displacement relate shear dilation to the joint roughness coefficient JRC or an empirical fitting factor (Table 4). Some models recognize cataclasis during shear displacement, but are complex and require shear stress information (Plesha 1987; Nguyen and Selvadurai 1998). Furthermore, available empirical and theoretical models are asymptotically incorrect, thus, unreliable for general applications.

We adopted the following logistic function with a distinct S-shaped trend in log–log scale to capture the evolution of the normalized transmissivity during shear displacement:

$$\frac{T(\delta_s) - T_{\delta_0}}{T_{\delta_\infty} - T_{\delta_0}} = \frac{e^{\left(\frac{1}{1+e^{\eta(1-\delta_s/\delta_{sc})}}-1\right)} - T_c}{1 - T_c} \quad \text{where } T_c = e^{\left(\frac{1}{1+e^{\eta}}-1\right)}. \tag{8}$$

The four parameters model capture: the sensitivity of the fracture transmissivity to shear displacement in the η-exponent, the displacement at maximum dilatancy or contractive rate in the characteristic shear displacement δ_{sc}, and the transmissivity asymptotes $T_{\delta 0}$ as $\delta_s \to 0$ and $T_{\delta\infty}$ as $\delta_s \to \infty$. This model can accommodate data that exhibits

Table 3 Fracture transmissivity models as a function of effective normal stress. Notes models are modified to satisfy asymptotic behavior

Model	Function	References
$T = T_{\sigma_\infty} + \left(T_{\sigma_0} - T_{\sigma_\infty}\right)\left(\frac{\sigma' + \sigma_c}{\sigma_c}\right)^{-\gamma}$	Power	Gale (1982); Gangi (1978)
$T = T_{\sigma_\infty} + \left(T_{\sigma_0} - T_{\sigma_\infty}\right)\exp\left(-\gamma\frac{\sigma'}{\sigma_c}\right)$	Exponential	Gutierrez et al. (2000)
$T = T_c\left[1 - \xi\ln\left(\frac{1\text{ MPa}}{\sigma' + \sigma_L} + \frac{1\text{ MPa}}{\sigma_H}\right)^{-1}\right]^3$ $\sigma_H = e^{\left(1 - \sqrt[3]{T_{\sigma\infty}/T_c}\right)/\xi}$ $\sigma_L = \frac{\sigma_H}{e^{\left(\sqrt[3]{T_{\sigma 0}/T_c} - \sqrt[3]{T_{\sigma\infty}/T_c}\right)/\xi} - 1}$ $\xi = \frac{\sqrt{2}\text{RMS}}{h_{H0}}$	Logarithmic	Walsh (1981)
$T = T_c\left[1 - \zeta\ln\left(\frac{1\text{ MPa}}{\sigma' + \sigma_L} + \frac{1\text{ MPa}}{\sigma_H}\right)^{-1}\right]^2$ $\sigma_H = e^{\left(1 - \sqrt{T_{\sigma\infty}/T_c}\right)/\zeta}$ $\sigma_L = \frac{\sigma_H}{e^{\left(\sqrt{T_{\sigma 0}/T_c} - \sqrt{T_{\sigma\infty}/T_c}\right)/\zeta} - 1}$	Logarithmic	Swan (1983)

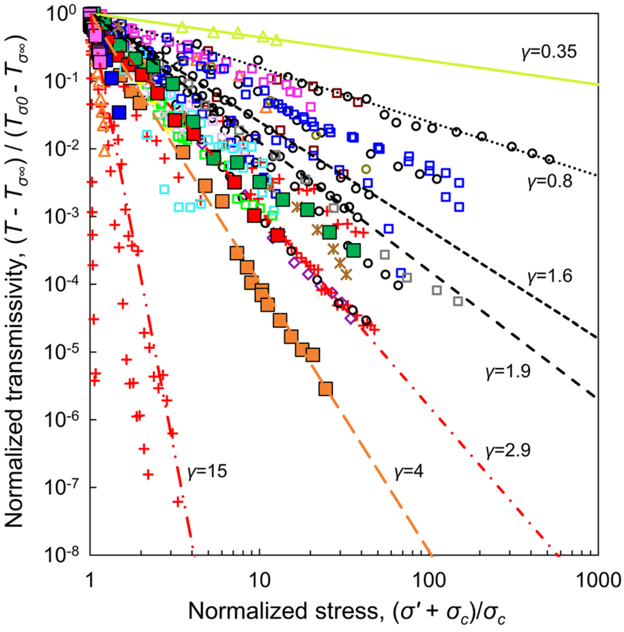

Fig. 10 Transmissivity as a function of normal stress—Experimental data and fitted power model (Eq. 7). Transmissivity normalized with respect to the transmissivity at zero and infinite normal stress $T_{\sigma 0}$ and $T_{\sigma\infty}$. Empty markers: published data. Filled markers: experimental data for limestone specimens (this study). Rock type: square-granites, diamond-granodiorites, cross-sandstones, 4 point star-marbles, triangle-shales, circle-gneiss, and 6 point star-amphibolites. Data sources: Witherspoon et al. (1980) (gray); Gale (1982) (black); Raven and Gale (1985) (blue); Brown and Kranz (1986) (purple); Makurat (1990) (olive); Wilbur and Amadei (1990) (yellow); Boulon et al. (1993) (maroon); Durham (1997) (brown); Indraratna et al. (1999) (green); Gutierrez et al. (2000) (orange); Pyrak-Nolte and Morris (2000) (magenta); Lee and Cho (2002) (lavender); Watanabe et al. (2008) (cyan); Cuss et al. (2011) (lime); Chen et al. (2017) (red)

Table 4 Fracture transmissivity models as a function of shear displacement

Model	References
$T = \frac{\rho g}{12\mu}\left(\mu_G/\mu\text{m}\right)^{3/2}\text{JRC}^3_{\text{mob}}$	Olsson and Barton (2001)
$T = \frac{\rho g}{12\mu}\left(h_{H0} + f \cdot h\right)^3$; $f = f_o\exp\left(-\int_0^{W^p} c_f\,\text{d}W^p\right)$	Plesha (1987); Nguyen and Selvadurai (1998)
$T = \frac{\rho g}{12\mu}\left(\frac{A_s}{1 + 9\frac{\sigma'_n}{B_s}}h_{H0}\right)^3$ where $A_s = \begin{cases} 1 & \text{before shear} \\ > 1 & \text{after shear} \end{cases}$	Tezuka et al. (2005)

either monotonic dilation or contraction during shear; in fact, Zhou et al. (2018) proposed a similar mathematical expression for dilation.

Figure 11 presents normalized transmissivity data plotted against the normalized shear displacement δ_s/δ_{sc} for studies reported in the literature and new data gathered in this study. The limited clustering by rock type suggests that changes in aperture are most sensitive to initial fracture roughness and matedness. In fact, complementary numerical simulations with synthetic fractures not shown in this manuscript demonstrate that roughness, matedness, and normal stress determine the transmissivity asymptotes $T_{\delta 0}$ and $T_{\delta\infty}$, and the characteristic shear displacement δ_{sc}. The η-exponent reflects the dilative tendency which is a function of surface roughness and initial matedness for a given normal stress.

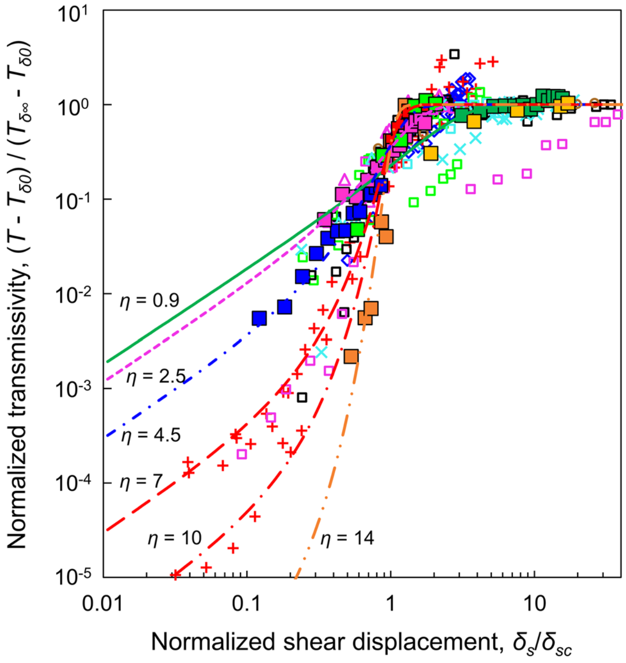

Fig. 11 Transmissivity as a function of shear displacement—Experimental data and fitted logistic model (Eq. 8). Transmissivity normalized with respect to the transmissivity at zero and infinite shear displacement $T_{\delta 0}$ and $T_{\delta\infty}$. Empty markers: published data. Filled markers: experimental data for limestone specimens (this study). Rock type: square-granites, diamond-plaster, cross-mortar, 4 point star-sandstone, triangle-marbles, welded tuff-gneiss, and 6 point star-chalk. Data sources: Makurat 1990 (cyan); Esaki et al. 1991 (black); Olsson 1992 (brown); Ahola et al. 1996 (green); Gentier et al. 1996 (gray); Cheon et al. 2002 (magenta); Li et al. 2008 (blue); Nishiyama et al. 2014 (red)

4.4 Hydro-Chemo–Mechanical Coupling: Dissolution

Carbonate rocks exhibit high solubility and high reaction rates (Plummer et al. 1978). Consequently, mineral dissolution, and precipitation play a significant role in the evolution of both geometric and hydraulic apertures. The Damkhöler number compares reaction kinetics and advective transport, while the transverse Peclet number contrasts longitudinal advective transport to diffusive transport across the fracture (Fredd and Fogler 1998; Golfier et al. 2002). These two dimensionless ratios help anticipate the type of transport regime: homogeneous dissolution, near-inlet dissolution, or channeling (Elkhoury et al. 2013; Deng et al. 2015).

Mineral dissolution impacts the aperture evolution for a given normal stresses. We explored the evolution of fracture transmissivity due to reactive fluid flow across a limestone specimen with an initially polished fracture surface using our annular fracture flow device. Figure 12 presents the fracture transmissivity and normal displacement data during loading and unloading before acid treatment. The initial transmissivity-stress trends obtained with water follow a typical compaction behavior, where transmissivity decreases as effective normal stress increases. We injected 5 cm^3 of a pH = 2 HCl-solution at 1 cm^3/min under constant normal stress $\sigma_z = 0.55$ MPa. For a diffusion coefficient $D = 2\times10^{-9}$ m^2/s, mean fracture aperture $h_H = 25$ μm, and kinetic rate $k = 3.2$ s^{-1}, the Damkhöler and Peclet numbers are Da = 9.1 and Pe = 2.7×10^{-2} respectively (see Kim and Santamarina 2016 for detailed Da and Pe definitions). These high Damkhöler and Peclet numbers imply fast reaction and seepage which cause near-inlet dissolution. Then, we

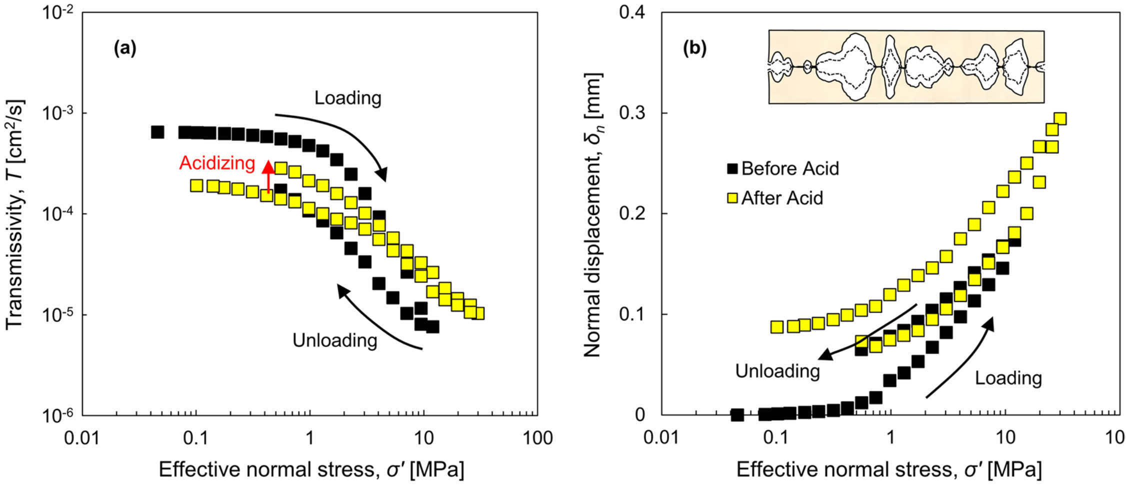

Fig. 12 Fracture transmissivity changes due to dissolution. Limestone subjected to the injection of HCl solution-pH 2 at 1 cm^3/min. (A) Fracture transmissivity versus effective normal stress and (B) normal displacement versus effective normal stress before (black) and after (yellow) acidizing treatment. The inset sketch illustrates the hypothesized aperture evolution following dissolution (dashed lines: surface before acidization)

measured transmissivity and normal displacement during a second loading–unloading cycle. There is a marked increment in fracture transmissivity during acid injection and insignificant changes in normal displacement. Thereafter, gains in transmissivity remain during loading even at high stress. This observation suggests the formation of dissolution channels during the acid treatment while the true contact area between fracture planes remains unaltered (see inset in Fig. 12).

5 Conclusions

Fluid flow in fractured rock masses is a common phenomenon in natural and engineered systems, from infrastructure applications to resource recovery and CO_2 geological storage. Fracture transmissivity along fractures defines the prevalent flow paths and controls all forms of hydro-thermo-chemo-bio-mechanically coupled processes. This study combined data compilation, new experimental data, and numerical studies to advance the understanding of fracture roughness, aperture, and transmissivity.

The fracture roughness reflects mineralogy and fabric at small scales compounded by kinematics at large scales. The power spectral density captures the inherent interplay between surface roughness amplitude and wavelength: $(X_u/X_v) = (\lambda_u/\lambda_v)^{\beta/2}$ where β ranges from $\beta = 1.9$ to 3. When plotted against wavelength, roughness power spectral density data cluster along a single trend for more than eight orders of magnitude in roughness wavelength with a global $\beta \approx 2.8$. Deviations from this trend at large wavelengths in artificially roughened specimens suggest non-natural smoothness and highlight experimental limitations to study large scale fracture processes. Nevertheless, the fractal nature of surface roughness provides a convenient framework for analytical and numerical studies.

Specimen size limitations and fractal characteristics limit physical experiments. Statistical numerical experimentation appear as a valuable approach to study fracture transmissivity. Our normal contact and kinematically based shear models provide first-order insight on fracture deformation. The power function between fracture roughness and wavelength automatically guarantees the validity of the simplified Navier–Stokes model (i.e., local cubic law).

Surface roughness and matedness define fracture aperture and its evolution during normal loading and shear displacement. Normal stress increments cause contact yield, fracture closure, and changes in the fracture void space. The closure of small local apertures increases the relative contribution of larger interconnected voids and promotes flow channeling. Rougher unmated surfaces preserve channels during loading, and transmissivity exhibits lower stress sensitivity. An asymptotically correct power function accurately captures the evolution of transmissivity with normal stress. Model parameters reflect initial roughness, matedness, and mineralogy.

The shear displacement of unmated fractures results in statistically identical aperture fields. By contrast, shear displacement increases both the aperture mean and standard deviation in initially mated fractures; in this case, contacts align along ridges transversely to the shear direction and lead to anisotropy in transmissivity during early stages of shear displacement. However, anisotropy decreases as the shear displacement increases (relative to the largest wavelength present in the fracture). A logistic function represents transmissivity changes with shear displacement. The fracture roughness, initial matedness, and normal stress relative to yield determine the transmissivity asymptotes.

Reactive flow modifies the void space. The impact of dissolution on fracture transmissivity depends on the rates of reaction, diffusion, and advection. In high advective regimes, transmissivity increases due to positive advective-reactive feedback and channeled erosion, even at minimal normal fracture displacement.

Acknowledgements Support for this research was provided by the KAUST Endowment at King Abdullah University of Science and Technology with additional funding by Saudi ARAMCO. G. E. Abelskamp edited the manuscript. M. Sanmurjana contributed to the design of the torsional ring shear device.

Code Availability Not applicable.

Declarations

Conflict of Interest The authors declare that they have no conflict of interest.

Availability of Data Not applicable.

References

Ahola MP, Mohanty S, Makurat A (1996) Coupled mechanical shear and hydraulic flow behavior of natural rock joints. In: Stephansson O, Jing L, Tsang CF (eds) Developments in geotechnical engineering: coupled thermo-hydro-mechanical processes of fractured media, vol 79. Elsevier, Amsterdam, pp 393–423. https://doi.org/10.1016/S0165-1250(96)80034-4

Al-Fahmi MM, Ozkaya SI, Cartwright JA (2018) New insights on fracture roughness and wall mismatch in carbonate reservoir rocks. Geosphere 14(4):1851–1859. https://doi.org/10.1130/ges01612.1

Asadollahi P, Tonon F (2010) Constitutive model for rock fractures: revisiting Barton's empirical model. Eng Geol 113:11–32. https://doi.org/10.1016/j.enggeo.2010.01.007

Auradou H (2009) Influence of wall roughness on the geometrical, mechanical and transport properties of single fractures. J Phys D Appl Phys. https://doi.org/10.1088/0022-3727/42/21/214015

Auradou H, Drazer G, Hulin JP, Koplik J (2005) Permeability anisotropy induced by the shear displacement of rough fracture walls. Water Resour Res. https://doi.org/10.1029/2005WR003938

Aydin A (2000) Fractures, faults, and hydrocarbon entrapment, migration and flow. Mar Pet Geol 17(7):797–814. https://doi.org/10.1016/S0264-8172(00)00020-9

Barr DR, Sherrill ET (1999) Mean and variance of truncated normal distributions. Am Stat 53(4):357–361. https://doi.org/10.2307/2686057

Barton N (1973) Review of a new shear-strength criterion for rock joints. Eng Geol 7(4):287–332. https://doi.org/10.1016/0013-7952(73)90013-6

Barton N, Bandis S, Bakhtar K (1985) Strength, deformation and conductivity coupling of rock joints. Int J Rock Mech Min Sci Geomech Abstr 22(3):121–140. https://doi.org/10.1016/0148-9062(85)93227-9

Barton CA, Zoback MD, Moos D (1995) Fluid flow along potentially active faults in crystalline rock. Geology 23(8):683–686. https://doi.org/10.1130/0091-7613(1995)023%3c0683:FFAPAF%3e2.3.CO;2

Beer AJ, Stead D, Coggan JS (2002) Estimation of the joint roughness coefficient (JRC) by visual comparison. Rock Mech Rock Eng 35(1):65–74. https://doi.org/10.1007/s006030200009

Berkowitz B (2002) Characterizing flow and transport in fractured geological media: a review. Adv Water Resour 25(8):861–884. https://doi.org/10.1016/S0309-1708(02)00042-8

Bertels SP, DiCarlo DA, Blunt MJ (2001) Measurement of aperture distribution, capillary pressure, relative permeability, and in situ saturation in a rock fracture using computed tomography scanning. Water Resour Res 37(3):649–662. https://doi.org/10.1029/2000wr900316

Boulon MJ, Selvadurai APS, Benjelloun H, Feuga B (1993) Influence of rock joint degradation on hydraulic conductivity. Int J Rock Mech Min Sci Geomech Abstr 30(7):1311–1317. https://doi.org/10.1016/0148-9062(93)90115-T

Briggs S, Karney BW, Sleep BE (2017) Numerical modeling of the effects of roughness on flow and eddy formation in fractures. J Rock Mech Geotech Eng 9(1):105–115. https://doi.org/10.1016/j.jrmge.2016.08.004

Brodsky EE, Kirkpatrick JD, Candela T (2016) Constraints from fault roughness on the scale-dependent strength of rocks. Geology 44(1):19–22. https://doi.org/10.1130/g37206.1

Brown SR (1987) Fluid flow through rock joints: the effect of surface roughness. J Geophys Res Solid Earth 92(B2):1337–1347. https://doi.org/10.1029/JB092iB02p01337

Brown SR (1995) Simple mathematical model of a rough fracture. J Geophys Res 100(B4):5941–5952. https://doi.org/10.1029/94JB03262

Brown SR, Kranz RL (1986) Correlation between the surfaces of natural rock joints. Geophys Res Lett 13(13):1430–1433. https://doi.org/10.1029/GL013i013p01430

Brown SR, Scholz CH (1986) Closure of Rock Joints. J Geophys Res 91(B5):4939–4948. https://doi.org/10.1029/JB091iB05p04939

Candela T, Renard F, Klinger Y, Mair K, Schmittbuhl J, Brodsky EE (2012) Roughness of fault surfaces over nine decades of length scales. J Geophys Res. https://doi.org/10.1029/2011JB009041

Chen G, Spetzler H (1993) Topographic characteristics of laboratory induced shear fractures. PAGEOPH 140(1):123–135. https://doi.org/10.1007/bf00876874

Chen Y, Liang W, Lian H, Yang J, Nguyen VP (2017) Experimental study on the effect of fracture geometric characteristics on the permeability in deformable rough-walled fractures. Int J Rock Mech Min Sci 98:121–140. https://doi.org/10.1016/j.ijrmms.2017.07.003

Cheon D, Lee H, Jeon S, Lee C (2001) A study of hydromechanical behaviors of rock joints using torsional shearing system. In: Proceedings of the ISRM 2nd Asian Rock Mechanics Symposium, Beijing, China, pp 185-188. ISRM-ARMS2-2001-039

Cuss RJ, Milodowski A, Harrington JF (2011) Fracture transmissivity as a function of normal and shear stress: first results in Opalinus Clay. Phys Chem Earth Parts a/b/c 36(17–18):1960–1971. https://doi.org/10.1016/j.pce.2011.07.080

Deng H, Fitts JP, Crandall D, McIntyre D, Peters CA (2015) Alterations of fractures in carbonate rocks by CO2-acidified brines. Environ Sci Technol 49(16):10226–10234. https://doi.org/10.1021/acs.est.5b01980

Dijk P, Berkowitz B, Bendel P (1999) Investigation of flow in water-saturated rock fractures using nuclear magnetic resonance imaging (NMRI). Water Resour Res 35(2):347–360. https://doi.org/10.1029/1998wr900044

Durham WB (1997) Laboratory observations of the hydraulic behavior of a permeable fracture from 3800 m depth in the KTB pilot hole. J Geophys Res Solid Earth 102(B8):18405–18416. https://doi.org/10.1029/96jb02813

Elkhoury JE, Ameli P, Detwiler RL (2013) Dissolution and deformation in fractured carbonates caused by flow of CO2-rich brine under reservoir conditions. Int J Greenh Gas Control. https://doi.org/10.1016/j.ijggc.2013.02.023

Esaki T, Du S, Mitani Y, Ikusada K, Jing L (1999) Development of a shear-flow test apparatus and determination of coupled properties for a single rock joint. Int J Rock Mech Min Sci 36(5):641–650. https://doi.org/10.1016/S0148-9062(99)00044-3

Fredd CN, Fogler HS (1998) Influence of transport and reaction on wormhole formation in porous media. AIChE J 44(9):1933–1949. https://doi.org/10.1002/aic.690440902

Gale JE (1982) The effects of fracture type (induced versus natural) on the stress-fracture closure-fracture permeability relationships. In: Proceedings of the ARMA 23rd U.S. Symposium on Rock Mechanics, Berkeley, California, ARMA-82-290

Gale JE (1987) Comparison of coupled fracture deformation and fluid flow models with direct measurements of fracture pore structure and stress-flow properties. Proceedings of the ARMA 28th U.S. Symposium on Rock Mechanics, Tucson, Arizona, ARMA-87-1213.

Gangi AF (1978) Variation of whole and fractured porous rock permeability with confining pressure. Int J Rock Mech Min Sci Geomech Abstr 15(5):249–257. https://doi.org/10.1016/0148-9062(78)90957-9

Gentier S, Lamontagne E, Archambault G, Riss J (1997) Anisotropy of flow in a fracture undergoing shear and its relationship to the direction of shearing and injection pressure. Int J Rock Mech Min Sci 34(3–4):94.e1-94.e12. https://doi.org/10.1016/S1365-1609(97)00085-3

Glover PWJ, Matsuki K, Hikima R, Hayashi K (1997) Fluid flow in fractally rough synthetic fractures. Geophys Res Lett 24(14):1803–1806. https://doi.org/10.1029/97GL01670

Golfier F, Zarcone C, Bazin B, Lenormand R, Lasseux D, Quintard M (2002) On the ability of a Darcy-scale model to capture wormhole formation during the dissolution of a porous media. J Fluid

Mech 457:213–254. https://doi.org/10.1017/S0022112002007735

Grasselli G (2001) Shear Strength of Rock Joints Based on Quantified Surface Description. Dissertation, Ecole Polytechnique Federale de Lausanne

Grasselli G, Wirth J, Egger P (2002) Quantitative three-dimensional description of a rough surface and parameter evolution with shearing. Int J Rock Mech Min Sci 39(6):789–800. https://doi.org/10.1016/S1365-1609(02)00070-9

Greenwood JA, Williamson JBP, Bowden FP (1966) Contact of nominally flat surfaces. Proc R Soc Lond Ser A Math Phys Sci 295(1442):300–319. https://doi.org/10.1098/rspa.1966.0242

Gutierrez M, Øino LE, Nygård R (2000) Stress-dependent permeability of a de-mineralised fracture in shale. Mar Pet Geol 17(8):895–907. https://doi.org/10.1016/S0264-8172(00)00027-1

Hakami E, Larsson E (1996) Aperture Measurements and Flow Experiments on a Single Natural Fracture. Int J Rock Mech Min Sci 33(4):395–404. https://doi.org/10.1016/0148-9062(95)00070-4

Hopkins DL, Cook NGW, Myer L (1987) Fracture stiffness and aperture as a function of applied stress and contact geometry. In: Farmer IW, Daemen JJ, Desai CS, Glass CE, Neuman SP (eds) Rock Mechanics: Proceedings of the 28th U.S. Symposium, CRC Press, Tucson, pp 673–680

Indraratna B, Ranjith PG, Gale W (1999) Single phase water flow through rock fractures. Geotech Geol Eng 17(3):211–240. https://doi.org/10.1023/a:1008922417511

Inoue J, Sugita H (2003) Fourth-order approximation of fluid flow through rough-walled rock fracture. Water Resour Res. https://doi.org/10.1029/2002WR001411

Iwano M, Einstein HH (1995) Laboratory experiments on geometric and hydromechanical characteristics of three different fractures in granodiorite. In: Proceedings of the 8th ISRM Congress, Tokyo, Japan. ISRM-8CONGRESS-1995-151

Jacobs TDB, Junge T, Pastewka L (2017) Quantitative characterization of surface topography using spectral analysis. Surf Topogr Metrol Prop. https://doi.org/10.1088/2051-672X/aa51f8

Jang J, Narsilio GA, Santamarina JC (2011) Hydraulic conductivity in spatially varying media—a pore-scale investigation. Geophys J Int 184(3):1167–1179. https://doi.org/10.1111/j.1365-246X.2010.04893.x

Katz AJ, Thompson AH (1985) Fractal sandstone pores: implications for conductivity and pore formation. Phys Rev Lett 54(12):1325–1328. https://doi.org/10.1103/PhysRevLett.54.1325

Keller A (1998) High resolution, non-destructive measurement and characterization of fracture apertures. Int J Rock Mech Min Sci 35(8):1037–1050. https://doi.org/10.1016/S0148-9062(98)00164-8

Kim S, Santamarina JC (2016) Geometry-coupled reactive fluid transport at the fracture scale: application to CO2 geologic storage. Geofluids 16(2):329–341. https://doi.org/10.1111/gfl.12152

Kling T, Vogler D, Pastewka L, Amann F, Blum P (2018) Numerical simulations and validation of contact mechanics in a granodiorite fracture. Rock Mech Rock Eng 51(9):2805–2824. https://doi.org/10.1007/s00603-018-1498-x

Lanaro F (2000) A random field model for surface roughness and aperture of rock fractures. Int J Rock Mech Min Sci 37:1195–1210. https://doi.org/10.1016/S1365-1609(00)00052-6

Leach R (2011) Optical measurement of surface topography. Springer, Berlin, Heidelberg. https://doi.org/10.1007/978-3-642-12012-1

Lee JJ, Bruhn RL (1996) Structural anisotropy of normal fault surfaces. J Struct Geol 18(8):1043–1059. https://doi.org/10.1016/0191-8141(96)00022-3

Lee HS, Cho TF (2002) Hydraulic characteristics of rough fractures in linear flow under normal and shear load. Rock Mech Rock Eng 35(4):299–318. https://doi.org/10.1007/s00603-002-0028-y

Li B, Jiang Y, Koyama T, Jing L, Tanabashi Y (2008) Experimental study of the hydro-mechanical behavior of rock joints using a parallel-plate model containing contact areas and artificial fractures. Int J Rock Mech Min Sci 45(3):362–375. https://doi.org/10.1016/j.ijrmms.2007.06.004

Li B, Zhao Z, Jiang Y, Jing L (2015) Contact mechanism of a rock fracture subjected to normal loading and its impact on fast closure behavior during initial stage of fluid flow experiment. Int J Numer Anal Meth Geomech 39(13):1431–1449. https://doi.org/10.1002/nag.2365

Lomize GM (1951) Flow in fractured rocks (in russian). Gosenergoizdat, Moscow, p 127

Magsipoc E, Zhao Q, Grasselli G (2020) 2D and 3D roughness characterization. Rock Mech Rock Eng 53:1495–1519. https://doi.org/10.1007/s00603-019-01977-4

Majumdar A, Bhushan B (1990) Role of fractal geometry in roughness characterization and contact mechanics of surfaces. J Tribol 112(2):205–216. https://doi.org/10.1115/1.2920243

Makurat A, Barton N, Rad NS, Bandis S (1990) Joint conductivity variation due to normal and shear deformation. In: Barton N, Stephansson O (eds) Proceedings of the International Symposium on Rock Joints, A.A. Balkema, Rotterdam, pp 535–540

Mandelbrot BB, Passoja DE, Paullay AJ (1984) Fractal character of fracture surfaces of metals. Nature 308:721–722. https://doi.org/10.1038/308721a0

Matsuki K, Chida Y, Sakaguchi K, Glover PWJ (2006) Size effect on aperture and permeability of a fracture as estimated in large synthetic fractures. Int J Rock Mech Min Sci 43(5):726–755. https://doi.org/10.1016/j.ijrmms.2005.12.001

Matsuki K, Kimura Y, Sakaguchi K, Kizaki A, Giwelli A (2010) Effect of shear displacement on the hydraulic conductivity of a fracture. Int J Rock Mech Min Sci 47(3):436–449. https://doi.org/10.1016/j.ijrmms.2009.10.002

Nemoto K, Watanabe N, Hirano N, Tsuchiya N (2009) Direct measurement of contact area and stress dependence of anisotropic flow through rock fracture with heterogeneous aperture distribution. Earth Planet Sci Lett 281(1):81–87. https://doi.org/10.1016/j.epsl.2009.02.005

Nguyen TS, Selvadurai APS (1998) A model for coupled mechanical and hydraulic behavior of a rock joint. Int J Numer Anal Meth Geomech 22(1):29–48. https://doi.org/10.1002/(SICI)1096-9853(199801)22:1%3c29::AID-NAG907%3e3.0.CO;2-N

Nishiyama S, Ohnishi Y, Ito H, Yano T (2014) Mechanical and hydraulic behavior of a rock fracture under shear deformation. Earth Planets Space 66(1):108. https://doi.org/10.1186/1880-5981-66-108

Odling NE (1994) Natural fracture profiles, fractal dimension and joint roughness coefficients. Rock Mech Rock Eng 27(3):135–153. https://doi.org/10.1007/bf01020307

Ogilvie SR, Isakov E, Glover PWJ (2006) Fluid flow through rough fractures in rocks. II: a new matching model for rough rock fractures. Earth Planet Sci Lett 241(3):454–465. https://doi.org/10.1016/j.epsl.2005.11.041

Olsson WA (1992) The effect of slip on the flow of fluid through a fracture. Geophys Res Lett 19(6):541–543. https://doi.org/10.1029/92GL00197

Olsson R, Barton N (2001) An improved model for hydromechanical coupling during shearing of rock joints. Int J Rock Mech Min Sci 38(3):317–329. https://doi.org/10.1016/S1365-1609(00)00079-4

Oron AP, Berkowitz B (1998) Flow in rock fractures: the local cubic law assumption reexamined. Water Resour Res 34(11):2811–2825. https://doi.org/10.1029/98WR02285

Patir N, Cheng H (1978) An average flow model for determining effects of three-dimensional roughness on partial hydrodynamic lubrication. J Lubr Technol 100(1):12–17. https://doi.org/10.1115/1.3453103

Patton FD (1966) Multiple modes of shear failure in rock. In: Proceedings of the 1st Congress International Society of Rock Mechanics, Lisbon, Portugal, 25 September, pp 509–513

Plesha ME (1987) Constitutive models for rock discontinuities with dilatancy and surface degradation. Int J Numer Anal Meth Geomech 11(4):345–362. https://doi.org/10.1002/nag.1610110404

Plummer L, Wigley T, Parkhurst D (1978) The kinetics of calcite dissolution in CO 2-water systems at 5 degrees to 60 degrees C and 0.0 to 1.0 atm CO 2. Am J Sci 278(2):179–216. https://doi.org/10.2475/ajs.278.2.179

Power WL, Durham WB (1997) Topography of natural and artificial fractures in granitic rocks: implications for studies of rock friction and fluid migration. Int J Rock Mech Min Sci 34(6):979–989. https://doi.org/10.1016/S1365-1609(97)80007-X

Power WL, Tullis TE (1991) Euclidean and fractal models for the description of rock surface roughness. J Geophys Res 96(B1):415–424. https://doi.org/10.1029/90JB02107

Pyrak-Nolte LJ, Morris JP (2000) Single fractures under normal stress: the relation between fracture specific stiffness and fluid flow. Int J Rock Mech Min Sci 37(1):245–262. https://doi.org/10.1016/S1365-1609(99)00104-5

Pyrak-Nolte LJ, Nolte DD (2016) Approaching a universal scaling relationship between fracture stiffness and fluid flow. Nat Commun 7:10663. https://doi.org/10.1038/ncomms10663

Pyrak-Nolte LJ, Myer LR, Cook NGW, Witherspoon PA (1987) Hydraulic and mechanical properties of natural fractures in low permeability rock. In: Herget G, Vongpaisal S (eds) Proceedings of the 6th ISRM Congress, A.A. Balkema, Rotterdam, pp 225–231

Raven KG, Gale JE (1985) Water flow in a natural rock fracture as a function of stress and sample size. Int J Rock Mech Min Sci Geomech Abstr 22(4):251–261. https://doi.org/10.1016/0148-9062(85)92952-3

Rutqvist J, Wu YS, Tsang CF, Bodvarsson G (2002) A modeling approach for analysis of coupled multiphase fluid flow, heat transfer, and deformation in fractured porous rock. Int J Rock Mech Min Sci 39(4):429–442. https://doi.org/10.1016/S1365-1609(02)00022-9

Saeb S, Amadei B (1992) Modelling rock joints under shear and normal loading. Int J Rock Mech Min Sci Geomech Abstr 29(3):267–278. https://doi.org/10.1016/0148-9062(92)93660-C

Sayles RS, Thomas TR (1978) Surface topography as a nonstationary random process. Nature 271(5644):431–434. https://doi.org/10.1038/271431a0

Sharifzadeh M, Mitani Y, Esaki T (2008) Rock joint surfaces measurement and analysis of aperture distribution under different normal and shear loading using GIS. Rock Mech Rock Eng 41(2):299–323. https://doi.org/10.1007/s00603-006-0115-6

Shin H, Santamarina JC (2019) An implicit joint-continuum model for the hydro-mechanical analysis of fractured rock masses. Int J Rock Mech Min Sci 119:140–148. https://doi.org/10.1016/j.ijrmms.2019.04.006

Souley M, Lopez P, Boulon M, Thoraval A (2015) Experimental hydromechanical characterization and numerical modelling of a fractured and porous sandstone. Rock Mech Rock Eng 48(3):1143–1161. https://doi.org/10.1007/s00603-014-0626-5

ASTM Standard D7012-14e1 (2014) Compressive strength and elastic moduli of intact rock core specimens under varying states of stress and temperatures. ASTM International, West Conshohocken. https://doi.org/10.1520/D7012-14E01

Swan G (1983) Determination of stiffness and other joint properties from roughness measurements. Rock Mech Rock Eng 16(1):19–38. https://doi.org/10.1007/bf01030216

Tarolli P (2014) High-resolution topography for understanding earth surface processes: opportunities and challenges. Geomorphology 216:295–312. https://doi.org/10.1016/j.geomorph.2014.03.008

Taron J, Elsworth D, Min KB (2009) Numerical simulation of thermal-hydrologic-mechanical-chemical processes in deformable, fractured porous media. Int J Rock Mech Min Sci 46(5):842–854. https://doi.org/10.1016/j.ijrmms.2009.01.008

Teufel LW (1987) Permeability changes during shear deformation of fractured rock. In: Farmer IW, Daemen JJ, Desai CS, Glass CE, Neuman SP (eds) Rock Mechanics: Proceedings of the 28th U.S. Symposium, CRC Press, Tucson, pp 473–480

Tezuka K, Tamagawa T, Watanabe K (2005) Numerical Simulation of Hydraulic Shearing in Fractured Reservoir. In: Horne R, Okandan E (eds) Proceedings of the World Geothermal Congress 2005, International Geothermal Association, Antalya

Thomas TR (1998) Rough Surfaces. Imperial College Press, London

Tsang YW, Witherspoon PA (1981) Hydromechanical behavior of a deformable rock fracture subject to normal stress. J Geophys Res Solid Earth 86(B10):9287–9298. https://doi.org/10.1029/JB086iB10p09287

Tuncay E, Hasancebi N (2009) The effect of length to diameter ratio of test specimens on the uniaxial compressive strength of rock. Bull Eng Geol Env 68(4):491–497. https://doi.org/10.1007/s10064-009-0227-9

Vogler D, Settgast RR, Annavarapu C, Madonna C, Bayer P, Amann F (2018) Experiments and simulations of fully hydro-mechanically coupled response of rough fractures exposed to high-pressure fluid injection. J Geophys Res Solid Earth 123(2):1186–1200. https://doi.org/10.1002/2017jb015057

Walsh JB (1981) Effect of pore pressure and confining pressure on fracture permeability. Int J Rock Mech Min Sci Geomech Abstr 18(5):429–435. https://doi.org/10.1016/0148-9062(81)90006-1

Walsh R, McDermott C, Kolditz O (2008) Numerical modeling of stress-permeability coupling in rough fractures. Hydrogeol J 16(4):613–627. https://doi.org/10.1007/s10040-007-0254-1

Watanabe N, Hirano N, Tsuchiya N (2008) Determination of aperture structure and fluid flow in a rock fracture by high-resolution numerical modeling on the basis of a flow-through experiment under confining pressure. Water Resour Res. https://doi.org/10.1029/2006wr005411

Wilbur C, Amadei B (1990) Flow pump measurements of fracture transmissivity as a function of normal stress. In: Hustrulid WA, Johnson GA (eds) Rock mechanics contributions and challenges: Proceedings of the 31st U.S. Symposium, CRC Press, London, pp 621–627

Witherspoon PA, Wang JSY, Iwai K, Gale JE (1980) Validity of Cubic Law for fluid flow in a deformable rock fracture. Water Resour Res 16(6):1016–1024. https://doi.org/10.1029/WR016i006p01016

Xiong F, Jiang Q, Chen M (2018) Numerical investigation on hydraulic properties of artificial-splitting granite fractures during normal and shear deformations. Geofluids. https://doi.org/10.1155/2018/9036028 (**Article ID 9036028**)

Yeo IW, de Freitas MH, Zimmerman RW (1998) Effect of shear displacement on the aperture and permeability of a rock fracture. Int J Rock Mech Min Sci 35(8):1051–1070. https://doi.org/10.1016/S0148-9062(98)00165-X

Zhao J (1997) Joint surface matching and shear strength part A: joint matching coefficient (JMC). Int J Rock Mech Min Sci 34(2):173–178. https://doi.org/10.1016/S0148-9062(96)00062-9

Zhou H, Abdelaziz A, Grasselli G (2018) Rock dilation and its effect on fracture transmissivity. Proceedings of the

Unconventional Resources Technology Conference, Houston, Texas. URTEC-2903018-MS

Zimmerman RW, Bodvarsson GS (1996) Hydraulic conductivity of rock fractures. Transp Porous Media 23(1):1–30. https://doi.org/10.1007/bf00145263

Carbonate rocks: Matrix permeability estimation

Alejandro Cardona and J. Carlos Santamarina

ABSTRACT

Carbonate rocks store half of the world's proven oil reserves. Genesis and postdepositional diagenetic processes define the porous network topology and the matrix permeability. This study compiles a database of porosity, specific surface, mercury porosimetry, and permeability values extracted from published sources and complements the database through a focused experimental study. Specific surface and porosity combine to estimate the pore size (D_{sur}). Permeability versus D_{sur} data cluster along a single trend with a slope of 2 in a log–log scale, which is in agreement with the Kozeny–Carman model. Discordant data points correspond to samples with dual porosity or broad pore-size distributions with long tails, where flow channels along larger interconnected pores. Indeed, the detailed analysis of all the porosimetry data in the database shows that permeability correlates best with the pore size D80, that is, the 80th percentile in pore-size distributions. Once again, the best fit is a power function in terms of $(D80)^2$, analogous to Kozeny–Carman. The prediction uncertainty using D80 is one order of magnitude and has the same degree of uncertainty as more complex models and analyses. This observation suggests an irreducible uncertainty of one order of magnitude in permeability estimation from index properties such as porosity, mercury porosimetry, and specific surface probably resulting from specimen preparation effects, inherent physical differences in permeation versus invasion, and difficulties in data interpretation. These estimates of permeability are most valuable when specimens are limited to small sizes, such as cuttings.

INTRODUCTION

The world energy demand has steadily increased during the last century, with an additional 30% increase in demand predicted

---

Manuscript received September 16, 2017; provisional acceptance October 31, 2017; revised manuscript received March 18, 2018; revised manuscript provisional acceptance April 26, 2018; 2nd revised manuscript received July 8, 2018; 2nd revised manuscript provisional acceptance October 29, 2018; 3rd revised manuscript received January 14, 2019; 3rd revised manuscript provisional acceptance January 30, 2019; 4th revised manuscript received February 19, 2019; final acceptance May 2, 2019.
DOI:10.1306/05021917345

AUTHORS

ALEJANDRO CARDONA ~ *Energy Resources and Petroleum Engineering, King Abdullah University of Science and Technology (KAUST), Thuwal, Saudi Arabia; alejandro.cardonaramirez@kaust.edu.sa*

Alejandro Cardona received his M.Sc. from KAUST and his B.S. from the Universidad Nacional de Colombia. He is currently pursuing his doctoral studies in energy resources and petroleum engineering at KAUST. His research focuses on the understanding of flow-related phenomena in porous media with an emphasis on fractured carbonate rocks.

J. CARLOS SANTAMARINA ~ *Energy Resources and Petroleum Engineering, KAUST, Thuwal, Saudi Arabia; carlos.santamarina@kaust.edu.sa*

Juan Carlos Santamarina received his Ph.D. from Purdue University, his M.Sc. from the University of Maryland, and his CE from Universidad Nacional de Córdoba Argentina. He explores the foundations of subsurface processes using particle- and pore-scale testing methods combined with high-resolution geophysical process monitoring systems and inversion techniques. The combined experimental-numerical framework supports developments in the field of energy geotechnology, with contributions to resource recovery as well as energy and waste geostorage.

ACKNOWLEDGMENTS

Support for this research was provided by the King Abdullah University of Science and Technology Endowment. G. E. Abelskamp edited the manuscript.

DATASHARE 115

Table S1 is available in an electronic version on the AAPG website (www.aapg.org/datashare) as Datashare 115.

by the year 2040 (BP, 2018). Fossil fuels satisfy 81% of the current global energy consumption (International Energy Agency, 2018). Although its share of the total consumption will decrease to 75% by the midcentury, the actual consumption of nonrenewable sources will continue to increase. Hydrocarbons comprise half of the global energy mix (International Energy Agency, 2015).

The rock porosity and permeability determine the quality of hydrocarbon reservoirs: porosity implies storage capacity, whereas permeability is needed for flow and recovery (Dullien, 1992; Tiab and Donaldson, 2012). Natural and induced fractures control the overall flow in carbonate reservoirs (Van Golf-Racht, 1996; Gale et al., 2004; Ortega et al., 2010); however, the rate at which stored hydrocarbons exit the matrix into fractures depends on the matrix permeability.

Permeability relates the average flow velocity to the driving total energy gradient. The flow velocity for Newtonian fluids in laminar flow through cylindrical tubes is proportional to the square of the tube diameter (Hagen–Poiseuille equation). The Kozeny–Carman model considers the porous medium as a set of parallel cylindrical tubes and uses the Hagen–Poiseuille equation to compute the effective flow velocity (Kozeny, 1927; Carman, 1997). Then, the resulting permeability k (m^2) is proportional to the square of the pore diameter D (m) and the porosity of the porous medium ϕ (m^3/m^3):

$$k = \frac{\phi}{32\tau^2} D^2 \tag{1}$$

where τ (m/m) is the tortuosity. However, pore size is not constant, and the largest interconnected pores are responsible for most of the flow. This is confirmed by network model studies of flow behavior at the pore scale, which show the coupling between pore size, spatial variability, and connectivity on flow patterns (Jang et al., 2011). Semiempirical factors added to the Kozeny–Carman equation attempt to take these processes into consideration, often through a generic tortuosity factor (equation 1).

Carbonate rocks store half of the world's proven oil reserves (US Energy Information Administration, 2015). Genesis and postdepositional diagenetic processes define the pore structure in carbonate rocks (Moore and Wade, 2013). The intraparticle porosity, high friability, and chemical reactivity of carbonate sediments affect their evolution during burial (Croizé et al., 2013; Moore and Wade, 2013) and leads to features such as dual and occluded porosity (Figure 1; see also Saner and Sahin, 1999; Poursoltani and Gibling, 2011). Experimental data show that the pore size in carbonates varies by more than 6 orders of magnitude (Nelson, 2009), whereas the permeability varies by approximately 10 orders

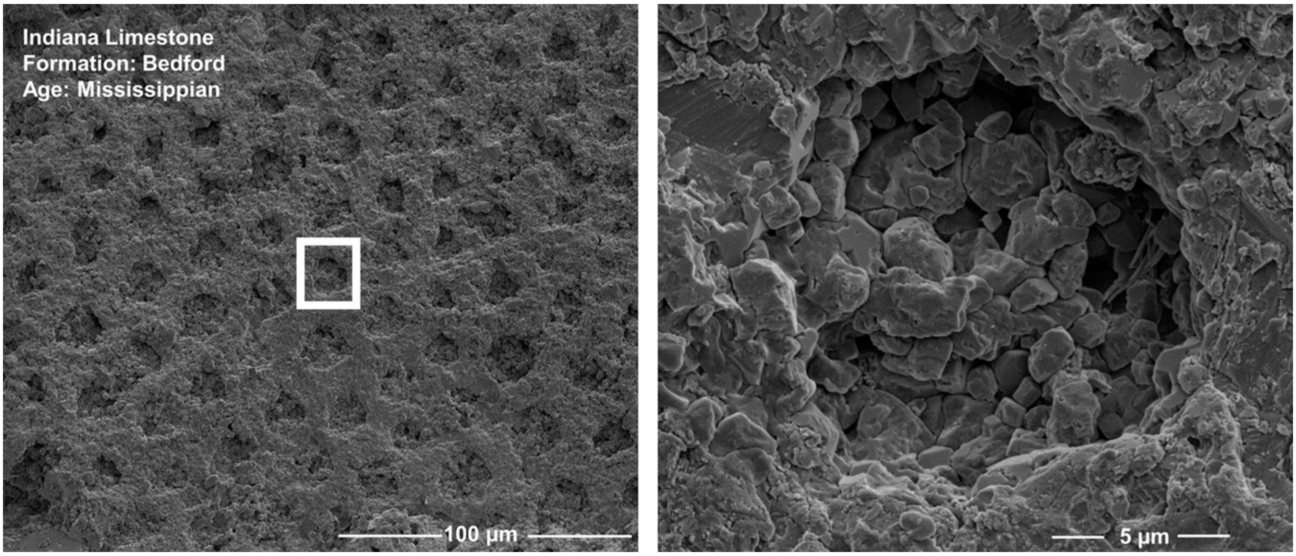

Figure 1. Scanning electron microscope image of an Indiana carbonate sample. The image confirms the presence of approximately 15 μm pores in agreement with mercury intrusion data. The zoomed-in picture on the right (corresponding to the white square on the left image) illustrates the submicron pore topology.

of magnitude (Nelson, 1994), which is in overall agreement with the power-2 dependency anticipated by equation 1.

The purpose of this study is to enhance the understanding of carbonate permeability using a physics-inspired yet data-driven approach. The following section describes the database compiled for this study.

DATABASE: CHARACTERIZATION AND POTENTIAL PITFALLS

This study compiles a database of permeability values extracted from published sources for carbonate rocks in the United States, Russia, the Middle East, and Europe (data sources are Brooks and Purcell, 1952; Chilingarian et al., 1990; Lucia, 1995; Mortensen et al., 1998; Lindsay et al., 2006; Fabricius et al., 2007; Clerke, 2009; Alam et al., 2011; Vincent et al., 2011). The 286 entries include mostly binary data in terms of permeability, rock formation, porosity, specific surface, and/or pore-size distribution (see Table S1, supplementary material available as AAPG Datashare 115 at www.aapg.org/datashare). Permeability and specific surface data span several orders of magnitude. Although data sources use similar measurement methods (gas adsorption for specific surface and helium expansion for porosity), differences in test protocols, devices, and data analyses add variability to the data set.

Only 13 entries have all 3, that of porosity, pore-size distribution, and specific surface (Paris Basin in Vincent et al., 2011). This research conducts a focused experimental study designed to extend this data set using 11 commercially available carbonates cores (Kocurek Industries), some with multimodal pore-size distributions (refer to Table 1). Test details and potential pitfalls follow.

Porosity

Weight change upon liquid saturation provides the accessible porosity (American Petroleum Institute, 1998). The saturation procedure involved five steps: (1) vacuum, (2) CO_2 injection cycles used to replace the residual air inside the specimen, (3) vacuum, (4) injection of deaired-deionized water into the vessel, and (5) several vacuum–pressure cycles. The specimen dry weight W_{dry} (g) and saturated weight W_{sat} (g) combine to determine the porosity ϕ using the mineral specific gravity G_s:

$$\phi = \frac{(W_{sat} - W_{dry})G_s}{W_{dry} + (W_{sat} - W_{dry})G_s} \tag{2}$$

Measured porosities range between $\phi = 0.11$ and $\phi = 0.53$ (Table 1).

Specific Surface

Several liquid- and gas-based methods were tested to determine specific surface. Whereas liquid adsorption measurements rely on gravimetric changes after lengthy equilibration times (Cerato and Lutenegger, 2002), gas adsorption with krypton emerged as the most adequate characterization procedure given the relatively low specific surface area of carbonates (Micromeritics accelerated surface area and porosimetry system 2420 in Beebe et al., 1945). The measured specific surface areas S_s range from 0.5 to 1.3 m^2/g (2441–6347 ft^2/lb). This coincides with reported values for carbonate rocks (Chilingarian et al., 1990; Vincent et al., 2011).

Tests were conducted with carbonates crushed to two different sizes. Results summarized in Table 1 show that the measured specific surface depends on crushed particle size although the external surface area is negligible in all cases (e.g., the external surface is 0.03 m^2/g [146 ft^2/lb] for 70-μm grains). This suggests that sample crushing gives access to occluded porosity and creates new gas pathways (calibration tests showed equipment variability of <4%).

Pore-Size Distribution

Mercury intrusion porosimetry (MIP) measures the volume of mercury that invades the specimen as a function of pressure (Giesche, 2006). Mercury invades along percolating paths, and occluded porosity remains untested. The Young–Laplace equation relates the measured pressure to pore-throat size (León y León, 1998), whereas injected volumes correspond to pore bodies. Consequently, large pores may be

Table 1. Carbonate Formations Tested in This Study

					Specific Surface, m^2/g (ft^2/lb)	Specific Surface, m^2/g (ft^2/lb)	
Sample	Location	Formation	Age	Porosity	$D < 74$ μm	150 μm $> D >$ 74 μm	Permeability, md
Austin Chalk	Central–southcentral Texas[*]	Austin Chalk[*]	Late Cretaceous[*]	0.28	0.93 (4541)	0.60 (2929)	2.1
Desert Pink	Garden City, Texas	–	Early Cretaceous	0.30	0.49 (2392)	0.61 (2978)	9.6
Edwards White	Edwards Plateau, Texas	Edwards[†]	Early Cretaceous	0.13	0.85 (4150)	0.66 (3222)	0.1
Edwards Yellow	Garden City, Texas	Edwards[†]	Early Cretaceous	0.29	0.57 (2783)	0.59 (2881)	27
Indiana 2–4	Oolitic, Indiana	Bedford[‡]	Mississippian	0.15	0.83 (4052)	–	0.9
Indiana 60	Oolitic, Indiana	Bedford[‡]	Mississippian	0.17	1.09 (5322)	0.84 (4101)	21
Indiana 70	Oolitic, Indiana	Bedford[‡]	Mississippian	0.16	1.24 (6054)	0.91 (4443)	220
Indiana 200	Oolitic, Indiana	Bedford[‡]	Mississippian	0.13	0.72 (3515)	1.13 (5517)	73
Mount Gambier	Southeast, Australia[§]	Whalers Bluff [§]	Pliocene[§]	0.53	1.17 (5712)	0.51 (2490)	4636
Silurian Dolomite	Thornton, Illinois	Racine[¶]	Silurian	0.11	0.84 (4101)	0.39 (1904)	1.9
Winterset	Redfield, Kansas	Dennis[#]	Missourian[#]	0.27	0.54 (2636)	0.80 (3906)	35

Abbreviations: – = no data; D = pore diameter.

[*] Corbett et al. (1987).

[†] Fisher and Rodda (1969).

[‡] Churcher et al. (1991).

[§] Kyser et al. (1998).

[¶] Weiner and Koster Van Groos (1976).

[#] Railsback (1993).

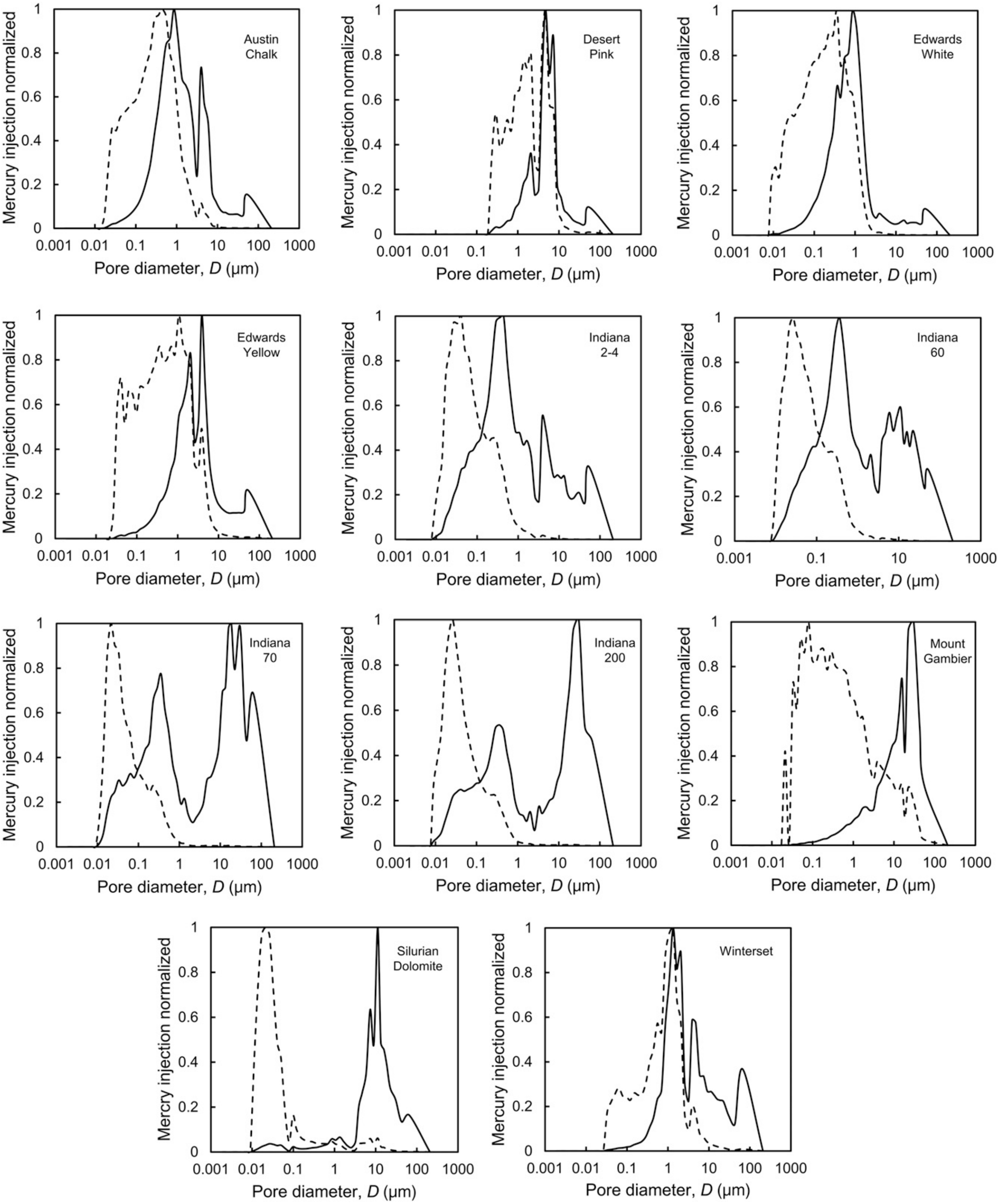

Figure 2. Normalized pore-size distributions obtained from mercury porosimetry. The black solid lines show the logarithmic differential intrusion, and the black dashed lines correspond to the probability density function.

assigned to small pore throats (i.e., the ink-bottle effect) (Diamond, 2000; Moro and Böhni, 2002).

Pore-size distributions obtained from mercury injection porosimetry tests are commonly presented in terms of pressure P (Pa) and the logarithm of the differential intrusion $g(D)$ for a given saturation S (m^3/m^3):

$$g(D) = \frac{dS}{d(lnP)} = P\frac{dS}{dP} \tag{3}$$

This definition emphasizes dual porosity systems and amplifies the contribution of large pores. However, the physical pore-size density function $f(D)$ relates pressure to capillarity in terms of the surface tension γ (N/m [lbf/ft]) and the contact angle θ (rad) (Lenormand, 2003):

$$f(D) = \frac{P^2}{2\gamma\ cos\theta}\frac{dS}{dP} = \frac{P}{2\gamma\ cos\theta}g(D) = \frac{2}{D}g(D) \tag{4}$$

Therefore, the commonly used distribution $g(D)$ has a pore-size–dependent amplification of the true pore-size distribution $g(D) = D \times f(D)/2$. Figure 2 shows the pore-size distributions $g(D)$ and $f(D)$ obtained for the 11 specimens tested in this study. The estimated mean pore sizes computed from $g(D)$ are significantly smaller than the mean pore sizes obtained from $f(D)$. These results highlight profound differences in the potential interpretation of these data.

Permeability

The permeability of all 11 specimens was measured using a gas permeameter (MetaRock Laboratories SSK-300). The ends remained unpolished to avoid fines clogging near the inlet face of the cylindrical specimens (diameter was 25 mm [1 in.] and length was 50 mm [2 in.]), and limited pressure gradients prevented nonlinear effects. Values of N_2 permeability measured at different mean pressures were used to correct for Klinkenberg's effect. Table 1 includes the measured permeability values.

DATA ANALYSES

Porosity and Carbonate Classification

Empirical models for carbonate permeability focus on porosity as a predictive parameter (Jennings and Lucia, 2003; Babadagli and Al-Salmi, 2004; Lucia, 2007). The inherent limitation in empirical models that are based exclusively on porosity is highlighted by the contrast between the very narrow range in porosity (e.g., $0.1 < \phi < 0.6$) versus the 10 orders of magnitude in the permeability range (Nelson, 1994).

Additional information can be included, such as carbonate classification in terms of textural features and particle size, because these features provide

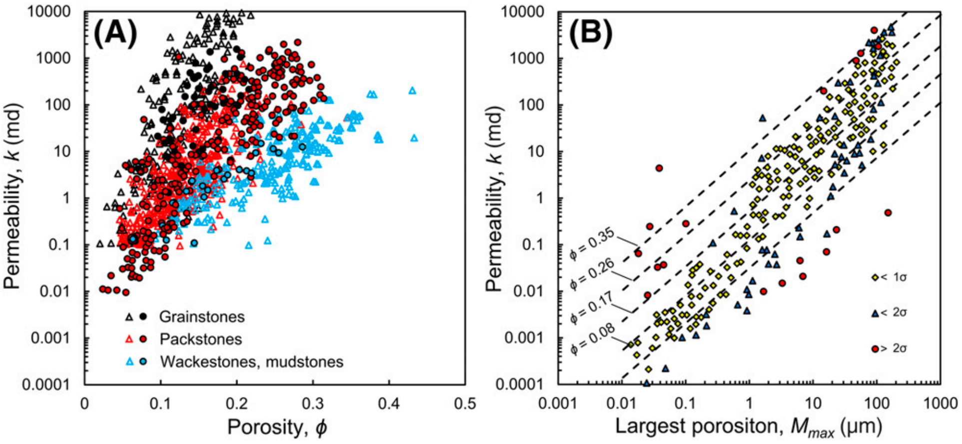

Figure 3. Empirical models for carbonate permeability. (A) Permeability as a function of porosity ϕ and carbonate type (data from Lucia, 1995 and Lindsay et al., 2006; for comparison, the original classification used by Lindsay et al., 2006 is mapped onto the classification from Lucia, 1995). Color coding identifies rock type; triangles correspond to data from Lucia, 1995 and filled circles are data from Lindsay et al., 2006. (B) Permeability as a function of the largest porositon size M_{max} measured using mercury porosimetry (after Clerke, 2009); dashed lines correspond to isoporosity values in the model (refer to equation 6). Data points are colored to reflect the distance between the model predictions and measured values in terms of standard deviation σ.

information about genesis and ensuing pore topology (Pemberton and Gingras, 2005; Boggs, 2009; Uddin et al., 2017).

The classification in Dunham (1962) distinguishes (1) coarse-grained dominant carbonates (grainstones being dolograinstones and large crystalline grainstones), (2) carbonates with a coarse-grained structure but with fines in pores (packstones), and (3) fines-dominant carbonates (wackestone, mudstone, and fine crystalline limestones and dolostones). Then, the empirical permeability–porosity power model (Lucia, 1995)

$$k = a\,\phi^b \tag{5}$$

relates the *a* factor and *b* exponent to carbonate rock type. Figure 3A superimposes two data sets for nonvuggy carbonate reservoirs in the United States and in the Middle East (Lucia, 1995; Lindsay et al., 2006). The model in Lucia (1995) highlights the importance of rock type and the impact of fines or "mud" on pore networks and permeability, yet predictions have more than one order of magnitude in uncertainty, which is in part because of potential differences in pore structure (see thin-section–based analyses in Weger et al., 2009).

Porosity, Pore-Size Distribution, and Pore Structure

Other models relate permeability to pore-size distributions inferred from mercury porosimetry (Swanson, 1981; Katz and Thompson, 1986; Glover et al., 2006; Rezaee et al., 2006; Gao and Hu, 2013). Data analyses reveal that the largest modal element or "porositon" M_{max} (μm) determines the matrix permeability (md) in carbonates with multimodal pore-size distributions (Figure 3B; Clerke et al., 2008; Clerke, 2009):

$$\log(k) = -1.54 + 1.2\log(M_{max}) + 7.3\phi \tag{6}$$

More detailed analyses assume an internal pore structure such as fractal, consider critical path analysis, and/or apply percolation theory (Charlaix et al., 1987; Friedman and Seaton, 1998; Hunt and Gee, 2002; Buiting and Clerke, 2013; Daigle, 2016). For example, Buiting and Clerke (2013) match mercury porosimetry data with one or more Thomeer hyperbolas and extract three parameters: the maximum invaded volume ϕ^*, pressure at first invasion P_d (kPa), and pore geometry factor *G*. Through mathematical analysis, these three parameters combine to predict the rock permeability (assumes tortuosity is at ~2 and fractal dimension is at ~1.56; see resemblance with the earlier empirical models by Swanson, 1981 and Thomeer, 1983):

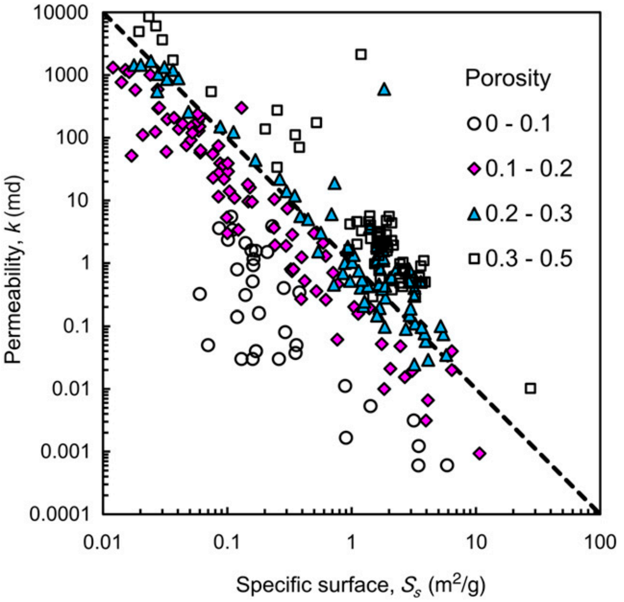

Figure 4. The permeability k versus specific surface S_s for different porosity ranges. The dashed line has a −2 slope in agreement with the Kozeny–Carman equation. The color coding distinguishes data points according to porosity. The data set includes 286 data points. The data sources are Brooks and Purcell (1952), Chilingarian et al. (1990), Mortensen et al. (1998), Fabricius et al. (2007), Alam et al. (2011), and Vincent et al. (2011).

$$k = 24{,}050\,\frac{\phi^*}{(P_d)^2}\,e^{-4.43\sqrt{G}} \tag{7}$$

where permeability is in darcys. The application of models based on pore-size distribution derived from MIP is not straightforward (starting from the interpretation of pore-size distribution data discussed above; equation 4). Although authors tend to highlight model predictability, results obtained as part of this study using these models against the data set show at least one order of magnitude in uncertainty.

Porosity and Specific Surface

Permeability is a measure of the drag that a viscous fluid experiences as it traverses a porous medium. Therefore, the data compilation and the experimental data set include specific surface and porosity. Data

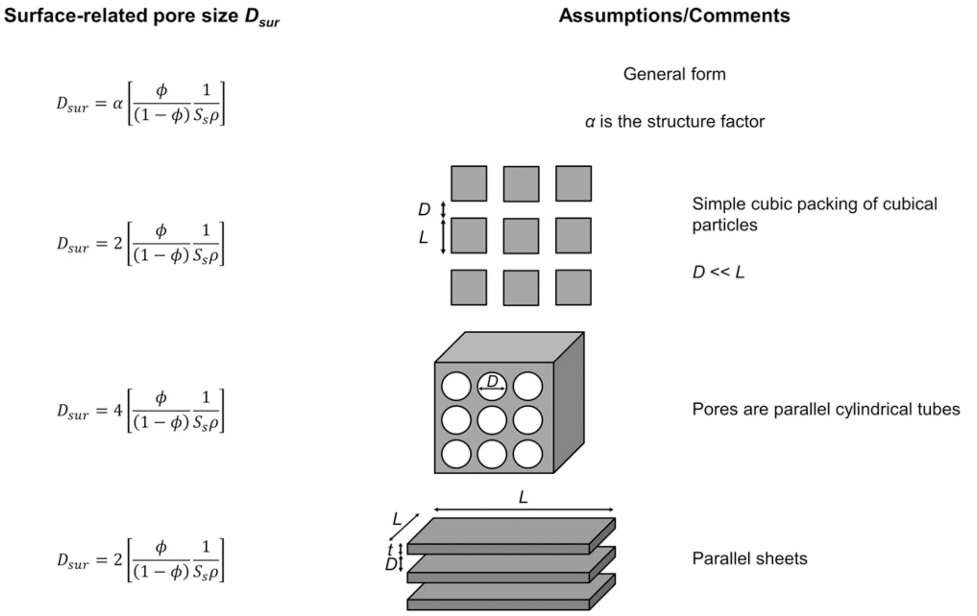

Figure 5. Models to estimate the surface-related pore size D_{sur} for different pore geometries where S_s (m^2/g) is specific surface and ϕ is porosity. ρ = mass density; D = pore diameter; L = largest grain size; t = grain thickness.

reported in terms of the volumetric specific surface S_{vol} (m^2/cm^3) are converted to the gravimetric specific surface S_s (m^2/g) as

$$S_s = \frac{1}{(1-\phi)\rho} S_{vol} \tag{8}$$

where ρ (g/cm^3) is the mass density of solids. Figure 4 illustrates permeability versus specific surface on a log–log scale. Data subsets of equal porosity cluster along lines with a slope of –2 in the log–log plot.

The Kozeny–Carman equation highlights the importance of pore size on permeability (equation 1). The specific surface S_s, porosity ϕ, and mineral mass density ρ combine to estimate the pore size D_{sur} (m) that corresponds to the measured surface area:

$$D_{sur} = \alpha\left[\frac{\phi}{(1-\phi)}\frac{1}{S_s\rho}\right] \tag{9}$$

where the α factor is a function of the fabric and pore topology, as shown in Figure 5. Figure 6 plots permeability values in the database as a function of the pore size estimated with equation 9 for α = 4 (i.e., parallel cylindrical tubes; Figure 5). All data points cluster along a single trend with a slope of 2 in a log–log scale in agreement with the Kozeny–Carman model in equation 1 (see analogous conclusions for a wide range of sediments in Ren and Santamarina, 2018). Most values fall within one order of magnitude of the main trend. The best fit line is

$$k = 5(D_{sur})^2 \tag{10}$$

where D_{sur} is in micrometers and permeability is in millidarcy. This equation allows us to predict permeability from S_s and ϕ values determined from small samples such as cuttings when pores are significantly smaller than the cutting size. In carbonates, the size of cuttings ranges from 1 to 10 mm (0.04–0.4 in.) long depending on drilling conditions (Archie, 1952; Dogruoz et al., 2016); therefore, cuttings are approximately three orders of magnitude larger than pores. However, cuttings impose an inherent bias because they break preferentially along more porous and weaker planes; therefore, predicted permeabilities are lower-bound estimates of the formation permeability.

DISCUSSION

Representative Pore Size

Out-of-trend data points in Figure 6 suggest that the pore size D_{sur} estimated from porosity and specific surface may not be an accurate predictor of the pore size that controls permeability in all cases.

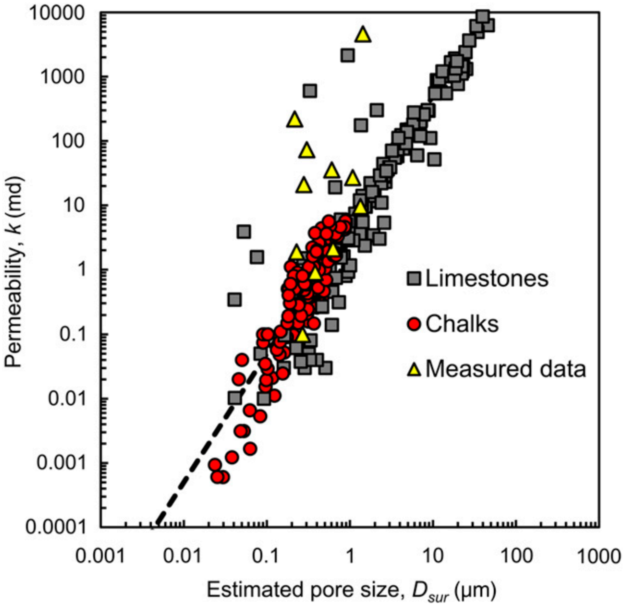

Figure 6. Measured permeability k versus estimated pore size D_{sur} using a model of parallel cylindrical tubes (equation 9). Most of the data collapse onto a narrow trend. The dashed line has a slope value of 2 in agreement with the Kozeny–Carman equation. The data sources are Brooks and Purcell (1952), Chilingarian et al. (1990), Mortensen et al. (1998), Fabricius et al. (2007), Alam et al. (2011), and Vincent et al. (2011). New experimental data gathered in this study are shown as yellow points.

Discordant data points either have clear dual porosity (see the $g(D)$ representation for Indiana 60, Indiana 70, and Indiana 200 in Figure 2) or they exhibit very broad pore-size distributions with long tails (Mount Gambier, Silurian Dolomite, and Winterset specimens in Figure 2).

The representative pore size that is most predictive of permeability is explored in Figure 7 in which the measured permeability values are plotted against selected pore diameter percentiles from $f(D)$ signatures (equation 4) (note that the representative pore size for permeability is equivalent to the concept of critical pore size in other studies; Arns et al., 2005; Nishiyama and Yokoyama, 2017). The data set used for this analysis includes the 11 samples tested in this study plus 13 carbonate samples from the literature (Vincent et al., 2011). The computed square error and visual inspection confirm that the pore size between the 70th and 85th percentiles in porosimetry data provides the most predictive permeability versus pore-size regression (micrometers) for all specimens (data range: 0.1 md $< k <$ 10,000 md):

$$k = 0.2(\mathrm{D80})^{1.75} \approx 0.1(\mathrm{D80})^2 \qquad (11)$$

Although the first equation is the best fit, the second expression has a very similar residual error, and it is quadratic on the particle diameter in agreement with the Kozeny–Carman equation 1. The pore size estimate D_{sur} is less relevant to permeability in the discordant data points because flow channels along the larger interconnected pores (i.e., D80 percentile). Further analyses show that permeability estimates using the D80 pore size have the same degree of uncertainty (i.e., one order of magnitude) as more complex models that assume fractal pore structures, critical path analysis, and percolation theory (methods by Charlaix et al., 1987; Buiting and Clerke, 2013; Daigle, 2016).

Equations 10 and 11 indicate that the representative pore size D80 along the most conductive percolating paths is $\mathrm{D80}/D_{sur} \approx 50$ larger than the pore size inferred from specific surface D_{sur}. The data set confirms the inverse relationship between specific surface and pore size; however, the pore size D_{sur} computed from the specific surface correlates best with the 20th percentile of the pore-size distribution $f(D)$ measured with mercury intrusion.

Anisotropy

Porosity, pore-size distribution, and specific surface do not provide information about anisotropy. Therefore, all models based on these parameters considered permeability to be isotropic (i.e., a scalar). However, permeability is direction dependent (i.e., a tensor). Permeability anisotropy in carbonates originates from inherent sedimentation layering and preferentially aligned features (Dürrast and Siegesmund, 1999; Tipping et al., 2006), biogenic burrows (Pemberton and Gingras, 2005), stress anisotropy (Barton and Quadros, 2014), and ensuing stress-dependent diagenetic processes (Sibson, 1994; Rashid et al., 2015; Toussaint et al., 2018).

Upscaling

Predictions based on MIP depend on the measurement and interpretation of pressure–volume data obtained on small specimens. The assumption of a fractal pore structure provides a convenient framework for upscaling laboratory measurements but only within the validity of the fractal system in the

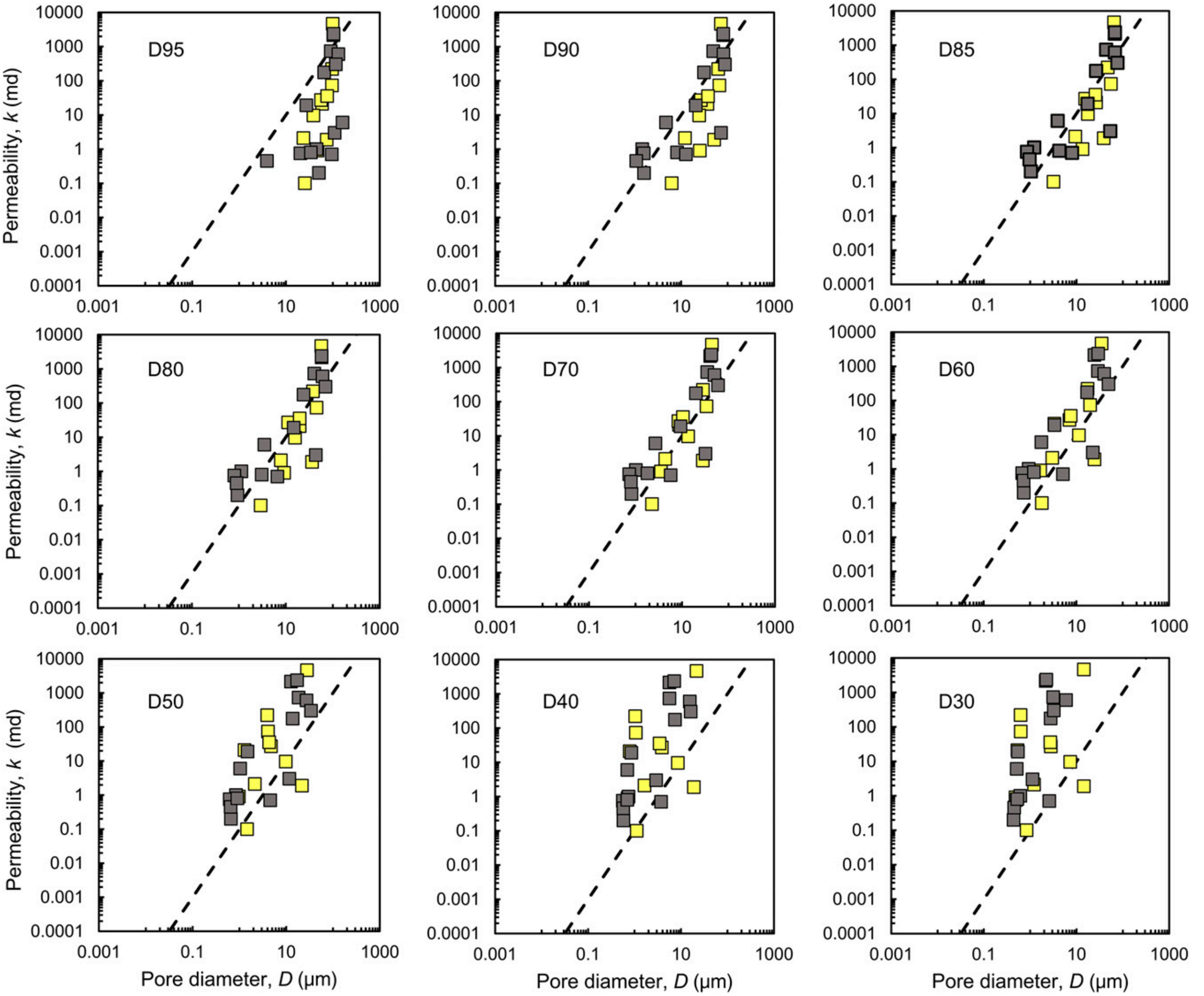

Figure 7. Permeability *k* versus different pore diameter *D* percentiles. The dashed line has a slope value of 2. The 70th to 85th percentiles in pore-size distributions (D70 to D85) provide the best regression with lowest square error with respect to the dashed line. New experimental data gathered in this study are shown as yellow points. Gray points indicate published data (Vincent et al., 2011).

rock matrix (Katz and Thompson, 1985; Pape et al., 1999; Costa, 2006). Stratigraphic features and fractures limit the upscaling size.

Alternatives

Analyses suggest that inherent limitations in the prediction of carbonate permeability from index properties lead to an uncertainty of at least one order of magnitude. Furthermore, porosity, specific surface, and porosimetry are costly measurements. They are most valuable when specimens are limited to small sizes, such as cuttings (Swanson, 1981; Santarelli et al., 1998). However, when cores are available, quick liquid-based measurements of permeability can be less costly. These measurements avoid complex data analysis (as in gas-based measurements) (Wu et al., 1998; Tanikawa and Shimamoto, 2009; Sander et al., 2017) and provide the true value of permeability rather than a correlated estimate; additionally, the test series can readily assess anisotropy and heterogeneity.

CONCLUSIONS

Matrix flow is important even in fractured systems because hydrocarbons stored in the matrix need to migrate to fractures. Carbonate type and formation history define the matrix permeability.

Permeability data plotted against the pore size estimated using porosity and specific surface cluster along a single trend with a slope of 2 (in log–log scale). This result highlights the underlying physics of permeability as captured in the Kozeny–Carman model.

Out-of-trend data points correspond to carbonates with either multimodal or broad pore-size distributions with long tails. In both cases, flow channels along the larger interconnected pores. Permeability correlates best with the pore size D80. This conclusion applies to all carbonates in the database, and it leads to a simple and robust permeability estimator.

More detailed analyses assume an internal pore structure and concepts such as critical path analysis. Their implementation is not straightforward; estimates of permeability using these models result in permeability values with a typical one order of magnitude in uncertainty. This variability is similar to that obtained with other simpler estimators.

All analyses suggest an irreducible uncertainty of one order of magnitude in permeability estimation from index properties such as porosity, porosimetry, and specific surface. This may reflect specimen preparation effects (e.g., crushing size for specific surface measurements or inadequate saturation in porosity determinations), inherent physical differences (permeation of single-phase fluid vs. invasion of an immiscible fluid in MIP), and difficulties in data interpretation (e.g., porosimetry, gas-related corrections in k measurements).

The estimation of permeability based on specific surface and porosity is most valuable when only cuttings are available. When cores are available, simple and quick liquid-based permeability measurements should be sought; they can be less costly than specific surface, porosity, and mercury porosimetry measurements, avoid the inherent uncertainty in correlation-based estimates, and allow the assessment of anisotropy.

REFERENCES CITED

Alam, M. M., I. L. Fabricius, and M. Prasad, 2011, Permeability prediction in chalks: AAPG Bulletin, v. 95, no. 11, p. 1991–2014, doi:10.1306/03011110172.

American Petroleum Institute, 1998, Recommended practices for core analysis, 2nd ed.: Washington, DC, API Publishing Services, 233 p.

Archie, G. E., 1952, Classification of carbonate reservoir rocks and petrophysical considerations: AAPG Bulletin, v. 36, no. 2, p. 278–298.

Arns, C. H., M. A. Knackstedt, and N. S. Martys, 2005, Cross-property correlations and permeability estimation in sandstone: Physical Review E, v. 72, no. 4, p. 046304, doi:10.1103/PhysRevE.72.046304.

Babadagli, T., and S. Al-Salmi, 2004, A review of permeability-prediction methods for carbonate reservoirs using well-log data: SPE Reservoir Evaluation & Engineering, v. 7, no. 2, p. 75–88, doi:10.2118/87824-PA.

Barton, N., and E. Quadros, 2014, Anisotropy is everywhere, to see, to measure, and to model: Rock Mechanics and Rock Engineering, v. 48, no. 4, p. 1323–1339, doi:10.1007/s00603-014-0632-7.

Beebe, R. A., J. B. Beckwith, and J. M. Honig, 1945, The determination of small surface areas by krypton adsorption at low temperatures: Journal of the American Chemical Society, v. 67, no. 9, p. 1554–1558, doi:10.1021/ja01225a048.

Boggs, S. Jr., 2009, Petrology of sedimentary rocks, 2nd ed.: Cambridge, United Kingdom, Cambridge University Press, 600 p., doi:10.1017/CBO9780511626487.

BP, 2018, BP energy outlook, accessed February 10, 2019, https://www.bp.com/content/dam/bp/business-sites/en/global/corporate/pdfs/energy-economics/energy-outlook/bp-energy-outlook-2018.pdf.

Brooks, C. S., and W. R. Purcell, 1952, Surface area measurements on sedimentary rocks: Fall Meeting of the Petroleum Branch of American Institute of Mining and Metallurgical Engineers, Houston, Texas, October 1–3, 1952, SPE-222-G, 12 p., doi:10.2118/222-G.

Buiting, J. J. M., and E. A. Clerke, 2013, Permeability from porosimetry measurements: Derivation for a tortuous and fractal tubular bundle: Journal of Petroleum Science Engineering, v. 108, p. 267–278, doi:10.1016/j.petrol.2013.04.016.

Carman, P. C., 1997, Fluid flow through granular beds: Chemical Engineering Research and Design, v. 75, p. S32–S48, doi:10.1016/S0263-8762(97)80003-2.

Cerato, A. B., and A. J. Lutenegger, 2002, Determination of surface area of fine-grained soils by the ethylene glycol monoethyl ether (EGME) method: Geotechnical Testing Journal, v. 25, no. 3, p. 315–321, doi:10.1520/GTJ11087J.

Charlaix, E., E. Guyon, and S. Roux, 1987, Permeability of a random array of fractures of widely varying apertures: Transport in Porous Media, v. 2, no. 1, p. 31–43, doi:10.1007/BF00208535.

Chilingarian, G. V., J. Chang, and K. I. Bagrintseva, 1990, Empirical expression of permeability in terms of porosity, specific surface area, and residual water saturation of carbonate rocks: Journal of Petroleum Science Engineering, v. 4, no. 4, p. 317–322, doi:10.1016/0920-4105(90)90029-3.

Churcher, P. L., P. R. French, J. C. Shaw, and L. L. Schramm, 1991, Rock properties of Berea Sandstone, Baker Dolomite, and Indiana Limestone: SPE International Symposium on Oilfield Chemistry, Anaheim, California, February 20–22, 1991, SPE-21044-MS, 19 p., doi:10.2118/21044-MS.

Clerke, E. A., 2009, Permeability, relative permeability, microscopic displacement efficiency and pore geometry of M_1 bimodal pore systems in Arab-D limestone: SPE Journal, v. 14, p. 524–531, doi:10.2118/105259-PA.

Clerke, E. A., H. W. Mueller III, E. C. Phillips, R. Y. Eyvazzadeh, D. H. Jones, R. Ramamoorthy, and A. Srivastava, 2008, Application of Thomeer hyperbolas to decode the pore systems, facies and reservoir properties of the Upper Jurassic Arab D Limestone, Ghawar field, Saudi Arabia: A "Rosetta Stone" approach: GeoArabia, v. 13, no. 4, p. 113–160.

Corbett, K., M. Friedman, and J. Spang, 1987, Fracture development and mechanical stratigraphy of Austin Chalk, Texas: AAPG Bulletin, v. 71, no. 1, p. 17–28.

Costa, A., 2006, Permeability-porosity relationship: A reexamination of the Kozeny-Carman equation based on a fractal pore-space geometry assumption: Geophysical Research Letters, v. 33, no. 2, p. L02318, doi:10.1029/2005GL025134.

Croizé, D., F. Renard, and J.-P. Gratier, 2013, Compaction and porosity reduction in carbonates: A review of observations, theory and experiments: Advances in Geophysics, v. 54, p. 181–238, doi:10.1016/B978-0-12-380940-7.00003-2.

Daigle, H., 2016, Application of critical path analysis for permeability prediction in natural porous media: Advances in Water Resources, v. 96, p. 43–54, doi:10.1016/j.advwatres.2016.06.016.

Diamond, S., 2000, Mercury porosimetry: An inappropriate method for the measurement of pore size distributions in cement-based materials: Cement and Concrete Research, v. 30, no. 10, p. 1517–1525, doi:10.1016/S0008-8846(00)00370-7.

Dogruoz, C., N. Bolukbasi, J. Rostami, and C. Acar, 2016, An experimental study of cutting performances of worn picks: Rock Mechanics and Rock Engineering, v. 49, no. 1, p. 213–224, doi:10.1007/s00603-015-0734-x.

Dullien, F. A. L., 1992, Porous media: Fluid transport and pore structure, 2nd ed.: San Diego, California, Academic Press, 574 p.

Dunham, R. J., 1962, Classification of carbonate rocks according to depositional textures, *in* W. E. Ham, ed., Classification of carbonate rocks--A symposium: AAPG Memoir 1, p. 108–121.

Dürrast, H., and S. Siegesmund, 1999, Correlation between rock fabrics and physical properties of carbonate reservoir rocks: International Journal of Earth Sciences, v. 88, no. 3, p. 392–408, doi:10.1007/s005310050274.

Fabricius, I. L., G. Baechle, G. P. Eberli, and R. Weger, 2007, Estimating permeability of carbonate rocks from porosity and vp/vs: Geophysics, v. 72, no. 5, p. E185–E191, doi:10.1190/1.2756081.

Fisher, W. L., and P. U. Rodda, 1969, Edwards Formation (Lower Cretaceous), Texas: Dolomitization in a carbonate platform system: AAPG Bulletin, v. 53, no. 1, p. 55–72.

Friedman, S. P., and N. A. Seaton, 1998, Critical path analysis of the relationship between permeability and electrical conductivity of three-dimensional pore networks: Water Resources Research, v. 34, no. 7, p. 1703–1710, doi:10.1029/98WR00939.

Gale, J. F. W., S. E. Laubach, R. A. Marrett, J. E. Olson, J. Holder, and R. M. Reed, 2004, Predicting and characterizing fractures in dolostone reservoirs: Using the link between diagenesis and fracturing, *in* C. J. R. Braithwaite, G. Rizzi, and G. Darke, eds., The geometry and petrogenesis of dolomite hydrocarbon reservoirs: Geological Society, London, Special Publications 2004, v. 235, p. 177–192, doi:10.1144/GSL.SP.2004.235.01.08.

Gao, Z., and Q. Hu, 2013, Estimating permeability using median pore-throat radius obtained from mercury intrusion porosimetry: Journal of Geophysics and Engineering, v. 10, no. 2, p. 1–7, doi:10.1088/1742-2132/10/2/025014.

Giesche, H., 2006, Mercury porosimetry: A general (practical) overview: Particle & Particle Systems Characterization, v. 23, no. 1, p. 9–19, doi:10.1002/ppsc.200601009.

Glover, J. P. W., I. I. Zadjali, and K. A. Frew, 2006, Permeability prediction from MICP and NMR data using an electrokinetic approach: Geophysics, v. 71, no. 4, p. F49–F60, doi:10.1190/1.2216930.

Hunt, A. G., and G. W. Gee, 2002, Application of critical path analysis to fractal porous media: Comparison with examples from the Hanford site: Advances in Water Resources, v. 25, no. 2, p. 129–146, doi:10.1016/S0309-1708(01)00057-4.

International Energy Agency, 2015, World energy outlook 2015: Executive summary, accessed July 6, 2017, https://webstore.iea.org/download/summary/224?fileName=English-WEO-2015-ES.pdf.

International Energy Agency, 2018, World energy outlook 2018: Executive summary, accessed February 10, 2019, https://webstore.iea.org/download/summary/190?fileName=English-WEO-2018-ES.pdf.

Jang, J., G. A. Narsilio, and J. C. Santamarina, 2011, Hydraulic conductivity in spatially varying media—A pore-scale investigation: Geophysical Journal International, v. 184, no. 3, p. 1167–1179, doi:10.1111/j.1365-246X.2010.04893.x.

Jennings, J. W. Jr., and F. J. Lucia, 2003, Predicting permeability from well logs in carbonates with a link to geology for interwell permeability mapping: SPE Reservoir Evaluation & Engineering, v. 6, no. 4, p. 215–225, doi:10.2118/84942-PA.

Katz, A. J., and A. H. Thompson, 1985, Fractal sandstone pores: Implications for conductivity and pore formation: Physical Review Letters, v. 54, no. 12, p. 1325–1328, doi:10.1103/PhysRevLett.54.1325.

Katz, A. J., and A. H. Thompson, 1986, Quantitative prediction of permeability in porous rock: Physical Review B, v. 34, no. 11, p. 8179–8181, doi:10.1103/PhysRevB.34.8179.

Kozeny, J., 1927, About capillary conduction of water in the soil (ascent, infiltration and application to irrigation) [in

German]: Vienna, Austria, Academy of Sciences Meeting Report 136, p. 271–306.

Kyser, T. K., N. P. James, and Y. Bone, 1998, Alteration of Cenozoic cool-water carbonates to low-Mg calcite in marine waters, Gambier Embayment, South Australia: Journal of Sedimentary Research, v. 68, no. 5, p. 947–955, doi:10.2110/jsr.68.947.

Lenormand, R., 2003, Interpretation of mercury injection curves to derive pore size distribution: International Symposium of the Society of Core Analysts, Pau, France, September 21–24, 2003, 7 p.

León y León, C. A., 1998, New perspectives in mercury porosimetry: Advances in Colloid and Interface Science, v. 76–77, p. 341–372, doi:10.1016/S0001-8686(98)00052-9.

Lindsay, R. F., D. L. Cantrell, G. W. Hughes, T. H. Keith, H. W. Mueller III, and S. D. Russel, 2006, Ghawar Arab-D Reservoir: Widespread porosity in shoaling-upward carbonate cycles, Saudi Arabia, *in* P. M. Harris and L. J. Weber, eds., Giant hydrocarbon reservoirs of the world: From rocks to reservoir characterization and modeling: AAPG Memoir 88, p. 97–137.

Lucia, F. J., 1995, Rock-fabric/petrophysical classification of carbonate pore space for reservoir characterization: AAPG Bulletin, v. 79, no. 9, p. 1275–1300, doi:10.1306/7834D4A4-1721-11D7-8645000102C1865D.

Lucia, F. J., 2007, Carbonate reservoir characterization: An integrated approach, 2nd ed.: Berlin, Springer-Verlag, 336 p.

Moore, C. H., and W. J. Wade, 2013, The nature and classification of carbonate porosity, *in* C. H. Moore and W. J. Wade, eds., Carbonate reservoirs: Porosity and diagenesis in a sequence stratigraphic framework, 2nd ed.: Amsterdam, Elsevier, Developments in Sedimentology 67, p. 51–65, doi:10.1016/B978-0-444-53831-4.00004-5.

Moro, F., and H. Böhni, 2002, Ink-bottle effect in mercury intrusion porosimetry of cement-based materials: Journal of Colloid and Interface Science, v. 246, no. 1, p. 135–149, doi:10.1006/jcis.2001.7962.

Mortensen, J., F. Engstrom, and I. Lind, 1998, The relation among porosity, permeability, and specific surface of chalk from the Gorm Field, Danish North Sea: SPE Reservoir Evaluation & Engineering, v. 1, p. 245–251, doi:10.2118/31062-PA.

Nelson, P. H., 1994, Permeability-porosity relationships in sedimentary rocks: The Log Analyst, v. 35, no. 3, p. 38–62.

Nelson, P. H., 2009, Pore-throat sizes in sandstones, tight sandstones, and shales: AAPG Bulletin, v. 93, no. 3, p. 329–340, doi:10.1306/10240808059.

Nishiyama, N., and T. Yokoyama, 2017, Permeability of porous media: Role of the critical pore size: Journal of Geophysical Research Solid Earth, v. 122, no. 9, p. 6955–6971, doi:10.1002/2016JB013793.

Ortega, O. J., J. F. W. Gale, and R. Marrett, 2010, Quantifying diagenetic and stratigraphic controls on fracture intensity in platform carbonates: An example from the Sierra Madre Oriental, northeast Mexico: Journal of Structural Geology, v. 32, no. 12, p. 1943–1959, doi:10.1016/j.jsg.2010.07.004.

Pape, H., C. Clauser, and J. Iffland, 1999, Permeability prediction based on fractal pore-space geometry: Geophysics, v. 64, no. 5, p. 1447–1460, doi:10.1190/1.1444649.

Pemberton, S. G., and M. K. Gingras, 2005, Classification and characterizations of biogenically enhanced permeability: AAPG Bulletin, v. 89, no. 11, p. 1493–1517, doi:10.1306/07050504121.

Poursoltani, M. R., and M. R. Gibling, 2011, Composition, porosity, and reservoir potential of the Middle Jurassic Kashafrud Formation, northeast Iran: Marine and Petroleum Geology, v. 28, no. 5, p. 1094–1110, doi:10.1016/j.marpetgeo.2010.11.004.

Railsback, L. B., 1993, Contrasting styles of chemical compaction in the Upper Pennsylvanian Dennis Limestone in the Midcontinent region, U.S.A.: Journal of Sedimentary Petrology, v. 63, no. 1, p. 61–72, doi:10.1306/D4267A8C-2B26-11D7-8648000102C1865D.

Rashid, F., P. W. J. Glover, P. Lorinczi, R. Collier, and J. Lawrence, 2015, Porosity and permeability of tight carbonate reservoir rocks in the north of Iraq: Journal of Petroleum Science Engineering, v. 133, p. 147–161, doi:10.1016/j.petrol.2015.05.009.

Ren, X. W., and J. C. Santamarina, 2018, The hydraulic conductivity of sediments: A pore size perspective: Engineering Geology, v. 233, p. 48–54, doi:10.1016/j.enggeo.2017.11.022.

Rezaee, M. R., A. Jafari, and E. Kazemzadeh, 2006, Relationships between permeability, porosity and pore throat size in carbonate rocks using regression analysis and neural networks: Journal of Geophysics and Engineering, v. 3, no. 4, p. 370–376, doi:10.1088/1742-2132/3/4/008.

Sander, R., Z. Pan, and L. D. Connell, 2017, Laboratory measurement of low permeability unconventional gas reservoir rocks: A review of experimental methods: Journal of Natural Gas Science and Engineering, v. 37, p. 248–279, doi:10.1016/j.jngse.2016.11.041.

Saner, S., and A. Sahin, 1999, Lithological and zonal porosity-permeability distributions in the Arab-D Reservoir, Uthmaniyah Field, Saudi Arabia: AAPG Bulletin, v. 83, no. 2, p. 230–243.

Santarelli, F. J., A. F. Marsala, M. Brignoli, E. Rossi, and N. Bona, 1998, Formation evaluation from logging on cuttings: SPE Reservoir Evaluation & Engineering, v. 1, p. 238–244.

Sibson, R. H., 1994, Crustal stress, faulting and fluid flow: Geological Society, London, Special Publications 1994, v. 78, p. 69–84, doi:10.1144/GSL.SP.1994.078.01.07.

Swanson, B. F., 1981, A simple correlation between permeabilities and mercury capillary pressures: Journal of Petroleum Technology, v. 33, p. 2498–2504, doi:10.2118/8234-PA.

Tanikawa, W., and T. Shimamoto, 2009, Comparison of Klinkenberg-corrected gas permeability and water permeability in sedimentary rocks: International Journal of Rock Mechanics and Mining Sciences, v. 46, no. 2, p. 229–238, doi:10.1016/j.ijrmms.2008.03.004.

Thomeer, J. H., 1983, Air permeability as a function of three pore-network parameters: Journal of Petroleum Technology, v. 35, no. 4, p. 809–814, doi:10.2118/10922-PA.

Tiab, D., and E. C. Donaldson, 2012, Petrophysics: Theory and practice of measuring reservoir rock and fluid transport properties, 3rd ed.: Boston, Gulf Professional Publishing, 976 p.

Tipping, R. G., A. C. Runkel, E. C. Alexander Jr., S. C. Alexander, and J. A. Green, 2006, Evidence for hydraulic heterogeneity and anisotropy in the mostly carbonate Prairie du Chien Group, southeastern Minnesota, USA: Sedimentary Geology, v. 184, no. 3–4, p. 305–330, doi:10.1016/j.sedgeo.2005.11.007.

Toussaint, R., E. Aharonov, D. Koehn, J.-P. Gratier, M. Ebner, P. Baud, A. Rolland, and F. Renard, 2018, Stylolites: A review: Journal of Structural Geology, v. 114, p. 163–195, doi:10.1016/j.jsg.2018.05.003.

Uddin, Y. N., E. A. Clerke, B. Bammel, S. Koronfol, and A. Grader, 2017, Quantitative study of formation vertical permeability in Middle East Thalassinoides burrowed carbonate mudstone: SPE Reservoir Characterisation and Simulation Conference and Exhibition, Abu Dhabi, United Arab Emirates, May 8–10, 2017, SPE-186001-MS, 17 p.

US Energy Information Administration, 2015, International energy statistics: Total primary energy production, accessed July 6, 2017, https://www.eia.gov/beta/international/data/browser.

Van Golf-Racht, T. D., 1996, Naturally-fractured carbonate reservoirs, *in* G. V. Chilingarian, S. J. Mazzullo, and H. H. Rieke, eds., Carbonate reservoir characterization: A geologic-engineering analysis: Amsterdam, Elsevier, v. 44, pt. 2, p. 683–771, doi:10.1016/S0376-7361(96)80029-X.

Vincent, B., M. Fleury, Y. Santerre, and B. Brigaud, 2011, NMR relaxation of neritic carbonates: An integrated petrophysical and petrographical approach: Journal of Applied Geophysics, v. 74, no. 1, p. 38–58, doi:10.1016/j.jappgeo.2011.03.002.

Weger, R. J., G. P. Eberli, G. T. Baechle, J. L. Massaferro, and Y.-F. Sun, 2009, Quantification of pore structure and its effect on sonic velocity and permeability in carbonates: AAPG Bulletin, v. 93, no. 10, p. 1297–1317, doi:10.1306/05270909001.

Weiner, W. F., and A. F. Koster Van Groos, 1976, Petrographic and geochemical study of the formation of chert around the Thornton reef complex, Illinois: Geological Society of America Bulletin, v. 87, no. 2, p. 310–318, doi:10.1130/0016-7606(1976)87<310:PAGSOT>2.0.CO;2.

Wu, Y.-S., K. Pruess, and P. Persoff, 1998, Gas flow in porous media with Klinkenberg effects: Transport in Porous Media, v. 32, no. 1, p. 117–137, doi:10.1023/A:1006535211684.